

Copyright

by

Ning Kong

2009

**The Dissertation Committee for Ning Kong Certifies that this is the approved  
version of the following dissertation:**

**Dopant Behavior in Complex Semiconductor Systems**

**Committee:**

---

Sanjay K. Banerjee, Supervisor

---

Taras A. Kirichenko, Co-Supervisor

---

Jack C. Lee

---

Leonard F. Register

---

Alexander A. Demkov

---

Emanuel Tutuc

# **Dopant Behavior in Complex Semiconductor Systems**

**by**

**Ning Kong, B.S.; M.S.E.**

## **Dissertation**

Presented to the Faculty of the Graduate School of

The University of Texas at Austin

in Partial Fulfillment

of the Requirements

for the Degree of

**Doctor of Philosophy**

**The University of Texas at Austin**

**December, 2009**

## **Dedication**

To my wife, Fei, and my parents.



## **Acknowledgements**

My past five years in Austin has been a challenging and exciting journey. I would like to begin my acknowledgements by thanking my supervisor, Dr. Sanjay K. Banerjee for his supervision, patience, encouragement and financial support. His vision and enthusiasm for technology development provided an ideal environment for my graduate research. The great academic freedom in his group made possible my research achievements in a variety of interesting topics, and also trained me to be an independent investigator.

Second, I would like to thank my co-supervisor, Dr. Taras A. Kirichenko for his intensive guidance and collaboration throughout the course of this work. He is extremely responsible and resourceful. His important advice on my research and career development definitely changes my life. It is not exaggerating to say that without his encouragement and support, this work is not possible.

My thanks also go to Dr. Mark C. Foisy for his critical review and facilitation of my projects during my summer interns. And I am grateful to Dr. Gyeong S. Hwang for his enlightening comments and suggestions. My gratitude also goes to my doctoral committee.

In addition, I would like to thank Li Lin and Yonghyun Kim for the very helpful discussions. Also I thank Zhihong Huang, Junjing Bao, Xiaofeng Fan, Ningyu Shi, Ken Liu, Xin Zheng, Yueran Liu, Di Li, and Han Zhao for their friendship and help.

This dissertation is dedicated to my wife and my parents for their love, encouragement and support.

# **Dopant Behavior in Complex Semiconductor Systems**

Publication No. \_\_\_\_\_

Ning Kong, Ph.D.

The University of Texas at Austin, 2009

Supervisor: Sanjay K. Banerjee

Co-Supervisor: Taras A. Kirichenko

As the size of modern transistors is continuously scaled down, challenges rise in almost every component of a silicon device. Formation of ultra shallow junction (USJ) with high activation level is particularly important for suppressing short channel effects. However, the formation of low resistance USJ is made difficult by dopant Transient Enhanced Diffusion (TED) and clustering-induced deactivation. In this work, we proposed a novel point defect engineering solution to address the arsenic TED challenge. By overlapping arsenic doped region with silicon interstitials and vacancies, we observed enhanced and retarded arsenic diffusion upon anneal, respectively. We explain this phenomenon by arsenic interstitial diffusion mechanism. In addition, we implemented this interstitial-based mechanism into a kinetic Monte Carlo (kMC) simulator. The key role of interstitials in arsenic TED is confirmed. And we demonstrated that the simulator has an improved prediction capability for arsenic TED and deactivation.

As a long time unsolved process challenge, arsenic segregation at SiO<sub>2</sub>/Si interface was investigated using density functional theory (DFT) calculation. The

segregation-induced arsenic dose loss not only increases resistance but also may induce interface states. We identified three arsenic complex configurations,  $\text{As}_{it}$ ,  $\text{As}_2\text{I}_{2I}$  and  $\text{As}_2\text{I}_{2II}$ , which are highly stabilized at  $\text{SiO}_2/\text{Si}$  interface due to the unique local bonding environments. Therefore, they could contribute to arsenic segregation as both initial stage precursors and dopant trapping sites. Our calculation indicates that arsenic atoms trapped in such interface complexes are electrically inactive. Finally, the formation and evolution dynamics of these interface arsenic-defect complexes are discussed and kMC models are constructed to describe the segregation effects.

A potential problem for the p-type USJ formation is the recently found transient fast boron diffusion during solid phase epitaxial regrowth process. Using DFT calculations and molecular dynamics simulation, we identified an interstitial-based mechanism of fast boron diffusion in amorphous silicon. The activation energy for this diffusion mechanism is in good agreement with experimental results. In addition, this mechanism is consistent with the experimentally reported transient and concentration-dependent features of boron diffusion in amorphous silicon.

## Table of Contents

<b>List of Tables.....</b>	<b>x</b>
<b>List of Figures .....</b>	<b>xi</b>
<b>Chapter 1 Research Background.....</b>	<b>1</b>
1.1 Ultra shallow junction in modern silicon transistors.....	1
1.2 Dopant transient enhanced diffusion and deactivation .....	2
1.3 Kinetic Monte Carlo simulation.....	5
1.4 Density functional theory calculation .....	7
1.5 Organization .....	10
<b>Chapter 2 Arsenic Transient Enhanced Diffusion in Point Defect Engineered Silicon .....</b>	<b>11</b>
2.1 Point defect engineering implant.....	11
2.2 Arsenic diffusion mechanism.....	13
2.3 Experimental details.....	14
2.4 Results and discussion.....	17
2.5 Conclusions .....	22
<b>Chapter 3 Kinetic Monte Carlo Simulation of Arsenic-Interstitial Interaction and Arsenic Uphill Diffusion.....</b>	<b>24</b>
3.1 Introduction .....	24
3.2 Kinetic Monte Carlo simulation.....	27
3.3 DADOS model calibration .....	30
3.4 Model description.....	34
3.5 Simulation results and discussion .....	41
3.6 Conclusion.....	49
<b>Chapter 4 Arsenic-Defect Complexes at SiO<sub>2</sub>/Si Interfaces .....</b>	<b>51</b>
4.1 Arsenic segregation at SiO <sub>2</sub> /Si interface .....	51
4.2 Computational details.....	53
4.3 Bulk-stabilized arsenic complexes at SiO <sub>2</sub> /Si interface .....	56

4.4 Interface-stabilized arsenic complexes at SiO <sub>2</sub> /Si interface.....	58
4.5 Kinetic arsenic complex models .....	66
4.6 Conclusion.....	70
<b>Chapter 5 Boron Diffusion Dynamics in Amorphous Silicon .....</b>	<b>72</b>
5.1 Introduction .....	72
5.2 Computational details.....	75
5.3 Results and discussion.....	77
5.4 Conclusion.....	82
<b>Chapter 6 Conclusions and Recommendation for Future Work.....</b>	<b>83</b>
6.1 Conclusions .....	83
6.2 Recommendation for future work .....	85
<b>References .....</b>	<b>87</b>
<b>Vita.....</b>	<b>96</b>

## List of Tables

Table 3.1:	Atomistic parameters of the species related with arsenic TED. Charge states are denoted by superscripts. Arsenic interstitial pair migration energies ( $E_m$ ), binding energies ( $E_b$ ) and ionization levels ( $e_t-e_v$ ) are based on [Har05a]. Other parameters are based on [Pin05]......	40
Table 3.2:	Arsenic cluster binding energies. Parameters based on [Ram96] and [Har06]. .....	41
Table 4.1:	Fermi level of arsenic complexes in bulk Si and SiO <sub>2</sub> /Si interface structures. The 0.35eV and 0.36eV in parentheses indicate deep donor level positions due to As <sub>it</sub> . .....	63

## List of Figures

Figure 1.1:	Typical transistor structure.....	2
Figure 1.2:	Mechanism of point defect-induced arsenic TED and deactivation. .	3
Figure 1.3:	Arsenic clustering and enhanced diffusion for 750°C and 800°C anneals. Figure is from [Sol03]. .....	4
Figure 1.4:	Arsenic enhanced diffusion by both interstitial injection from surface oxidation and vacancy injection from surface nitridation. Figure is from [Ura99]. .....	5
Figure 1.5:	DADOS simulation of dopant and point defect particles. Yellow particles are arsenic species. Red rods are {311} defects and red plates are dislocation loop defects. Figure is from [MarD].....	6
Figure 1.6:	Comparison of all-electron potential (solid line) and pseudopotential (dashed line) and their corresponding wavefunctions. The figure is from [Pay92].....	8
Figure 1.7:	Finding total energy using an iterative minimization scheme. The figure is from [Kre07]. .....	9
Figure 2.1:	Principle of point defect engineering implant: (a) Illustration of interstitial-vacancy separation during ion implantation (b) Dopant, interstitial and vacancy layer distribution of point defect engineered wafers.....	12
Figure 2.2:	Experimental procedure. ....	15

Figure 2.3: UT-MARLOWE simulations of As and Si I-rich/V-rich as-implanted profiles. 5 keV As was implanted with dose  $1 \times 10^{15} \text{ cm}^{-2}$  (triangles) or  $6 \times 10^{13} \text{ cm}^{-2}$  (stars). The net IV separation is shown with open circles denoting net vacancy, and solid circles denoting net interstitial distributions. V-rich implant is shown in the inset. .. 16

Figure 2.4: SIMS profiles of low dose ( $6 \times 10^{13} \text{ cm}^{-2}$ ) arsenic diffusion. (a) (b) are samples without pre-anneal; (c) (d) are with  $1025^\circ\text{C}$ , 10s pre-anneal. Then V-rich (grey line, Si V-rich) or I-rich (triangles, Si I-rich) or no (black line, no Si implant) Si implant into bulk Si, or V-rich Si implant into SOI (cross, SOI V-rich), is performed, followed by a post-anneal of  $750^\circ\text{C}$ , 10min as shown in (a) (c), or  $1025^\circ\text{C}$ , 5s as shown in (b) (d). The SIMS profiles immediately after pre-anneal are shown as starting curves for post-anneal (square)..... 18

Figure 2.5: SIMS profiles of high dose ( $1 \times 10^{15} \text{ cm}^{-2}$ ) arsenic diffusion. Similar processes as for Figure 2.4 (c) and (d) are used, except for a higher arsenic implant dose. Post-anneals are performed for (a)  $700^\circ\text{C}$ , 10min (b)  $750^\circ\text{C}$ , 10min (c)  $1025^\circ\text{C}$ , 5s..... 21

Figure 2.6: Point defect engineering implant energy and dose optimization. .... 22

Figure 3.1: Kinetic Monte Carlo simulation used in device level simulation. Red rods indicate the formation of extended defects and light blue species indicate clustered dopant atoms. The picture is from [Syn09]. ..... 27

Figure 3.2: DADOS modules organization..... 28



Figure 3.3: DADOS simulation procedure and event list (a) DADOS simulation procedure (b) Event list. ....	29
Figure 3.4: Comparison of DADOS with experiments: DC products for interstitial and vacancy [Bra95] [Cow99a] [Gie00]. ....	31
Figure 3.5: Comparison of DADOS with experiments: point defect evolution (a) Time evolution of interstitial supersaturation [Cow99b], (b) Time evolution of interstitials trapped in clusters/{311} [Sto97]. ....	32
Figure 3.6: Comparison of DADOS with experiments: boron diffusion [Cow91]. ....	33
Figure 3.7: Comparison of DADOS with experiments: boron TED and clustering [Pel97]. ....	34
Figure 3.8: Arsenic intrinsic diffusivity: Lines are experimental values from different references [Plu00] [Cer86] [Fai81] [Ish82]. Void squares show the theoretical values calculated by DADOS parameters. ....	35
Figure 3.9: New models implemented in DADOS. ....	37
Figure 3.10: Arsenic diffusion SIMS profiles [Kon07] and DADOS simulation. Blue curves are SIMS profiles. Red cross curves are DADOS simulation with arsenic-interstitial mechanism implemented. Green square curves are DADOS simulation with the previous models. All diffusion and Si implant steps are after a 5 keV, $6 \times 10^{13} \text{ cm}^{-2}$ arsenic implant. The profiles start from the Si/SiO <sub>2</sub> interface. ....	39
Figure 3.11: Enhanced and retarded arsenic TED by DADOS simulation. Profiles are obtained after 5 keV, $6 \times 10^{13} \text{ cm}^{-2}$ arsenic implant, I-rich/V-rich/no Si implant and 750°C 10 min anneal. ....	41

Figure 3.12: Time evolution of free point defect concentrations during annealing after I-rich/V-rich/no Si implants. Implant and annealing conditions are the same as for Figure 3.11. ....	43
Figure 3.13: Time evolution of $As_i$ pair and $AsV$ pair concentrations during annealing after I-rich/V-rich/no Si implants. Implant and annealing conditions are the same as for Figure 3.11. ....	44
Figure 3.14: Time evolution of arsenic dose trapped in $As_nI_m$ clusters and $As_nV_m$ clusters during annealing after I-rich/V-rich/no Si implants. Implant and annealing conditions are the same as for Figure 3.11. ....	45
Figure 3.15: Time evolution of average arsenic number in $As_nV_m$ clusters, for I-rich, V-rich and no Si implant cases. Implant and annealing conditions are the same as for Figure 3.11. ....	46
Figure 3.16: DADOS simulated sheet resistance. Samples are implanted by 5 keV, $6 \times 10^{13} \text{ cm}^{-2}$ arsenic, followed by I-rich/V-rich/no Si implants and then followed by (a) 750°C, 10min and (b) 1025°C, 5s anneal. ....	48
Figure 4.1: $SiO_2/Si$ interface structures used in this work: (a) monolayer crystalline- $SiO_2/Si$ interface structure (c- $SiO_2/Si$ ) and the definition of position and orientation of arsenic complexes in this system (b) amorphous $SiO_2/Si$ interface structure (a- $SiO_2/Si$ ).....	54

Figure 4.2:	Total energy of $As_4V$ and split(110) $As_i$ in different layers of $SiO_2/Si$ interface structure. The total energy of arsenic complex in deep layers (deep layers are considered to have bulk Si-like properties) are set to be 0 eV reference. The position and orientation associated with interface arsenic complexes are marked, corresponding to the definition in Figure 4.1.....	56
Figure 4.3:	$As_{it}$ configuration at (a) monolayer c- $SiO_2/Si$ interface and (b) a- $SiO_2/Si$ interface.....	59
Figure 4.4:	(a) $As_{it}$ structure (b) Split(111) interstitial structure with a neighboring $As_{sub}$ . ....	60
Figure 4.5:	$As_2I_{2I}$ configuration at (a) monolayer c- $SiO_2/Si$ interface (b) a- $SiO_2/Si$ interface; $As_2I_{2II}$ configuration at (c) monolayer c- $SiO_2/Si$ interface (d) a- $SiO_2/Si$ interface. Atom #1 and #2 are the two arsenic atoms. ....	61
Figure 4.6:	ELF iso-surface plot of (a) $As_{it}$ in c- $SiO_2/Si$ interface, (b) $As_2I_{2I}$ in c- $SiO_2/Si$ interface and (c) $As_2I_{2II}$ in a- $SiO_2/Si$ interface, with ELF=0.88. The blue balls represent O and green balls represent Si in (a) and (b). In (c), the blue balls represent Si and green balls are O. Red ball represents As in all (a), (b) and (c). ....	62
Figure 4.7:	Evolution from $As_i$ in bulk Si to interface $As_{it}$ : (a) from split(110) $As_i$ to $As_{it}$ . (b), (c) from hexagonal $As_i$ to $As_{it}$ . (d) Transition from $As_2I_{2I}$ to $As_2I_{2II}$ .....	67
Figure 4.8:	Kinetic models for arsenic segregation based on DFT studies: (a) DADOS models (b) Sentaurus Process models [Sen09].....	68

Figure 4.9: Comparison of kinetic Monte Carlo simulation and experimental data from [Ste08].	69
Figure 5.1: Boron fast diffusion at low annealing temperature. This figure is from [Duf04].	73
Figure 5.2: Transient feature of boron fast diffusion: diffusivity decreases with time. This figure is from [Mir08].	74
Figure 5.3: Amorphous silicon supercells: (a) 64-atom (b) 211-atom.	76
Figure 5.4: MD simulation shows $B_i$ will kick out lattice Si and become $B_{sub}+I$ .	78
Figure 5.5: The diffusion of $B_i$ through a-Si lattice.	78
Figure 5.6: The mobility of kicked-out interstitials. $B_i$ kicks out Si #2 and Si #2 kicks out Si #3. Due to periodic boundary conditions, Si #2 moves upward and injects from down side of Si #3.	79
Figure 5.7: Interstitial-based B diffusion mechanism in a-Si.	80

## **Chapter 1: Research Background**

### **1.1 ULTRA SHALLOW JUNCTION IN MODERN SILICON TRANSISTORS**

The remarkable growth of the microelectronics industry has brought us into the very large scale integration (VLSI) age. The main driving force of this development is the scaling of Si transistors, predicted by Gordon Moore in 1965 as the number of transistors that can be integrated on a microchip will double for every 18 months [Moo65]. This prediction surprisingly held for more than 40 years and is still being pushed forward for faster and more powerful chips.

Figure 1.1 is an illustration of a typical transistor structure. A huge amount of effort has been made to shrink the gate length by employing advanced lithography technology. However, as the feature length shrinks to sub-100nm or less, some other problems emerge and seriously degrade the device performance. One major problem is that as the source and drain region become closer to each other, the electrical field from drain will attract the carriers from source region to overcome the barrier imposed by source-channel junction. This effect will circumvent the gate control over the channel current and cause leakage even when the gate is off. The source and drain extension regions shown in Figure 1.1 is used to address this problem. The electrical field interaction between source and drain will be substantially reduced by the ultra shallow junctions (USJ) in the extension region. However, one of the major tradeoffs of using shallow extensions is that source/drain resistance will increase with decreased junction depth. Therefore a high activation level is usually required in these extension regions to lower the source/drain resistance.

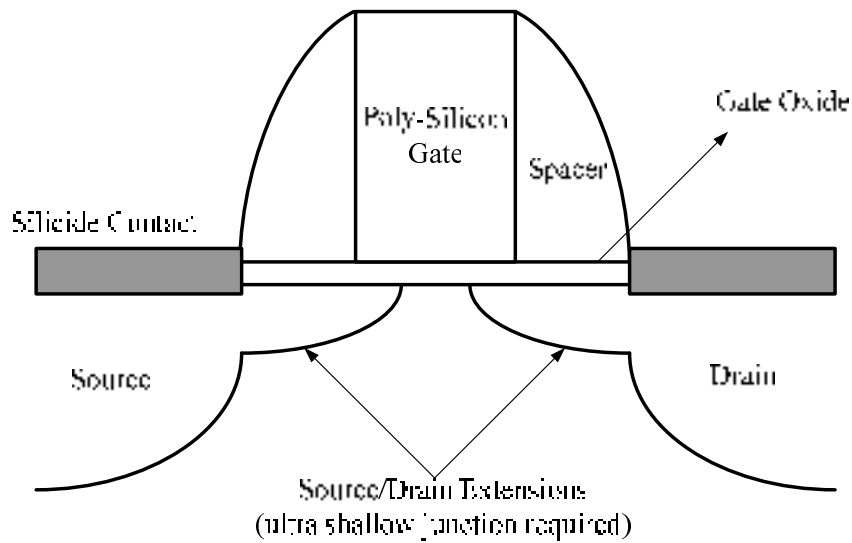


Figure 1.1: Typical transistor structure.

## 1.2 DOPANT TRANSIENT ENHANCED DIFFUSION AND DEACTIVATION

For the source/drain extension fabrication, low energy dopant implant is commonly used, followed by high temperature annealing for dopant activation and implant damage repair. The process has the targets of shallow junction depth, high dopant activation and good control over dopant diffusion. However, these are always made difficult by dopant Transient Enhanced Diffusion (TED) and deactivation by dopant clustering [Mic87] [Sol03]. These effects are explained by the interaction between dopant and point defects such as interstitials and vacancies. An example of arsenic TED and deactivation mechanism is illustrated in Figure 1.2. Diffusing arsenic interstitial pair ( $As_i$ ) can be created by arsenic-interstitial interaction, while deactivating arsenic vacancy cluster ( $As_nV_m$ ) can be created by arsenic-vacancy reaction.

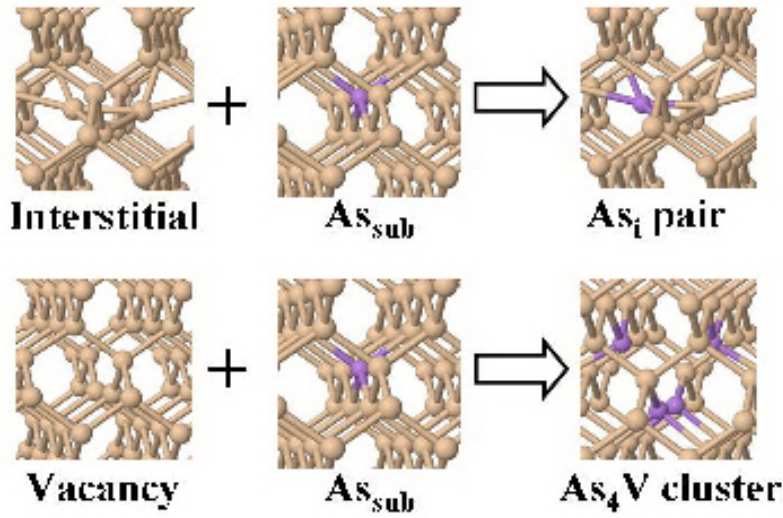
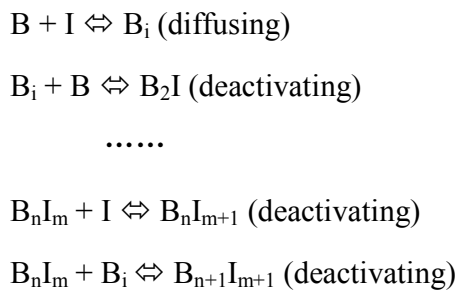


Figure 1.2: Mechanism of point defect-induced arsenic TED and deactivation.

In real semiconductor processing, ion implantation will create interstitials and vacancies in silicon lattice. During the subsequent anneal, some of these point defects will form stable extended defects such as  $\{311\}$  defects, dislocation loops or voids as sources of interstitial and vacancy supersaturation. The mobile interstitials and vacancies will increase the dopant diffusion. For example, boron diffusion and deactivation are well established as related to interstitial dominant mechanism [Fah89], shown as follows:



For arsenic, the TED and clustering are observed experimentally as shown in Figure 1.3 [Sol03]. A variety of research [Sol03] [Fah89] [Ura99] [Har05a] [Xie99] confirmed the combination of interstitial and vacancy mechanism for arsenic TED, shown as:

Interstitial mechanism:  $\text{As} + \text{I} \rightleftharpoons \text{As}_\text{i}$  (diffusing)

Vacancy mechanism:  $\text{As} + \text{V} \rightleftharpoons \text{AsV}$  (diffusing)

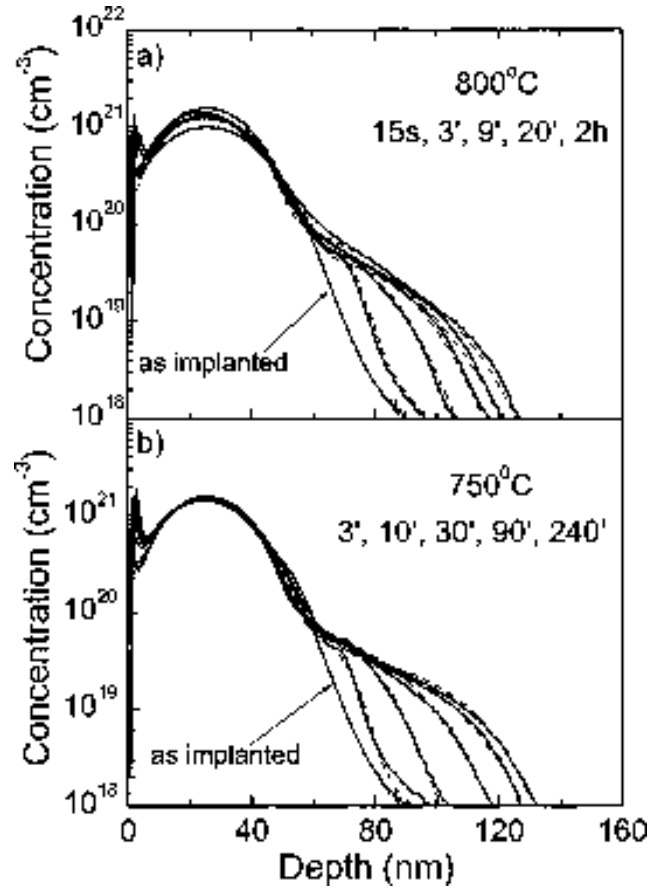


Figure 1.3: Arsenic clustering and enhanced diffusion for 750°C and 800°C anneals.  
Figure is from [Sol03].

As shown in Figure 1.4 [Ura99], both interstitial and vacancy surface injection will enhance arsenic diffusion. For arsenic deactivation, the general opinion is that the arsenic pairs combine with each other and form energetically favorable arsenic vacancy clusters. These clusters will grow larger and more stable by absorbing more mobile arsenic pairs [Xie99]. On the other hand, recent research also proposed interstitial may



also play an important role in arsenic deactivation by the formation of arsenic interstitial clusters ( $As_nI_m$ ) [Har06].

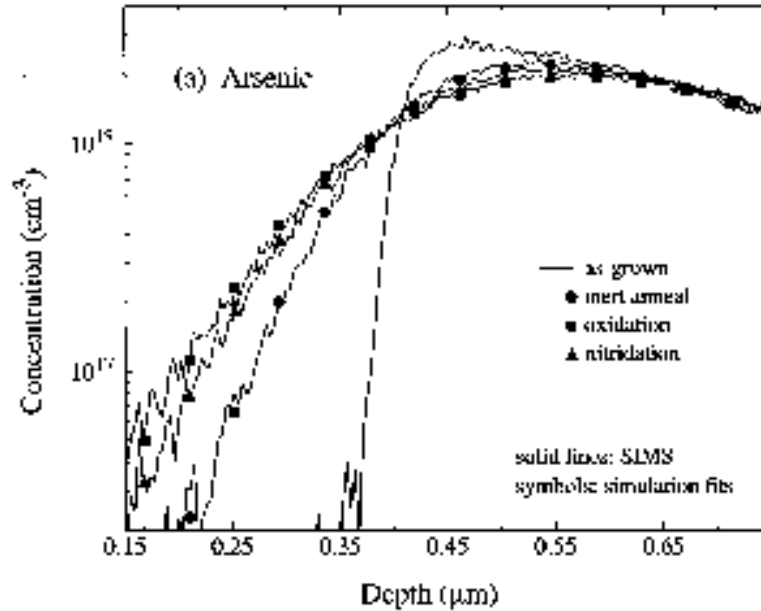


Figure 1.4: Arsenic enhanced diffusion by both interstitial injection from surface oxidation and vacancy injection from surface nitridation. Figure is from [Ura99].

Arsenic TED was conventionally considered to be of less intensity than boron TED and therefore received less attention. However, with the down-scaling of the source/drain extension depth for 45nm node and beyond, the understanding and solution for arsenic TED become more and more a research focus.

### 1.3 KINETIC MONTE CARLO SIMULATION

For process simulation, we use an atomistic kinetic Monte Carlo (kMC) simulator named DADOS [DAD]. It is capable of simulating dopant diffusion, activation and dopant-defect interaction in silicon during annealing process. The kinetic Monte Carlo

simulation differs from lattice Monte Carlo simulation in that only dopant and point defects activities are considered while the silicon lattice atoms are ignored in order to improve computation efficiency. Compared with the mainstream continuum simulator, kMC mainly simulates the behavior of dopant/defect particles, instead of their concentrations. The simulation scenario can be illustrated in Figure 1.5 [MarD]. The simulation includes comprehensive and detailed demonstration of physics concepts and interaction mechanism and the simulation results will contribute to the understanding of inside process. Most of the simulation parameters have physical meanings and can be derived from first-principle calculation. Therefore, the kMC simulation has the potential to provide reliable reference for continuum simulator, upon systematic modeling and calibration. However, the disadvantage is that it is restricted by insufficient understanding of internal mechanism and incomplete parameters. High computation time is another drawback. However, as dimension of modern device shrinks, the simulation time will scale down accordingly, which makes this simulator a potential candidate for future mainstream process simulator.

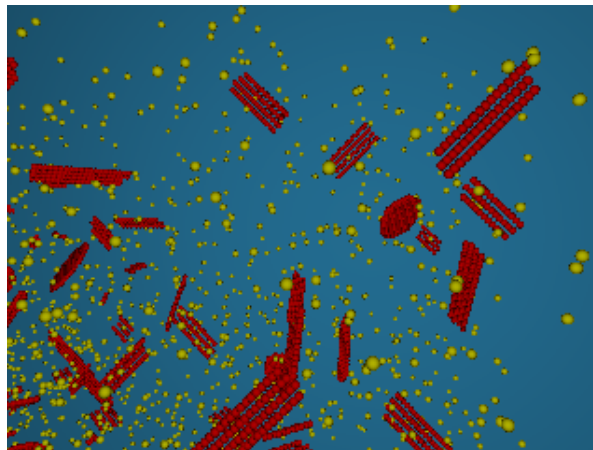


Figure 1.5: DADOS simulation of dopant and point defect particles. Yellow particles are arsenic species. Red rods are  $\{311\}$  defects and red plates are dislocation loop defects. Figure is from [MarD].

## 1.4 DENSITY FUNCTIONAL THEORY CALCULATION

Prediction of the electronic and geometric structure of a solid system requires calculation of the quantum-mechanical total energy of the system and subsequent minimization of that energy by adjusting the electronic and nuclear coordinates. The electron-ion system is intrinsically difficult to handle due to the complicated interactions. However, approximations can be made to simplify the calculation. First, since electrons and ions undergo the same amplitude of forces while having vastly different mass, the movement of ions can be treated adiabatically. Therefore electrons can be treated as in a potential field induced by electron-ion Coulomb interaction. This is called Born-Oppenheimer approximation. The exchange effects will spatially separate electrons with same spin, leading to a reduction of Coulomb interaction between electrons. The corresponding total energy reduction term is called exchange energy. The Hartree-Fock approximation is assumed by including exchange energy term into total energy calculation. The difference between total energy of a realistic electron-ion system and total energy under Hartree-Fock approximation is defined as correlation energy [Fet71]. The wavefunction can be described by Kohn-Sham equations [Koh65]:

$$\left[ \frac{-\hbar^2}{2m} \nabla^2 + V_{ion}(\vec{r}) + V_H(\vec{r}) + V_{XC}(\vec{r}) \right] \psi_i(\vec{r}) = \varepsilon_i \psi_i(\vec{r})$$

The first term in brackets represents kinetic energy,  $V_{ion}$  is the electron-ion potential,  $V_H$  is the Hartree potential of electrons,  $V_{XC}$  is the exchange-correlation potential,  $\psi_i$  represents electron wavefunction of state  $i$ , and  $\varepsilon_i$  is the Kohn-Sham eigenvalue.

Generally it is very difficult to calculate exchange and correlation term  $V_{xc}(\mathbf{r})$  unless certain approximation is used. One approach is based on the fact that total energy as well as exchange and correlation energies are unique function of the electron density [Hoh64]. The well-know Local Density Approximation (LDA) assumes the exchange and correlation energy at a certain location in electron gas is equal to the exchange and correlation energy at a homogenous electron gas with the same local electron density [Koh65]. An improved method called Generalized Gradient Approximation (GGA) assumes the energy terms not only depend on electron density, but also depend on gradient of the density [Per96]. In this way, the exchange and correlation energy can be estimated. The calculation using this approximation is known as density functional theory (DFT) calculation.

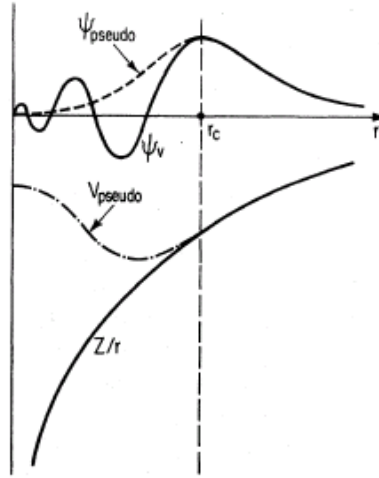


Figure 1.6: Comparison of all-electron potential (solid line) and pseudopotential (dashed line) and their corresponding wavefunctions. The figure is from [Pay92].

Typically, plane-wave basis sets can be used to expand the wavefunction based on Bloch's theorem. One problem of such expansion is that a large number of basis sets is

required to describe the rapidly oscillating wavefunction in the core region. And this will considerably increase the computation time. However, the physical properties of a solid are mainly determined by its valence electrons rather core electrons. Therefore the pseudopotential approximation is commonly used to replace strong core electron and ionic potential with weaker pseudopotential to reduce plane-wave basis set, while scattering properties of pseudopotential are kept identical to the scattering properties of ion and core electrons. Comparison of all-electron potential and pseudopotential is illustrated in Figure 1.6 [Pay92].

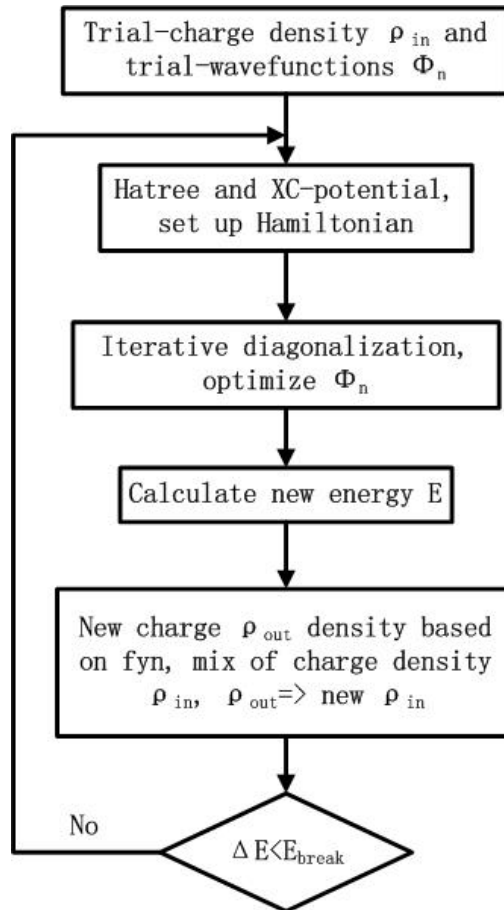


Figure 1.7: Finding total energy using an iterative minimization scheme. The figure is from [Kre07].

Overall, an iterative minimization scheme is needed to relax electron and ion coordinates and obtain total energy. A typical calculation flow can be illustrated in Figure 1.7 [Kre07]. More detailed DFT calculation description can be found in [Pay92] [Kre96a] [Kre96b].

## **1.5 ORGANIZATION**

In the following chapters, I will describe my attempts to understand dopant behavior in complex semiconductor systems. The understandings are gained through experiments, kMC simulation and DFT calculation. Chapter 2 will describe my experimental study of arsenic enhanced and retarded diffusion in point defect engineered silicon. In chapter 3, a kMC simulation is used to further understand and verify the arsenic-interstitial interaction during arsenic TED and deactivation. In chapter 4, I use DFT calculation to reveal the arsenic segregation mechanism at SiO<sub>2</sub>/Si interface. Chapter 5 will discuss a boron diffusion mechanism in amorphous silicon. Conclusions are made in Chapter 6 and future work is also recommended.

## **Chapter 2: Arsenic Transient Enhanced Diffusion in Point Defect Engineered Silicon**

### **2.1 POINT DEFECT ENGINEERING IMPLANT**

In recent years, increasingly research effort has been devoted to point defect engineering implant as a possible solution for dopant Transient Enhanced Diffusion (TED) [Sul98] [Ven00] [Cow05]. It is well known that ion implantation will create interstitials and vacancies in the silicon lattice. As shown in Figure 2.1(a), during the implant, the scattering between dopant atom and silicon lattice will drive the newly created interstitials into the deeper region while leaving the new vacancies in the shallower region. Therefore, after implant, a shallower vacancy-rich (V-rich) region and a deeper interstitial-rich (I-rich) region will be created in the wafer. Silicon implant is typically used to produce this interstitial and vacancy separated distributions, although other species can also be used. The boundary depth of I-rich region and V-rich region is determined by Si implant energy. Higher energy implant will results in deeper boundary and the boundary will be closer to surface for lower energy Si implant. One associated problem is that, during annealing the interstitials from I-rich region will diffuse up to V-rich region and destroy the local vacancy supersaturation by IV annihilation. To avoid this effect, silicon-on-insulator (SOI) wafers are often used. The buried oxide is designed to separate the interstitial and vacancy regions from recombining with each other [Kal01]. If the dopant diffusion/deactivation is via interstitial related mechanism, dopant can be subsequently implanted with proper energy so that the dopant region is overlapped with the shallower vacancy region and therefore the dopant TED and deactivation reactions will be suppressed by IV annihilation, as shown in Figure 2.1(b). Similarly, if the dopant diffusion/deactivation is associated with vacancy mechanism, overlapping with interstitial region will help to reduce TED and deactivation.

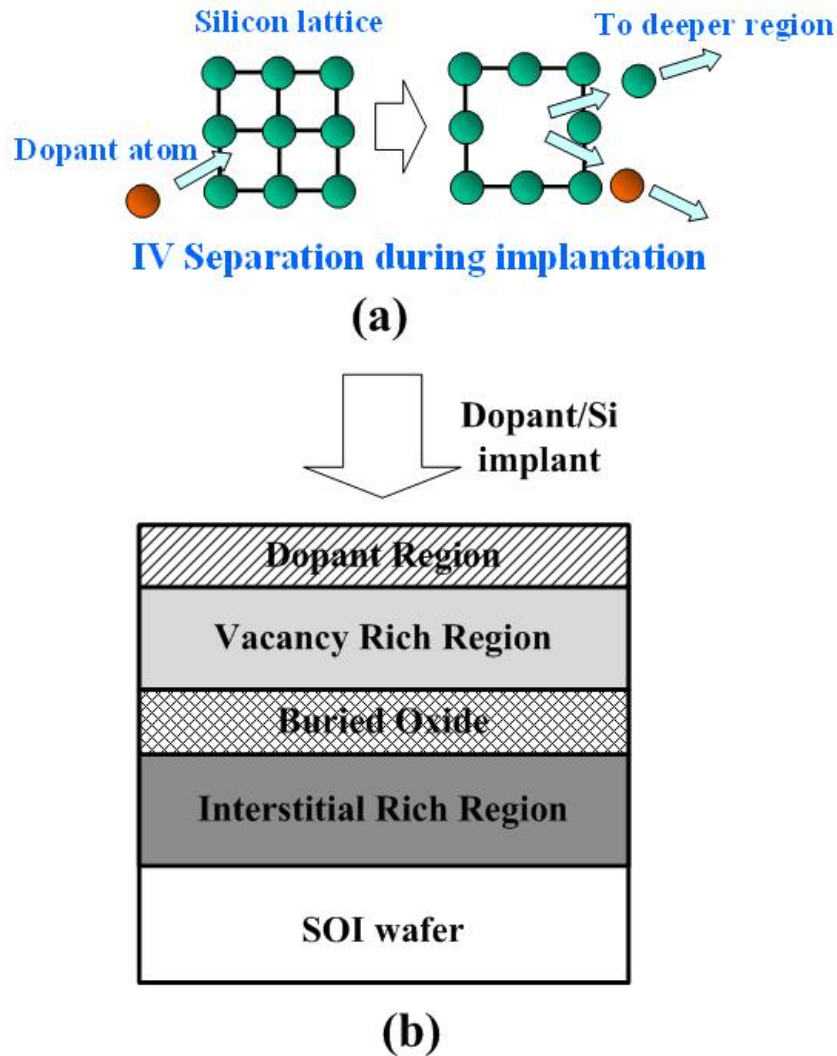


Figure 2.1: Principle of point defect engineering implant: (a) Illustration of interstitial-vacancy separation during ion implantation (b) Dopant, interstitial and vacancy layer distribution of point defect engineered wafers.

This technique has been well studied for boron TED control. Cowern et al. [Cow05] reported substantially shallower junction and lower sheet resistance by placing active boron doping region into the vacancy region created by the extra Si implant. Sultan



et al. [Sul98] reported shallower boron junction depth by employing Si implant before boron implant and anneal to reduce channeling and boron TED. Venezia et al. [Ven00] demonstrated that when two implants superimposed in silicon, vacancies introduced by MeV Si implant will annihilate the interstitials created by keV Si implant and therefore eliminate the boron TED normally associated with keV Si implant.

## 2.2 ARSENIC DIFFUSION MECHANISM

The direct transfer of this technique from boron to arsenic is not that straightforward. One major challenge is that unlike boron diffusion, which is almost solely enhanced by interstitials and retarded by vacancies, arsenic diffusion has been well recognized as a process with both interstitial and vacancy mechanisms [Fah89] [Ura99]. Traditional theoretical and experimental studies [Ram96] [Mat83] support AsV as the major diffusion species for arsenic TED and arsenic vacancy clusters such as As<sub>2</sub>V, As<sub>3</sub>V, As<sub>4</sub>V are the major deactivation factors. However, the possible role of interstitial mediated arsenic TED was also proposed recently [Sol03] [Kim02]. Theoretical study indicated that the interstitial mechanism should not be neglected due to the energetically favorable recombination of As<sub>n</sub>V<sub>m</sub> with interstitials [Har05a] and the lower migration energy (0.4eV) of As<sub>i</sub> pair [Har05a] compared to AsV (0.9eV) [Xie99], especially when interstitial is in excess. The dual mechanism implies that arsenic TED cannot be controlled by placing arsenic either in the interstitial rich region or in the vacancy rich region because both interstitial and vacancy supersaturation will enhance arsenic diffusion.

However, in some practical cases, such as post-implant annealing, it is possible that one of the two types of point defect, interstitial or vacancy, will contribute more to arsenic diffusion than the other. Arsenic TED can be inhibited if this major diffusion

contributor is suppressed. Additional Si implant can be performed to create either interstitial or vacancy excess in the arsenic-implanted region. The major diffusion contributor and diffusion mechanism can then be identified by observing the different arsenic diffusion behaviors within such point defect engineered areas. Based on the results, possible pathways for arsenic ultra-shallow junction (USJ) formation can be suggested.

### 2.3 EXPERIMENTAL DETAILS

Both p-type  $\langle 100 \rangle$   $18 \pm 4 \text{ } \Omega \cdot \text{cm}$  bulk Si wafers and silicon-on-insulator (110nm silicon on oxide layer) wafers were used in the experiments. SOI was used because the buried oxide (BOX) will block the up-diffusion of deeper interstitials and thus keep the shallower vacancy distribution from being recombined. After growing 25 Å screen oxide, we implanted arsenic with energy 5 keV and low dose of  $6 \times 10^{13} \text{ cm}^{-2}$  or high dose of  $1 \times 10^{15} \text{ cm}^{-2}$ . Some samples were annealed at 1025°C for 10s in N<sub>2</sub> atmosphere to remove arsenic implant damage (referred as preanneal). After that, for some samples, Si was implanted with energy 15 keV and dose  $5 \times 10^{13} \text{ cm}^{-2}$  (referred as Si I-rich implant) into bulk Si wafers to produce interstitial rich environments surrounding arsenic. For some other samples, Si was implanted with energy 160 keV and dose  $7 \times 10^{13} \text{ cm}^{-2}$  (referred as Si V-rich implant) into SOI wafers to produce vacancy rich regions overlapping arsenic region. Si V-rich implant into bulk Si wafers was also performed to test the blocking effects of the buried oxide in SOI. Anneals are performed in 700°C for 10min, 750°C for 10min and 1025°C for 5s (referred as postanneal). For samples with no Si implant, control tests proved no significant difference between bulk Si and SOI wafers in as-implanted and diffused arsenic profiles. Secondary ion mass spectrometry (SIMS) analyses of arsenic diffusion profiles were performed by employing 1 keV Cs<sup>+</sup> beams at

an incidence angle of  $60^\circ$ , and detecting  $\text{AsSi}^-$  and  $\text{S}^{3-}$  secondary ions. The Si sputter rate was  $\sim 3.5$  nm/min.

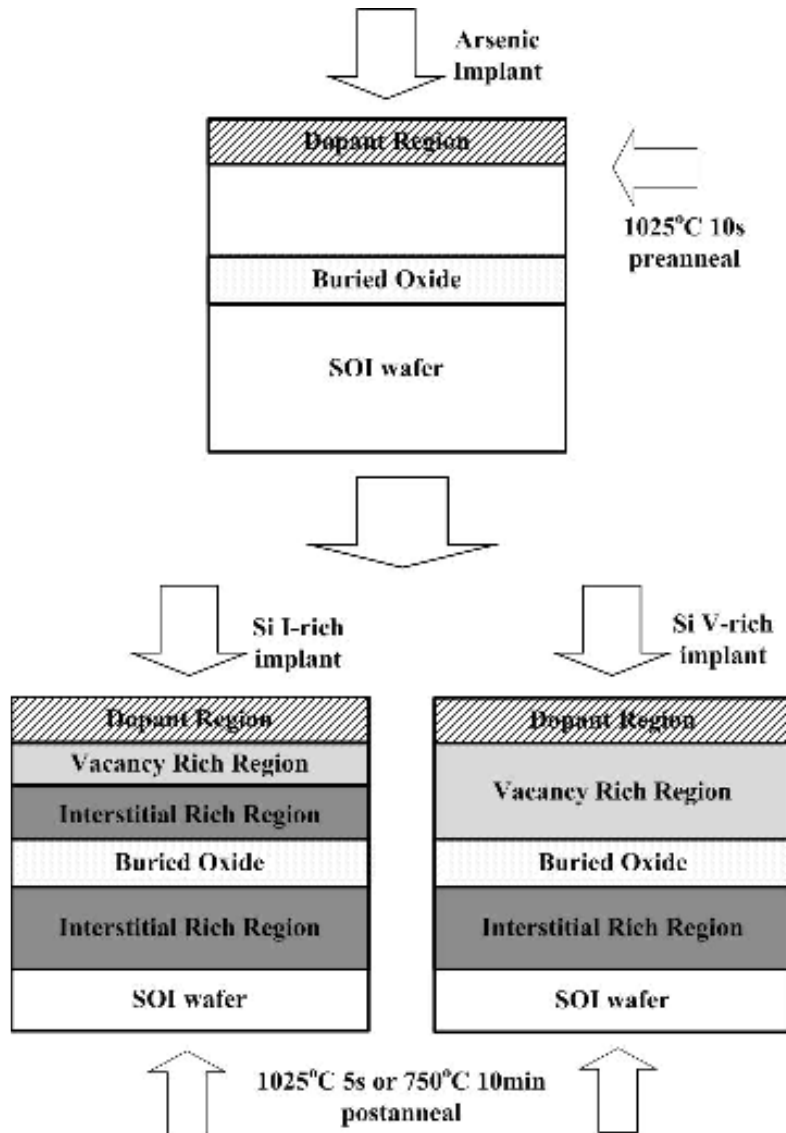


Figure 2.2: Experimental procedure.

The illustration of the experimental steps is shown in Figure 2.2. In Si I-rich implant, the interstitial will diffuse up and cover the vacancy rich region, so arsenic in

this situation is actually in interstitial rich environment compared with arsenic in vacancy rich environment in Si V-rich implant case. That is why we have the name V-rich and I-rich implant. They are used to produce V-rich and I-rich environments around arsenic.

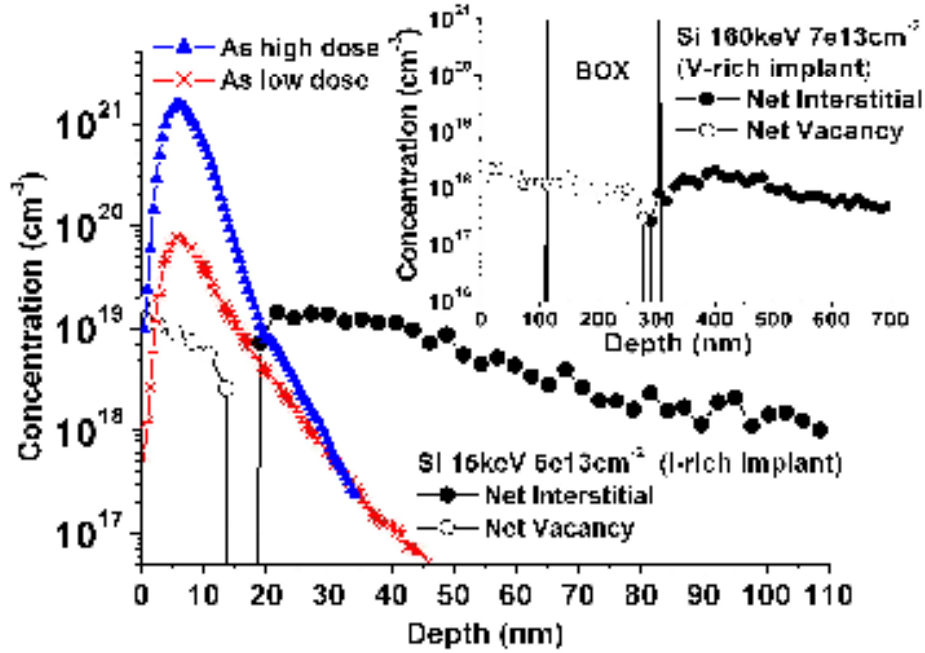


Figure 2.3: UT-MARLOWE simulations of As and Si I-rich/V-rich as-implanted profiles. 5 keV As was implanted with dose  $1 \times 10^{15} \text{ cm}^{-2}$  (triangles) or  $6 \times 10^{13} \text{ cm}^{-2}$  (stars). The net IV separation is shown with open circles denoting net vacancy, and solid circles denoting net interstitial distributions. V-rich implant is shown in the inset.

Monte Carlo simulation of the arsenic and Si I-rich/V-rich implants using UT-MARLOWE [UTM] is shown in Figure 2.3. The IV separation introduced by I-rich implant into bulk Si (Si I-rich implant) will annihilate in the early stage of annealing, leaving a region with excess interstitials, which is due to the introduction of extra Si atoms by implant. The inset shows the blocking effect of BOX for V-rich implant

samples. In our experiments, V-rich implant into both bulk Si (Si V-rich implant) and SOI (SOI V-rich implant) wafers are performed to confirm this blocking effect.

## 2.4 RESULTS AND DISCUSSION

The low dose, non-pre-annealed diffusion profiles are shown in Figure 2.4 (a) and (b). First, the Si V-rich and SOI V-rich implant samples exhibit different diffusion behaviors despite identical implant and annealing conditions. This indicates that in SOI V-rich samples, the up-diffusion of deeper interstitials is effectively blocked by the BOX, which keeps the sub-100nm region V-rich. In contrast, in the Si V-rich samples, the initial IV separation is removed by interstitial up-diffusion, resulting in a net excess of interstitials overlapping the arsenic implant. Second, for both temperatures, arsenic enhanced and retarded diffusion are clearly seen by comparing the Si I-rich/V-rich and SOI V-rich curves with no Si implant curves, respectively. The diffusion enhancement in the interstitial excess region created by Si I-rich or V-rich implant, and retardation in vacancy excess region created by SOI V-rich implant indicate that interstitials are the major contributors to arsenic diffusion during post-implant anneal, and  $As_i$  is a more dominant diffusion vehicle compared to  $AsV$ . A possible reason for retarded diffusion in SOI V-rich samples is that interstitials from arsenic implant damage, which normally contribute to arsenic diffusion during post implant annealing [Sol03], are partially annihilated by vacancies introduced by V-rich implant. Due to a reduced interstitial concentration, the  $As_i$  is less likely to form and thus diffusion is retarded. At a higher temperature, interstitials and vacancies exist for a shorter time due to faster annihilation; thus the enhancement and retardation effects will be smaller, explaining why trends are more pronounced in Figure 2.4 (a) than in Figure 2.4 (b). However, the vacancy supersaturation and the high energy gain of  $As_nV_m$  clustering [Ram96] make it also

possible that the immobile  $\text{As}_n\text{V}_m$  clusters are formed to trap arsenic and retard diffusion, although it may not be the only reason. Small but clear trends (Figure 2.4 (b)) are also seen for 1025°C, 5s post-anneal, which should dissolve most of the clusters [Sol03].

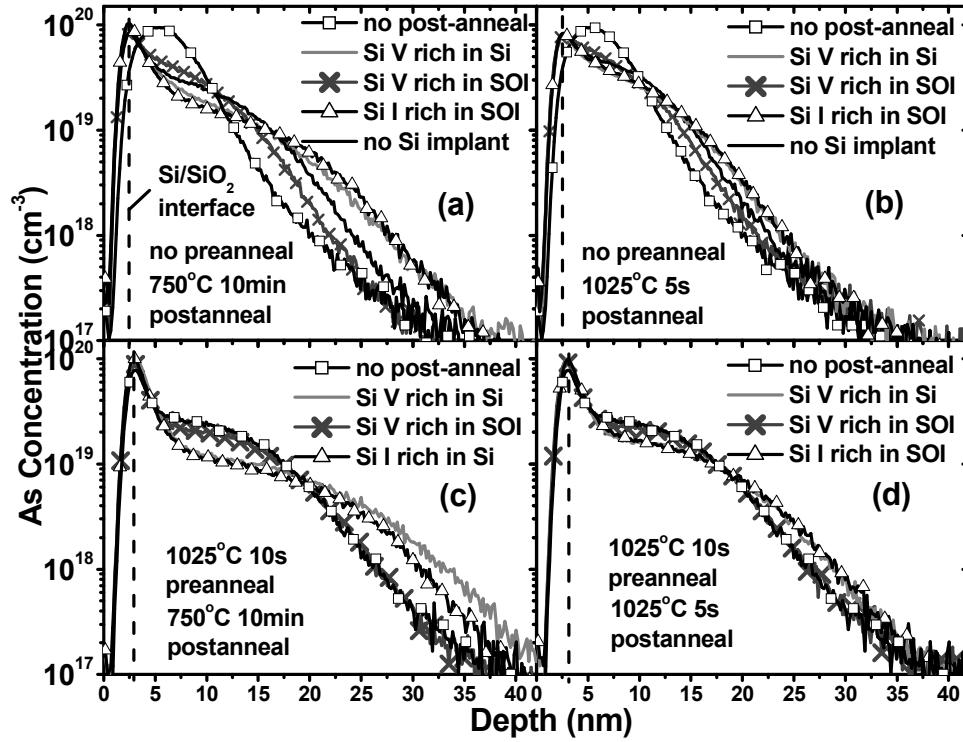


Figure 2.4: SIMS profiles of low dose ( $6 \times 10^{13} \text{ cm}^{-2}$ ) arsenic diffusion. (a) (b) are samples without pre-anneal; (c) (d) are with 1025°C, 10s pre-anneal. Then V-rich (grey line, Si V-rich) or I-rich (triangles, Si I-rich) or no (black line, no Si implant) Si implant into bulk Si, or V-rich Si implant into SOI (cross, SOI V-rich), is performed, followed by a post-anneal of 750°C, 10min as shown in (a) (c), or 1025°C, 5s as shown in (b) (d). The SIMS profiles immediately after pre-anneal are shown as starting curves for post-anneal (square).

To further confirm the role of arsenic implant damage, a 1025°C, 10s pre-anneal was used to remove it immediately after arsenic implant. Other steps remain unchanged. The results are shown in Figure 2.4 (c) and (d).

In Figure 2.4 (c) and (d), instead of observing retarded diffusion as in non-pre-annealed cases, pre-annealed SOI V-rich implanted samples show almost complete absence of diffusion for both temperatures, when compared to the no post-anneal curves. This is compatible with an interstitial-mediated diffusion mechanism. In SOI V-rich samples, most of the arsenic implant damage was removed by pre-anneal and the rest was annihilated with vacancies from V-rich implant. The arsenic region may transiently be rich in vacancies. However, they contribute little to enhanced diffusion since both the activation of a percolation network or  $\text{As}_2\text{V}$ -enhanced diffusion mechanisms requires higher dopant concentration [Xie99] [Mat83]. Also, due to the high diffusivity of vacancies [Fah89] and the close location to the surface, such vacancy supersaturation will disappear in a short time by surface absorption. Therefore, a relatively point-defect-free region was created. Arsenic diffusion, which relies on either interstitial or vacancy mechanism, is thus inhibited due to the lack of diffusion carriers. The “profile freezing” effect extends to arsenic concentrations as low as  $1 \times 10^{17} \text{cm}^{-3}$  and even occurs at temperatures as high as  $1025^\circ\text{C}$ . Since dopant clustering is not likely in such conditions [Sol03], it may not be a major contributor to the retardation effect in low dose cases.

To clarify the retardation role of clustering, which is more obvious in high arsenic concentration regions, we performed the same experiments with a higher arsenic implant dose,  $1 \times 10^{15} \text{cm}^{-2}$ , followed by the same pre-anneal. A lower temperature post-anneal of  $700^\circ\text{C}$ , 10min was added to increase the clustering effects.

Figure 2.5 shows the high dose pre-annealed cases. For SOI V-rich curves, immobile parts appear above arsenic threshold concentrations of  $8 \times 10^{18} \text{cm}^{-3}$  for  $700^\circ\text{C}$  and  $3 \times 10^{19} \text{cm}^{-3}$  for  $750^\circ\text{C}$  post-anneals, but are less obvious for  $1025^\circ\text{C}$  post-anneal samples. This indicates the possible formation of  $\text{As}_n\text{V}_m$  clusters, and thus the possible retardation effects from clustering in a vacancy-rich environment. However, instead of

“profile freezing” observed for low dose counterparts in Figure 2.4 (c) and (d), pre-annealed high dose SOI V-rich samples show visible diffusion in the tail region for all three temperature anneals. The tails could be attributed to the formation of a percolation network and subsequent  $As_2V$ -enhanced diffusion [Xie99]. And this percolation/ $As_2V$  enhanced diffusion is overshadowed by externally introduced interstitials, as shown by the drastically enhanced diffusion in Si I-rich/V-rich implanted samples.

It is interesting to note another manifestation of  $As_nV_m$  clustering. For high dose low temperature post-annealed samples in Figure 2.5 (a) and (b), arsenic profiles for Si V-rich implant cases diffuse much less than for Si I-rich implant cases, while in low dose or high temperature annealed samples as shown in Figure 2.4 and Figure 2.5(c), Si V-rich cases have comparable or even more arsenic diffusion compared with Si I-rich cases. This can be explained by the formation of  $As_nV_m$  clusters, facilitated by abundance of arsenic atoms and vacancies and low annealing temperatures. These clusters retarded the diffusion for high dose Si V-rich samples even when the deeper interstitials diffuse up, as shown in Figure 2.5 (a) and (b). In low dose or high temperature annealing cases, this clustering effect can be neglected.



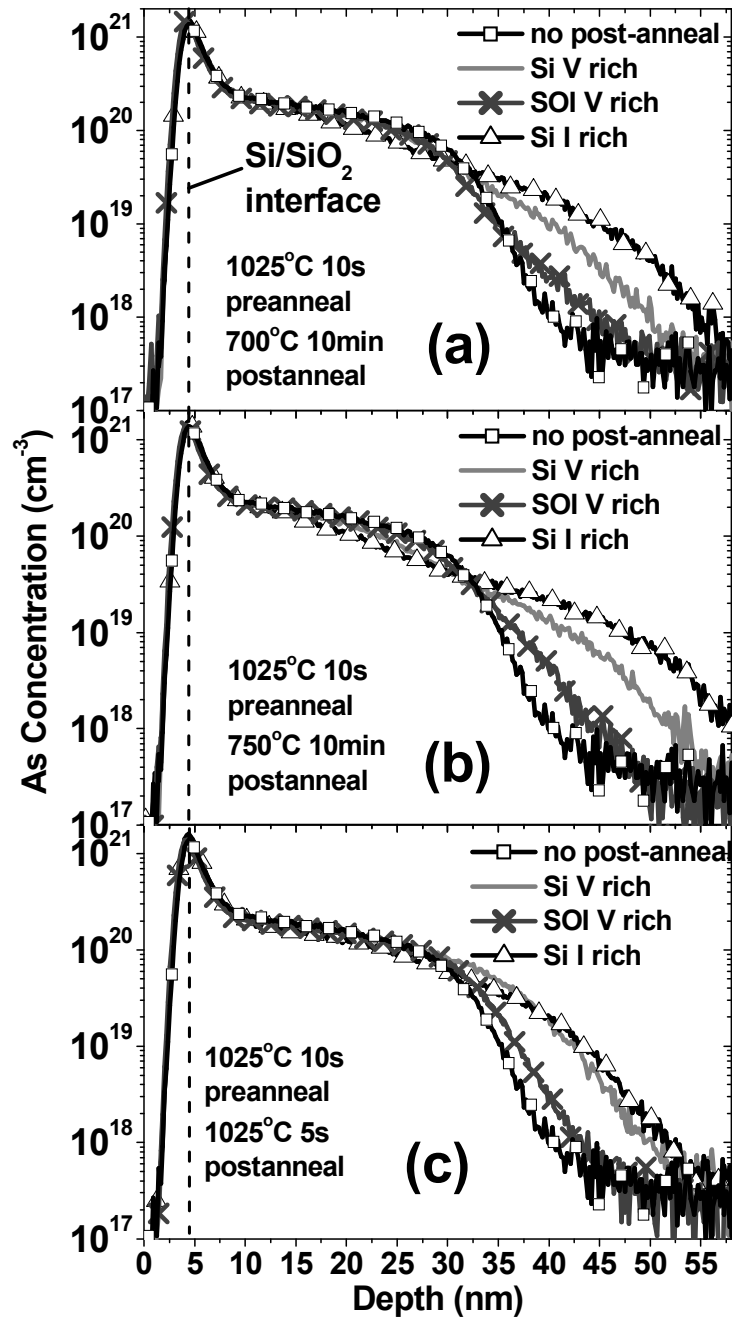


Figure 2.5: SIMS profiles of high dose ( $1 \times 10^{15} \text{ cm}^{-2}$ ) arsenic diffusion. Similar processes as for Figure 2.4 (c) and (d) are used, except for a higher arsenic implant dose. Post-anneals are performed for (a) 700°C, 10min (b) 750°C, 10min (c) 1025°C, 5s.

## 2.5 CONCLUSIONS

In summary, due to the dominant role of the interstitial mechanism during arsenic post-implant annealing, point defect engineering is shown to be an effective approach for controlling arsenic TED for USJ fabrication. The annihilation of local interstitials by externally-introduced vacancies is the major mechanism for arsenic retarded diffusion. The formation of  $As_nV_m$  could also be a possible factor for trapping arsenic and retarding diffusion in the case of high doping concentrations and low temperature anneals.

In terms of process integration, this point defect engineering implant method could be used where shallow arsenic profile is needed. Especially, the point defect engineering implant provides an alternative to solid phase epitaxial regrowth (SPER). As we know, the end-of-range defects created by SPER may lead to junction leakage and is an important source of dopant TED. If point defect engineering is used for TED control, since the Si implant dose used is lower than for SPER, the induced damage could be at a lower level. This method could also be used in SOI devices, where the deep interstitials can be designed in buried oxide layers.

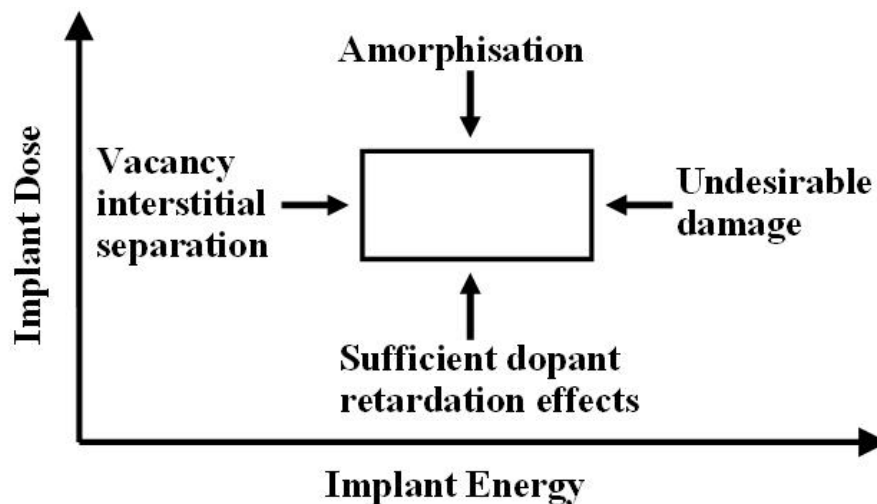


Figure 2.6: Point defect engineering implant energy and dose optimization.

If point defect engineering is to be used, the implant energy and dose should be fine tuned to meet process integration need. For example, as shown in Figure 2.6, the implant dose should be high enough to produce sufficient dopant retardation effects and should be low enough to avoid amorphisation. Too high implant energy may induce undesirable damage to other critical parts of device, while too low implant energy may not create enough vacancy-interstitial separation.

## Chapter 3: Kinetic Monte Carlo Simulation of Arsenic-Interstitial Interaction and Arsenic Uphill Diffusion

### 3.1 INTRODUCTION

The continuous scaling down of silicon transistors requires Ultra Shallow Junction (USJ) technology to alleviate short channel effects. This technology targets precise junction depth control and high dopant activation level. However, dopant Transient Enhanced Diffusion (TED) is often observed to cause anomalous diffusion tails, and the formation of impurity clusters may keep the dopant activation level well below solubility limits. Although these detrimental effects are particularly strong for boron and phosphorus, arsenic TED and clustering also become process challenges as transistor dimension migrates to 45nm node and beyond. Therefore, it is essential to understand arsenic TED and deactivation mechanisms before solutions can be proposed to control these effects.

Arsenic TED was traditionally explained by AsV pairs having low migration barriers within a percolation network [Mat83] [Ram96] [Xie99]. The fast movement of AsV pairs facilitate arsenic agglomeration into deactivating  $As_nV_m$  clusters, such as  $As_2V$ ,  $As_3V$  and  $As_4V$  [Ram96] [Xie99]. However, interstitial mechanism for arsenic TED has also been proposed by recent theoretical and experimental work. Harrison et al. [Har05a], by their density functional theory calculations, suggested that  $As_i$  pair has low migration barrier and may play an important role in arsenic TED. This is especially plausible during post-implant annealing where Si interstitials exist in large numbers [Har04a] [Har05a]. In the previous chapter, we created different point defect environments by Si point defect engineering, and observed retarded arsenic TED in vacancy-rich (V-rich) environments and enhanced arsenic TED in interstitial-rich (I-rich) environments [Kon07]. This further confirmed the interstitial-mediated arsenic TED mechanism. On the other hand, density

functional theory (DFT) calculation suggested that  $As_nI_m$  clusters are less stable than  $As_nV_m$  clusters [Ram96], but they may exist in an interstitial-excess environment as an intermediate state before eventually transferring to  $As_nV_m$  [Har06].

While the key role of interstitial mechanism in arsenic TED has been fully recognized recently, there are no physically-based arsenic-interstitial models in mainstream process simulation tools. In these simulators,  $As_i$  pair diffusion is set to be either identical [Sen07] or negligible [Pin05] compared with  $AsV$  pair diffusion, both of which are contradictory to recent experimental and theoretical findings. As the junction depth scales to sub-50nm range, it becomes clear that without physically-based and well-calibrated arsenic-interstitial interaction models, it is impossible to simulate the arsenic diffusion and deactivation behavior during USJ formation.

The atomistic kinetic Monte Carlo (kMC) simulator DADOS [DAD] is an ideal platform to handle this issue. The kMC approach has been proved to give accurate prediction in many process conditions [Jar96] [Mar04] [Pel99] [Pel03] and has already been included as an option in commercial TCAD tools [AMC07]. The kMC simulation time scales with device size, so it could potentially be the mainstream process simulator in future device design, as shown in Figure 3.1. This approach tracks the behavior of objects ranging from individual point defects or dopant atoms, to larger structures such as  $\{311\}$  extended defects or impurity clusters. Therefore, it can provide a realistic overview of dopant-point defect interaction. However, since the key role of interstitial mechanism in arsenic TED was discovered only recently, both academic DADOS [DAD] and commercial kMC [AMC07] lack physically-based and calibrated arsenic-interstitial interaction models, limiting their predictive capability for arsenic USJ formation especially in Si interstitial-rich environments.

Another effect current kMC fails to simulate is arsenic uphill diffusion [Fer06a]. The uphill diffusion refers to the phenomenon that dopants have a tendency to pileup in the first few nanometers in proximity of the Si/SiO<sub>2</sub> interface during post-implant anneal. This effect was first reported for boron [Wan01] [Duf03] and then found for other dopants, such as P [Duf05] and As [Kas00] [Hop04]. The understanding of this phenomenon becomes imperative in that the pileup portion of the dopant profile may contribute a significant part to the entire activation of the extension junction, which has shrunk to the ~20nm range as the transistor scales down. Since most uphill diffusion involve amorphisation and solid phase epitaxial regrowth (SPER), they were initially explained as the dopant dose “snowplowing” in the advancing Si a/c boundary during SPER and eventually trapped underneath the Si/SiO<sub>2</sub> interface [Van02]. However, later studies found significant uphill diffusion occurs even after SPER is complete [Hop], and also in non-amorphised samples [Kon07]. Currently the uphill diffusion is attributed to dopant TED toward the surface and preferential occupation of lattice site (traps) in proximity of the Si/SiO<sub>2</sub> interface [Fer06a] [Lau89]. Implant-induced point defects, especially interstitials, are suggested to play a key role during this process [Duf03] [Duf05] [Hop04]. Yet the formation kinetics, atomistic structure and activation property of the dopants in this uphill portion are still largely unknown. Thus very few kinetic Monte Carlo studies can be found to address this phenomenon.

In this chapter, DFT-based arsenic-interstitial mechanism is implemented in the atomistic kMC simulator DADOS. The models are calibrated with our previous experiments [Kon07] that highlight the role of interstitial mechanism in arsenic TED. With the new models, we investigate the underlying physics of the arsenic enhanced and retarded diffusion in I-rich and V-rich environments, respectively. The behavior of As<sub>n</sub>I<sub>m</sub> clusters, which are considered to be less stable than As<sub>n</sub>V<sub>m</sub> clusters, but may serve as an

intermediate stage during arsenic deactivation, is also studied in the point-defect engineered regions. A novel surface-trapping-based kinetic Monte Carlo model is introduced into DADOS to simulate the arsenic uphill diffusion effects. By utilizing this model, the important activation behavior of arsenic in this region was studied.

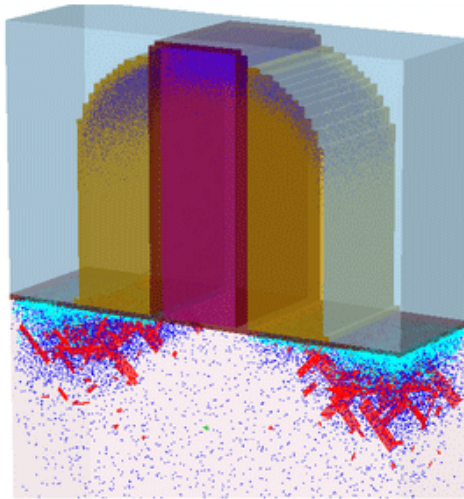


Figure 3.1: Kinetic Monte Carlo simulation used in device level simulation. Red rods indicate the formation of extended defects and light blue species indicate clustered dopant atoms. The picture is from [Syn09].

### 3.2 KINETIC MONTE CARLO SIMULATION

The operation of DADOS modules is shown in Figure 3.2. A brief description for major C++ classes is as following:

**DADOSApp:** Read in parameter files and annealing control files, read in as-implant dopant, interstitial and vacancy profiles from Monte Carlo ion implantation simulators.

**CSimulator:** Annealing initialization, control and coordinate the entire annealing process, timing and temperature control.

**EventManager:** Initializing and updating event rates. Selecting and performing random events. Charge calculation and charge stages update.

**LocationManager:** Point defect jumping in simulation space. All locating related tasks. Deatomize particles/defects for output.

**Particle:** The particle property of an atom, including arsenic, boron,  $As_i$ ,  $As_i^-$ , I, V, etc.

**Defect:** The defect that each atom belongs to, including point defect, cluster, dislocation loop,  $As_nI_m$ , etc.

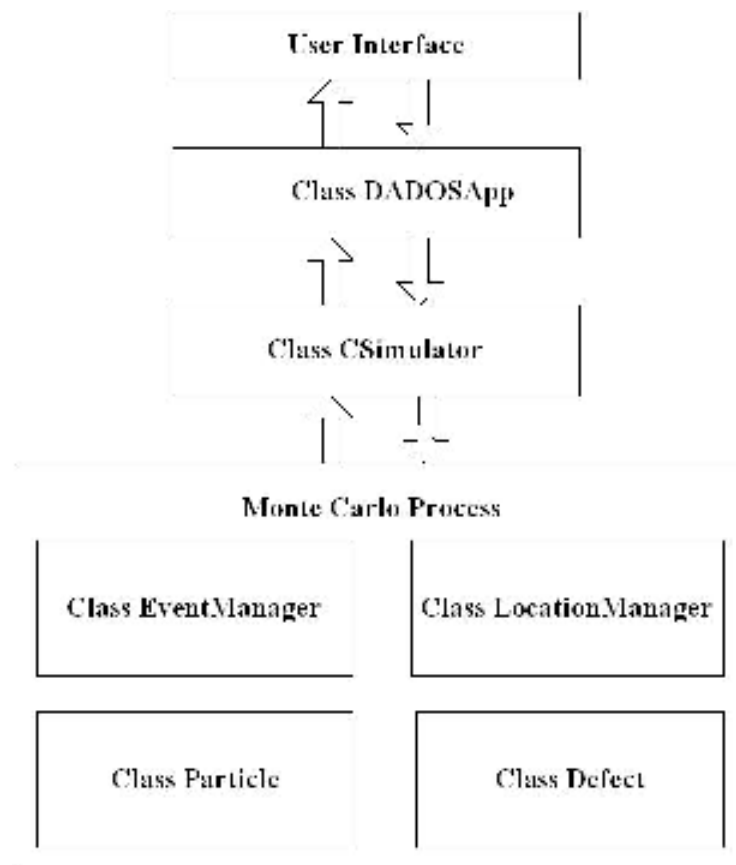


Figure 3.2: DADOS modules organization.



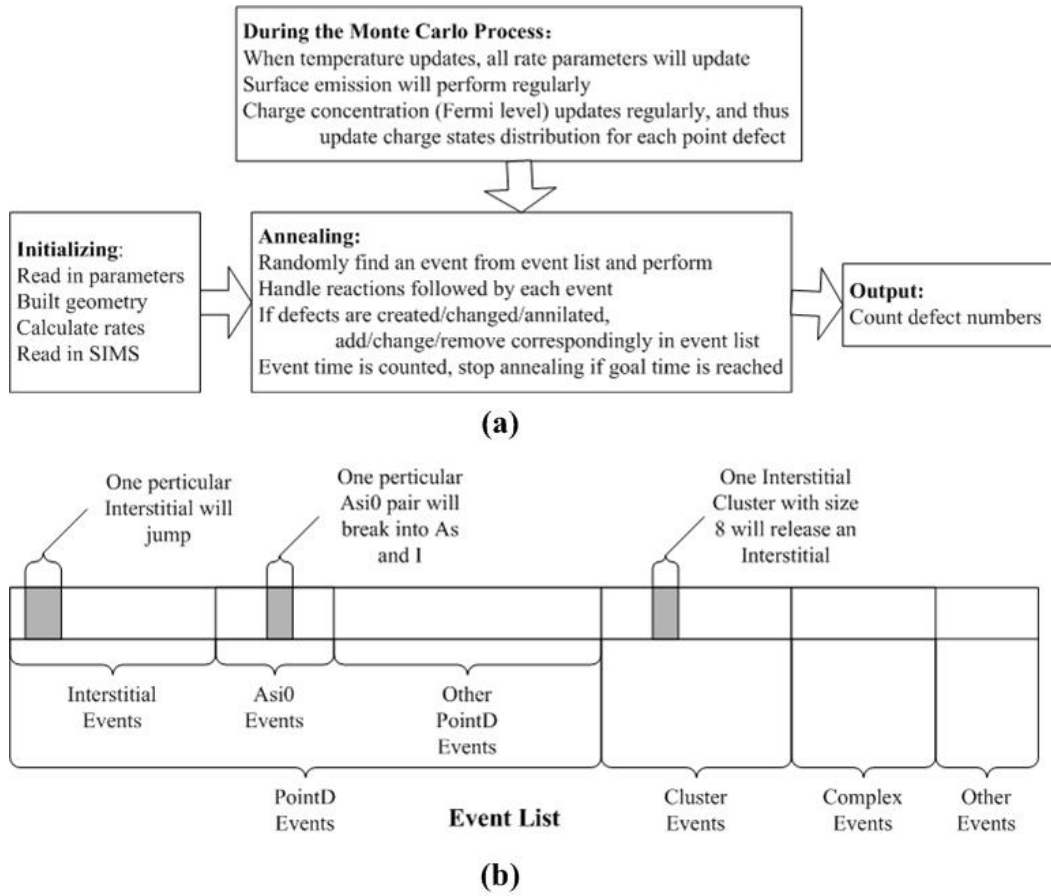


Figure 3.3: DADOS simulation procedure and event list (a) DADOS simulation procedure (b) Event list.

The simulation procedures are shown in Figure 3.3(a). Before annealing starts, annealing control and diffusion parameters are read in, all event rates are initialized. Dopant, interstitial and vacancy distributions are read from Monte Carlo ion implantation simulator, with concentrations atomized into particles in the simulation space. Then, an event list is created as shown in Figure 3.3(b). The event list contains all possible events by all existing particles in the space. When annealing starts, one event is randomly

selected from the event list at one time and performed. The consequences followed by this event are properly handled. For example, after an interstitial jumping events, possible reactions includes: interstitial interacts with a neighboring dopant atom or interstitial joins the nearby I cluster, or IV annihilation, etc. Event list is periodically updated with the insert or remove of defects. And event rate updates with annealing temperature. After one event is performed, another event is randomly selected and performed. The time for each event is recorded and if the annealing time goal is achieved, the annealing stops. Defects are counted and deatomized in output modules.

### **3.3 DADOS MODEL CALIBRATION**

Models in DADOS have been carefully verified and calibrated based on available data from reported experiments. Figure 3.4 is the interstitial and vacancy diffusivity-equilibrium concentration product (DC product) comparison between DADOS and experimental [Bra95] [Cow99a] [Gie00] results. Figure 3.5(a) is the DADOS calibration with interstitial supersaturation evolution measured by [Cow99b]. And Figure 3.5(b) is the calibration with time evolution of interstitials trapped in clusters/{311} extended defects reported by [Sto97]. Figure 3.6 is an example of boron diffusion calibration [Cow91] and Figure 3.7(a) (b) (c) and (d) show examples of boron TED and clustering simulation compared with experiments [Pel97].

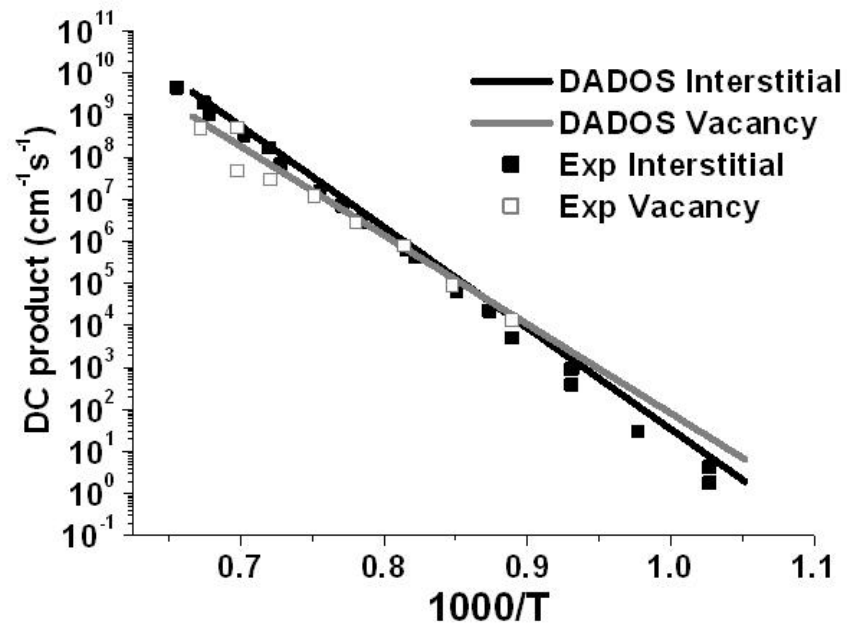


Figure 3.4: Comparison of DADOS with experiments: DC products for interstitial and vacancy [Bra95] [Cow99a] [Gie00].

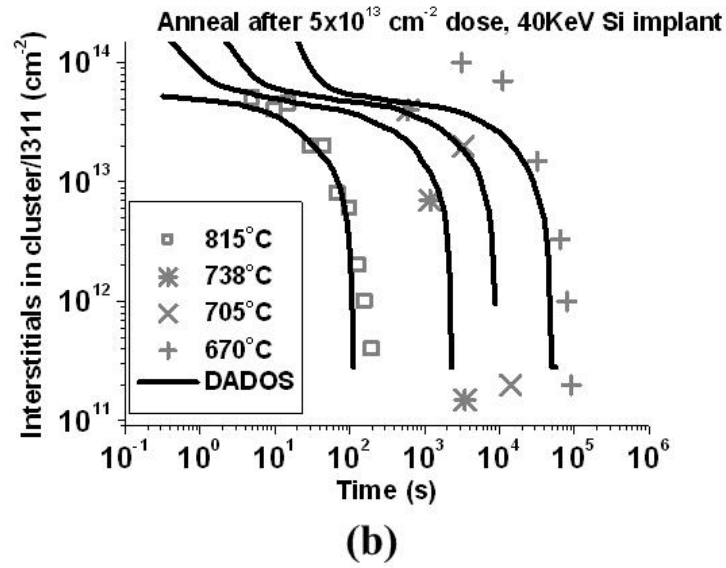
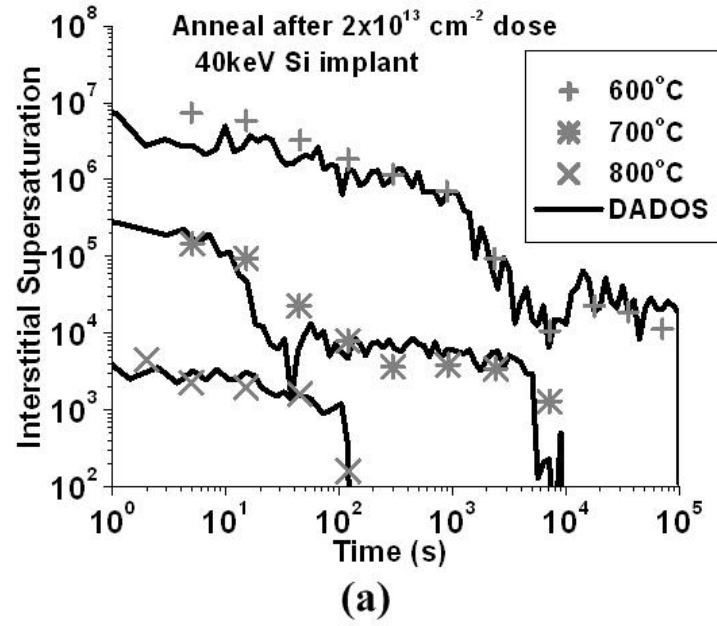


Figure 3.5: Comparison of DADOS with experiments: point defect evolution (a) Time evolution of interstitial supersaturation [Cow99b], (b) Time evolution of interstitials trapped in clusters/ $\{311\}$  [Sto97].

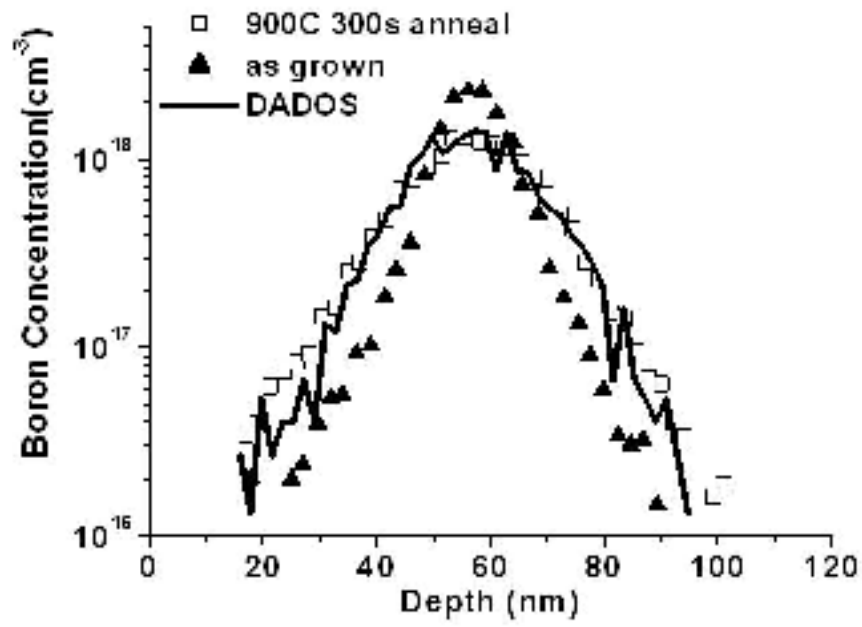


Figure 3.6: Comparison of DADOS with experiments: boron diffusion [Cow91].

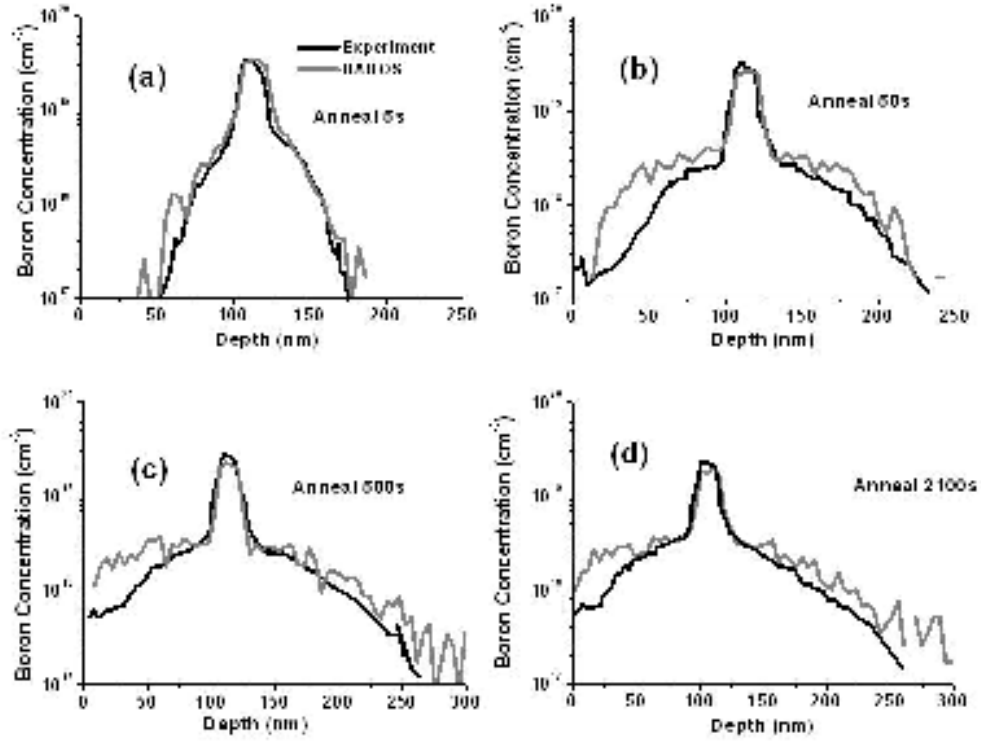


Figure 3.7: Comparison of DADOS with experiments: boron TED and clustering [Pel97].

### 3.4 MODEL DESCRIPTION

In DADOS simulations, initial as-implanted dopant and damage profiles are converted to particles in the simulation space. These particles represent diffusion species such as dopant and point defects. During annealing, a variety of events are simulated according to predetermined physical mechanisms. Examples for these events are dopant-point defect interactions, front surface emission/absorption, dopant-vacancy pair jumping,  $\{311\}$  extended defects releasing interstitials, etc. Specifically, arsenic diffusion is controlled by the following reactions:



Substitutional arsenic  $\text{As}_s$  is immobile and active.  $\text{As}_i$  and  $\text{AsV}$  species represent the two major arsenic diffusion mechanisms. The superscripts denote charge states for each species. There can be translations between different charge states, for example:



According to DFT studies, diffusion species in different charge states generally have different migration barriers. The interstitial cluster/{311} and vacancy cluster models are based on [Cow99b] and [Bon98].

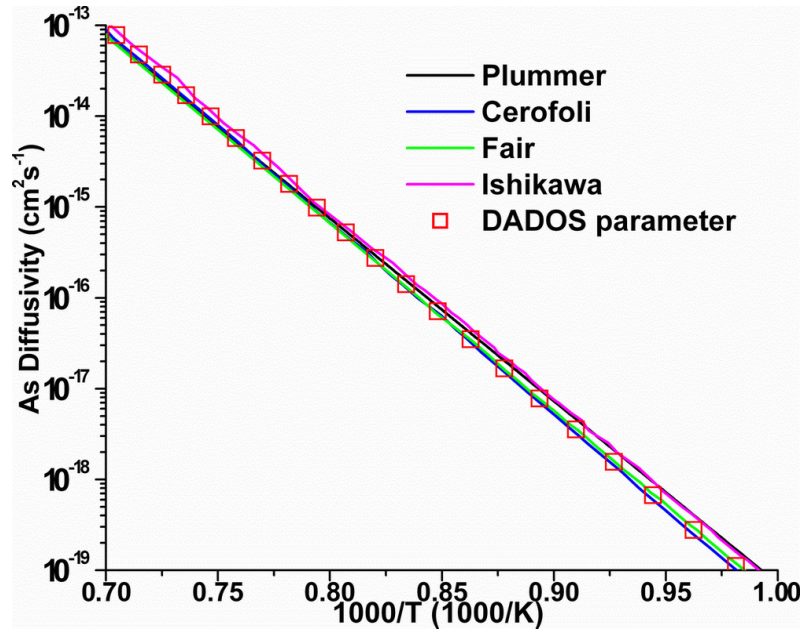


Figure 3.8: Arsenic intrinsic diffusivity: Lines are experimental values from different references [Plu00] [Cer86] [Fai81] [Ish82]. Void squares show the theoretical values calculated by DADOS parameters.

The DADOS  $As_i$  pair models in previous study [Pin05] (referred as “previous models” in the following) are non-physically based with higher activation energies compared with  $AsV$  pair. Also, the models ignore the diffusion of  $As_i^-$  charged state. All the above disagree with recent DFT calculation [Har05a] that  $As_i$  has generally low migration barriers and  $As_i^-$  has significant contribution to both intrinsic and extrinsic arsenic diffusion. Therefore, the previous models may lead to an underestimation of  $As_i$  contribution to arsenic TED. In our simulation, DFT-based arsenic interstitial pair models and parameters are used, as shown in Table 3.1. Our arsenic diffusion parameters are compatible with arsenic intrinsic diffusion experiments [Plu00] [Cer86] [Fai81] [Ish82], as shown in Figure 3.8. And the ratio of diffusion via interstitial mechanism and via vacancy mechanism falls within the range reported in previous literature [Ura99].

The dopant deactivation in previous models has only been based on  $As_nV_m$  clusters. However, in this work,  $As_nI_m$  clustering mechanism is implemented to address its possible intermediate role during arsenic deactivation. The  $As_nI_m$  clusters include  $As_2I$ ,  $As_3I$  and  $As_4I$ , with binding energies based on DFT calculation, as shown in Table 3.2. The  $As_nI_m$  and  $As_nV_m$  clusters with  $m>1$  are not included in this simulation because they have much less impact on the clustering mechanism and simulation results than  $As_nI$  and  $As_nV$  clusters [Ram96] [Har06] [Pan88] [Law95] [Ber98]. The clustering reaction includes:

Trapping/Emission:



Recombination/Frank Turnbull process:



Complementary Recombination/Emission:





The evolution process can therefore be illustrated as in Figure 3.9. Although the final products are mostly energetically-favorable  $\text{As}_3\text{V}$  and  $\text{As}_4\text{V}$  clusters upon adequate thermal treatment,  $\text{As}_n\text{I}_m$  mediated evolution will also provide important insight into the entire deactivation process.

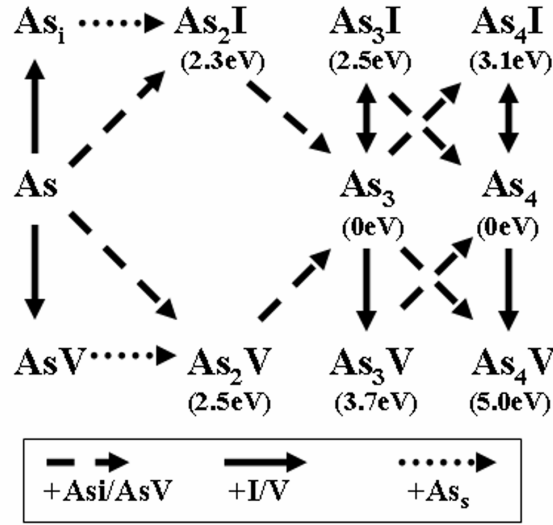


Figure 3.9: New models implemented in DADOS.

Although the underlying physics is still largely unclear, boron and phosphorous uphill diffusion effects have been suggested to be initiated by interstitial-assisted dopant transport towards the Si/SiO<sub>2</sub> interface region [Duf03] [Duf05]. The existence of energetically preferable “trap” sites beneath the Si/SiO<sub>2</sub> interface has also been proposed to explain this pileup effect [Fer06a] [Duf05]. In our simulation, a “transport and trap” mechanism is implemented in order to simulate the arsenic uphill diffusion. The  $\text{AsV}$  and  $\text{As}_i$  pairs that diffuse into the Si/SiO<sub>2</sub> interface region can be trapped by some

energetically favorable sites “Trap” into immobile and stable state “AsT”. The trapping process can be described by:



A virtual, immobile particle “Trap” is initially introduced within 5 nm from the Si/SiO<sub>2</sub> interface, with distribution:

$$\text{Trap Concentration} = 1.131 \times 10^{20} \exp\left(\frac{-\text{depth}(\text{nm})}{0.85}\right) \text{cm}^{-3} \quad (10)$$

The fitting parameter  $1.131 \times 10^{20}$  and 0.85 in the above empirical distribution were calibrated with our arsenic diffusion profiles for different anneal and point defect conditions, as shown in Figure 3.10 (a)-(f). These parameters are applied for all simulations throughout this work.

After the model verification by a variety of implant and annealing conditions, most of the analysis in this work (Figure 3.11, 3.12, 3.13, 3.14, 3.15 and 3.16) is based on the experiments where arsenic is implanted into Silicon-On-Insulator (SOI) wafers with energy 5 keV, dose  $6 \times 10^{13} \text{ cm}^{-2}$ , followed by Si I-rich (15 keV,  $5 \times 10^{13} \text{ cm}^{-2}$ ), Si V-rich (160 keV,  $7 \times 10^{13} \text{ cm}^{-2}$ ) or no Si implant, followed by 750°C 10 min or 1025°C 5 s anneal. This recipe shows the most obvious arsenic enhanced and retarded diffusion and thus contains significant TED physics. Figure 3.11 also uses the results of some control experiments in which a 1025°C 10 s anneal was performed immediately after arsenic implant to remove implant damage. Detailed process conditions can be found in [Kon07].

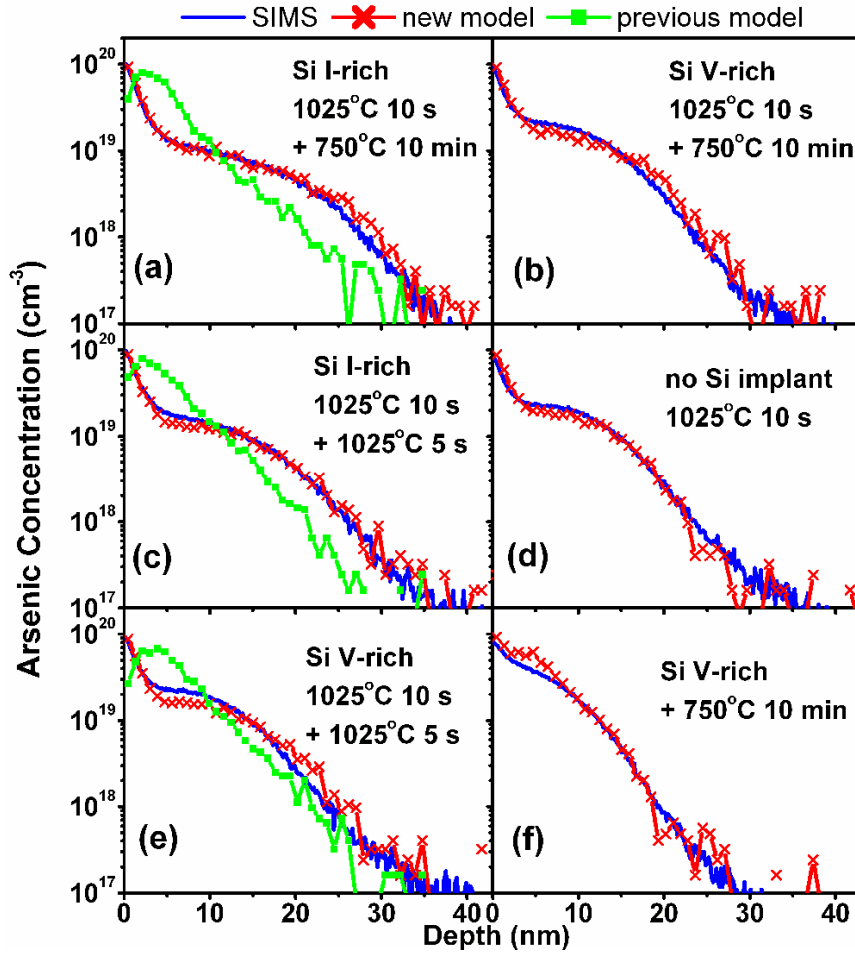


Figure 3.10: Arsenic diffusion SIMS profiles [Kon07] and DADOS simulation. Blue curves are SIMS profiles. Red cross curves are DADOS simulation with arsenic-interstitial mechanism implemented. Green square curves are DADOS simulation with the previous models. All diffusion and Si implant steps are after a 5 keV,  $6 \times 10^{13} \text{ cm}^{-2}$  arsenic implant. The profiles start from the Si/SiO<sub>2</sub> interface.

For DADOS simulations, as-implanted dopant profile, interstitial and vacancy profiles are the three major input files. Arsenic as-implanted SIMS profile is directly used as initial dopant input while UT-Marlowe simulation [UTM] is used to obtain the

interstitial and vacancy profiles generated by arsenic and silicon implant. The dopant profiles simulated by UT-Marlowe are found to agree with the as-implanted arsenic SIMS measurements. To simulate the blocking effect of oxide layer in V-rich case, damage profiles by the high energy Si V-rich implant are truncated and only the first 110 nm (the thickness of the SOI layer) profiles are used as input. Point defects and dopants will sink in SOI and buried oxide interface, while periodic boundary conditions are applied in the horizontal direction. Sheet resistance is obtained by Sentaurus Process extraction [Sen07] of the active arsenic profiles from the kMC simulation.

	$D_{m0}(\times 10^{-3} \text{ cm}^2/\text{s})$	$E_m(\text{eV})$	$e_t-e_v(T=0)(\text{eV})$	$E_f(\text{eV})$	$E_b(\text{eV})$
$V^{++}$	1.0	0.8	1.06		
$V^+$	1.0	0.6	0.6		
$V^0$	1.0	0.4		3.8	
$V^-$	1.0	0.4	0.03		
$V^{--}$	1.0	0.3	0.13		
$I^+$	50	0.8	1.0		
$I^0$	50	0.8		3.97	
$I^-$	50	0.8	0.35		
$As_i^+$	1.3	0.78	0.26		0.25
$As_i^0$	1.3	0.87			
$As_i^-$	1.3	0.89	0.85		
$AsV^+$	0.8	1.3	0.3		1.01
$AsV^0$	0.8	1.75			
$AsV^-$	0.8	1.57	0.77		

Table 3.1: Atomistic parameters of the species related with arsenic TED. Charge states are denoted by superscripts. Arsenic interstitial pair migration energies ( $E_m$ ), binding energies ( $E_b$ ) and ionization levels ( $e_t-e_v$ ) are based on [Har05a]. Other parameters are based on [Pin05].

	As <sub>2</sub> V	As <sub>3</sub> V	As <sub>4</sub> V	As <sub>2</sub> I	As <sub>3</sub> I	As <sub>4</sub> I
Binding Energy (eV)	2.5	3.7	5.0	2.3	2.5	3.1

Table 3.2: Arsenic cluster binding energies. Parameters based on [Ram96] and [Har06].

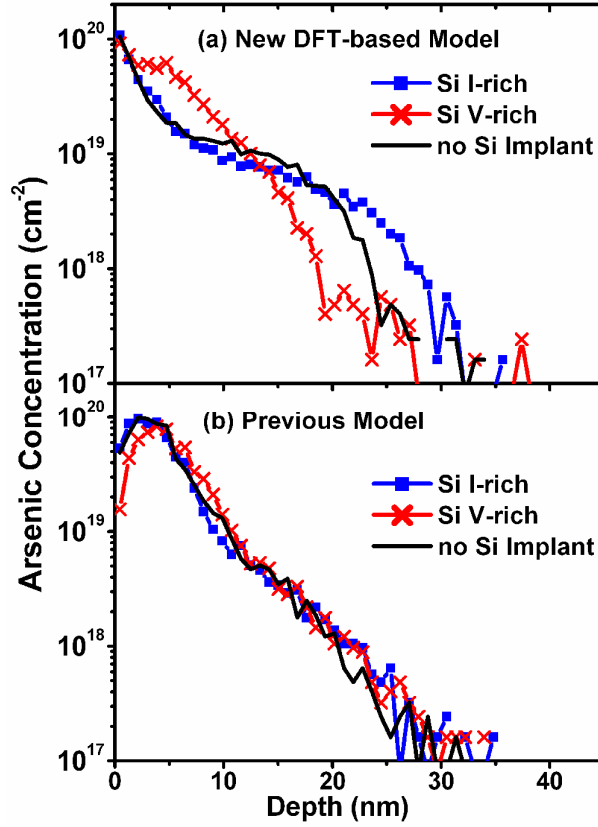


Figure 3.11: Enhanced and retarded arsenic TED by DADOS simulation. Profiles are obtained after 5 keV,  $6 \times 10^{13} \text{ cm}^{-2}$  arsenic implant, I-rich/V-rich/no Si implant and 750°C 10 min anneal.

### 3.5 SIMULATION RESULTS AND DISCUSSION

With the physically-based arsenic-interstitial models implemented, our simulation results show excellent agreement with experimental SIMS profiles, as shown in Figure

3.10. The good matches can be obtained in a variety of point defect engineering and annealing conditions. Moreover, as shown in Figure 3.11 (a), our simulation is able to reproduce the arsenic enhanced and retarded diffusion in I-rich and V-rich environments, respectively. On the other hand, simulation with previous models can also give correct tail prediction to arsenic TED in V-rich condition, as shown in Figure 3.10 (e). However, it underestimates the  $As_i$  contribution to arsenic TED due to the unphysical arsenic-interstitial interaction models, such as too large  $As_i$  pair migration barriers and small  $As_i$  pair binding energies, etc. Therefore it underestimates junction depth for arsenic TED in I-rich conditions, as shown in Figure 3.10 (a) and (c), and cannot predict the arsenic enhanced and retarded diffusion effects, as shown in Figure 3.11 (b).

In addition, with the surface trapping mechanism implemented, our models have much better prediction of arsenic profiles in the close-to-interface region compared to previous models, as can be seen in Figure 3.10 (a) (c) and (e). The uphill peaks are primarily contributed by the trapped arsenic  $As_T$ . The activation behavior of the arsenic in this region will be discussed in detail later.

In order to clarify the mechanism of enhanced and retarded arsenic diffusion, it is necessary to track the time evolution of some key diffusive species such as free interstitials and vacancies,  $As_i$  and  $AsV$  pairs, in different point defect environments. Our analysis is primarily based on 5 keV,  $6 \times 10^{13} \text{ cm}^{-2}$  arsenic implant with 750°C 10 min anneal samples because they show the most obvious enhanced and retarded diffusion trends and thus are most suitable for illustrating underlying physics. It is important to note that the mechanism discussed in this work also applies for high dose arsenic implant (5 keV,  $1 \times 10^{15} \text{ cm}^{-2}$ ) and high temperature anneal (1025°C 5 s) cases, which have been experimentally demonstrated [Kon07] to show the same enhanced and retarded diffusion effects.

First, the time evolution of point defects in I-rich, V-rich and no Si implant environments are examined. As shown in Figure 3.12, free interstitial concentration is the highest in I-rich case and is well suppressed in V-rich case, which was our point defect engineering goal. The long-lasting interstitial supersaturation in I-rich case results from the dissolution of small interstitial clusters and  $\{311\}$  defects during annealing. On the other hand, free vacancy concentration is the highest in V-rich case and the vacancy supersaturation is maintained throughout the annealing process, by means of vacancy emission from vacancy clusters. Initially, vacancy concentration in I-rich case is higher than that in no Si implant case due to the extra vacancies introduced by I-rich implant. Eventually, these vacancies will either agglomerate into  $As_nV_m$  clusters or annihilate with excess interstitials.

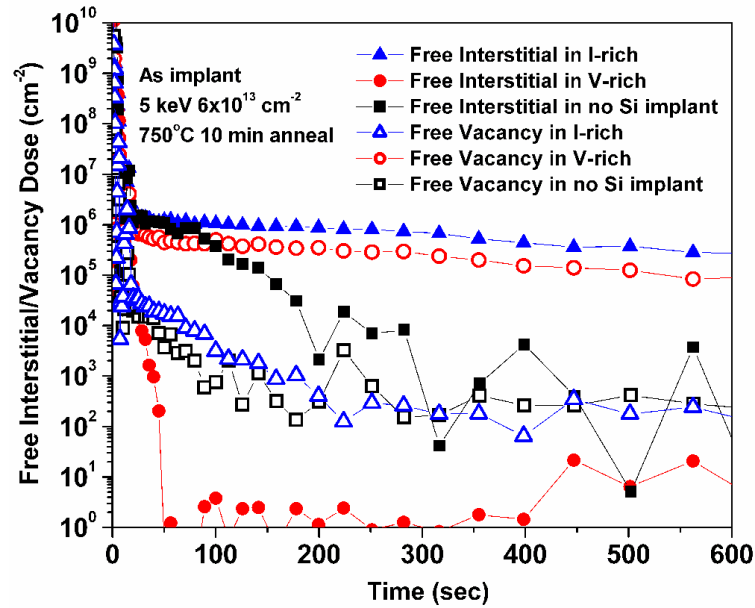


Figure 3.12: Time evolution of free point defect concentrations during annealing after I-rich/V-rich/no Si implants. Implant and annealing conditions are the same as for Figure 3.11.

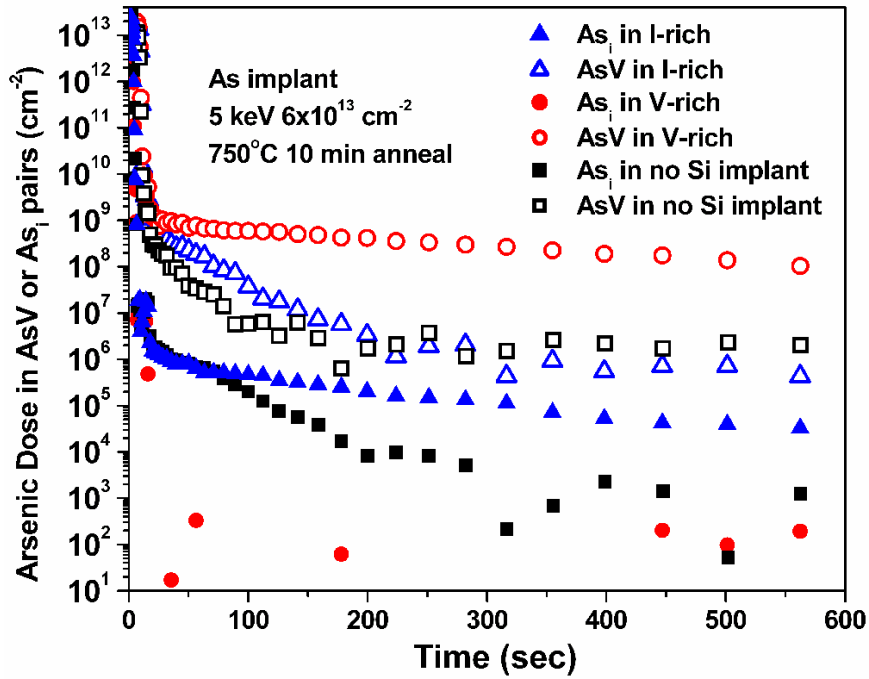


Figure 3.13: Time evolution of  $\text{As}_i$  pair and  $\text{AsV}$  pair concentrations during annealing after I-rich/V-rich/no Si implants. Implant and annealing conditions are the same as for Figure 3.11.

Next, the time evolution of  $\text{As}_i$  and  $\text{AsV}$  pairs are investigated in cases of I-rich, V-rich and no Si implant situations, as shown in Figure 3.13. The concentration of  $\text{AsV}$  in V-rich case is much higher than those in I-rich and no Si implant cases, which is expected because arsenic is more likely to pair with the excess vacancies introduced by Si V-rich implant. If arsenic TED is mainly through  $\text{AsV}$  pair diffusion, we should expect an highly enhanced arsenic diffusion tail in V-rich environment due to a highly enhanced  $\text{AsV}$  pair concentration. However, as can be seen from Figure 3.11 (a), the highest concentration of  $\text{AsV}$  in V-rich case corresponds to the most retarded diffusion tail, which suggests an insignificant TED contribution from  $\text{AsV}$  diffusion in this situation. On the other hand,  $\text{As}_i$  concentration is the highest in I-rich case and lowest in V-rich



case, which is similar to the interstitial concentration trend, as shown in Figure 3.12. This trend is fully compatible with the arsenic enhanced diffusion in I-rich case and retarded diffusion in V-rich case, if the dominant role of arsenic interstitial diffusion mechanism is assumed. The simulation suggests that although  $As_i$  pair has lower concentration than  $AsV$  pair due to a lower binding energy, a much lower migration barrier enables it to contribute significantly to arsenic TED, especially in post-implant situation where interstitial concentrations are high.

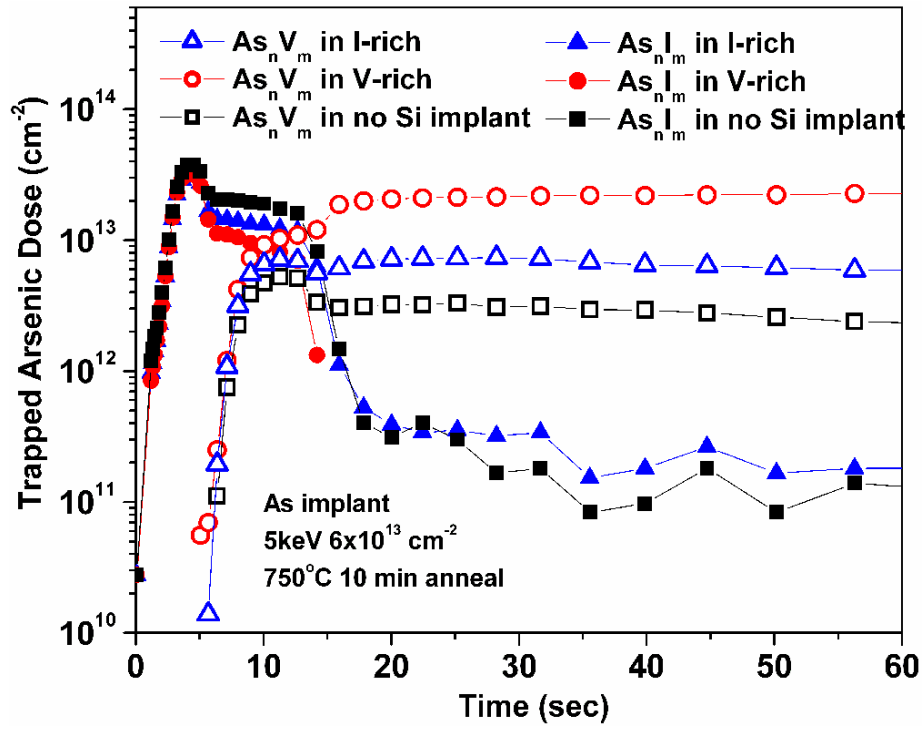


Figure 3.14: Time evolution of arsenic dose trapped in  $As_nI_m$  clusters and  $As_nV_m$  clusters during annealing after I-rich/V-rich/no Si implants. Implant and annealing conditions are the same as for Figure 3.11.

Another factor that might cause the retardation effect is  $As_nV_m$  or  $As_nI_m$  clustering [Kon07], which is even more important in modeling arsenic deactivation during TED.

Figure 3.14 illustrates the evolution of the arsenic dose that is trapped in  $As_nV_m$  or  $As_nI_m$  clusters during anneal. The simulation shows that the  $As_nI_m$  clusters appear transiently within the first 15 seconds, mostly in the form of  $As_2I$ . The decrease of these clusters happens quickly thereafter, accompanied by a drastic rise of  $As_nV_m$  clusters, which dominates over the  $As_nI_m$  clusters during the rest of the annealing process. The initial appearance of  $As_2I$  clusters can be largely attributed to the reaction:

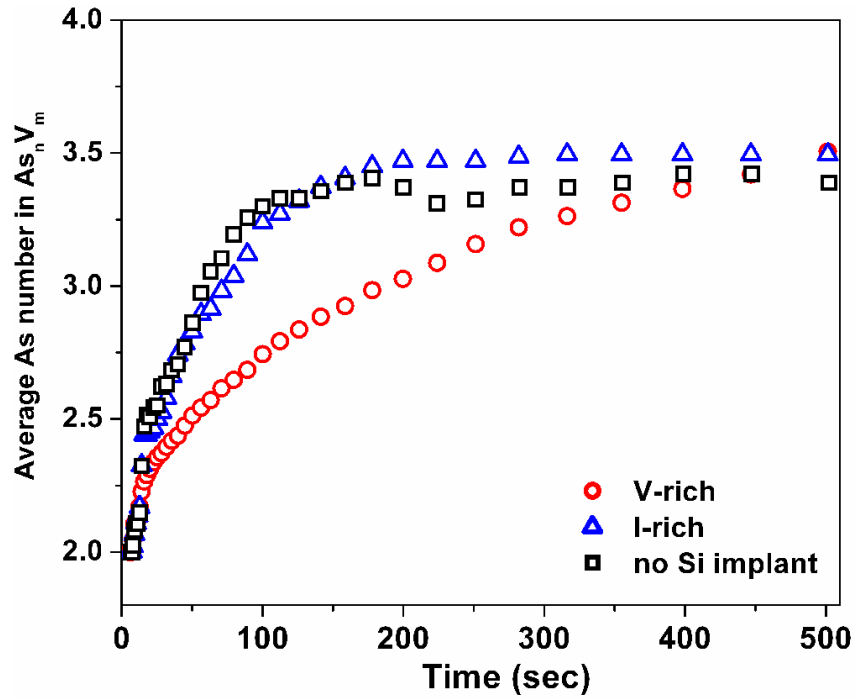


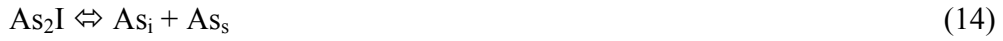
Figure 3.15: Time evolution of average arsenic number in  $As_nV_m$  clusters, for I-rich, V-rich and no Si implant cases. Implant and annealing conditions are the same as for Figure 3.11.

Since most as-implanted arsenic atoms are not in substitutional positions,  $As_s$  is the limiting factor in the above reaction. Also considering that  $As_i$  and  $As_2I$  can be easily

suppressed by extra vacancies via IV recombination, one can explain why  $\text{As}_2\text{I}$  concentration in the no Si implant case is slightly higher than either I-rich or V-rich cases, in which extra vacancies are introduced by the Si implant. Due to the less favorable binding energies compared with  $\text{As}_n\text{V}_m$  clusters, the initial  $\text{As}_2\text{I}$  clusters will transfer to more stable  $\text{As}_2\text{V}$  cluster by absorbing free vacancies:



or by breaking up and reconstructing:



This mechanism is compatible with the recent theoretical calculation with respect to the role of  $\text{As}_2\text{I}$  in arsenic clustering [Har05b]. Moreover, the  $\text{As}_2\text{I}$ -based clustering agrees well with a previous experimental observation [Bri99], in which low dose arsenic are found to trap interstitials and the ratio of As and I was estimated to be 2:1. As shown in Figure 3.15, during annealing, the  $\text{As}_n\text{V}_m$  clusters will evolve from low index  $\text{As}_2\text{V}$  clusters to high index, more stable  $\text{As}_3\text{V}$  and  $\text{As}_4\text{V}$  clusters. This transition is slower for V-rich samples due to the abundance of AsV species, which will enhance the reaction:



Eventually most of the clustered arsenic is in the form of energetically favorable  $\text{As}_3\text{V}$  or  $\text{As}_4\text{V}$  clusters, together with a few  $\text{As}_4\text{I}$  clusters in I-rich and no Si implant cases. Although  $\text{As}_n\text{I}_m$  is not the major clustering component in this situation, their transient appearance during post-implant anneal might make it important in short time anneals such as laser anneal or spike anneal.

As shown in Figure 3.14, almost half of the arsenic dose in V-rich case is trapped in  $\text{As}_n\text{V}_m$  clusters. This might not be the sole reason for the retarded diffusion in V-rich

case because the arsenic dose in  $As_nV_m$  cluster is also higher in I-rich case than in no Si implant case but only enhanced diffusion is observed in this situation. However, it implies that the retardation by  $As_nV_m$  clustering cannot be ignored, especially in V-rich environments.

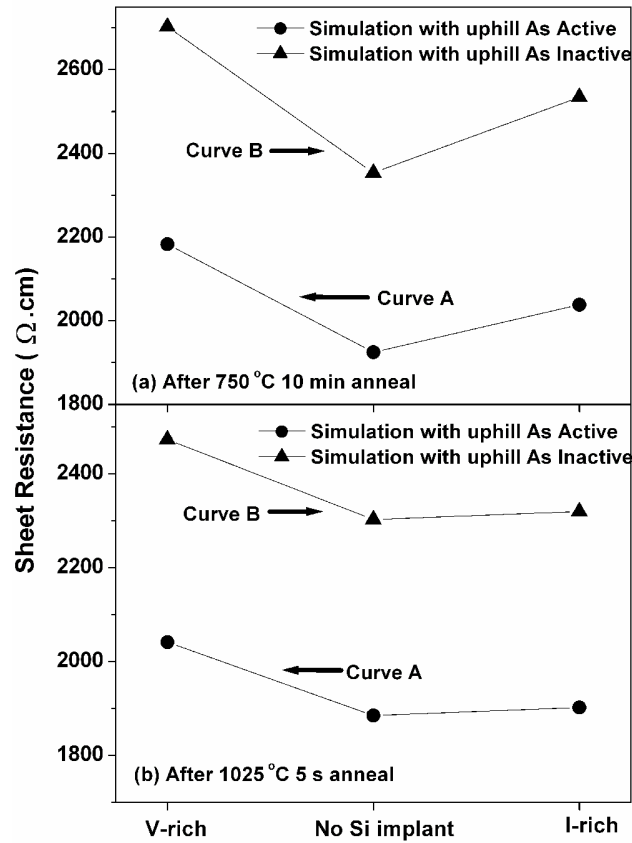


Figure 3.16: DADOS simulated sheet resistance. Samples are implanted by 5 keV,  $6 \times 10^{13} \text{ cm}^{-2}$  arsenic, followed by I-rich/V-rich/no Si implants and then followed by (a) 750°C, 10min and (b) 1025°C, 5s anneal.

Moreover, the high dose of arsenic trapped in  $As_nV_m$  clusters suggests that these clusters have significant contribution to arsenic deactivation, especially in V-rich samples. However, in ultra shallow arsenic implant cases, the deactivation role of uphill

arsenic may also be important. Although dopant uphill diffusion was proposed as a potential ultra shallow junction solution during the first time it is reported [Fer06a], the understanding of its activation behavior is still quite limited. Few studies clearly indicate whether the portion of arsenic that constitutes the uphill layer is active or not, and how important it is to the entire activation level. In Figure 3.16, we extract the sheet resistance from active arsenic profiles simulated for V-rich, I-rich and no Si implant conditions. To distinguish the role of uphill arsenic,  $R_s$  is extracted separately by assuming the “AsT” portion of arsenic active or inactive, shown as curve A and curve B, respectively.

According to Figure 3.16, the  $R_s$  difference between curve A and curve B can be as high as 20%, indicating the significant role of the uphill layer to the entire dopant activation, and that can mask the variation between V-rich and I-rich samples. This suggests that although arsenic TED is mainly controlled by the point defect environment, the activation level can be impacted by both arsenic-point defect clustering and uphill diffusion. This  $R_s$  contribution from uphill arsenic is expected to be larger upon further scaling down of source/drain extension junction depth. However, at this time we cannot build physically complete activation models for uphill arsenic due to the poor understanding with respect to the atomistic structure and formation kinetics of the arsenic uphill diffusion. Knowledge of the underlying mechanism requires DFT or other first principle studies.

### 3.6 CONCLUSION

In this chapter, DFT-based arsenic-interstitial mechanism is implemented into the atomistic kinetic Monte Carlo simulator DADOS. With the physical models and calibrated parameters, our simulation shows excellent agreement with arsenic diffusion profiles in a variety of annealing conditions and point defect environments. Interstitial

mediated arsenic diffusion mechanism is confirmed to be the major reason for arsenic enhanced diffusion in I-rich environment and retarded diffusion in V-rich environments. This can be attributed to the interstitial excess environments during post implant anneal, and the low migration barriers of  $\text{As}_i$  pair compared with  $\text{AsV}$  pair.  $\text{As}_n\text{I}_m$  clusters are observed to appear transiently during the early stages of anneal and then be replaced by the energetically more stable  $\text{As}_n\text{V}_m$  clusters. This transient deactivation by  $\text{As}_n\text{I}_m$  cluster could be important in short time laser anneal or spike anneal. In addition, a surface-trap based kinetic Monte Carlo model is implemented in DADOS to simulate arsenic uphill diffusion in proximity of the  $\text{Si}/\text{SiO}_2$  interface. By using this model, good agreement between simulation and experiments can be obtained in the surface region and the activation contribution from the uphill arsenic has been identified.

## Chapter 4: Arsenic-Defect Complexes at SiO<sub>2</sub>/Si Interfaces

### 4.1 ARSENIC SEGREGATION AT SiO<sub>2</sub>/Si INTERFACE

The behavior of dopant and defect species at semiconductor interfaces has drawn extensive research attention due to their scientific interest and technological importance [Wan01] [Duf03] [Duf05] [Hop04] [Fer06a] [Kas00] [Whe01] [Sai85] [Ste08] [Pei08] [Par08] [Dab00] [Zho05] [Rav05] [Kir05]. A well known example is the dopant uphill diffusion and segregation in SiO<sub>2</sub>/Si interface region [Wan01] [Duf03] [Duf05] [Hop04] [Fer06a]. As the junction depth of CMOS transistors further scales down, this effect may pose more serious technical challenges by increasing dose loss and sheet resistance, leading to device performance degradation [Kas00] [Whe01] [Sai85]. Interface-segregation-induced dose loss may also play a key role in the recent emerging nanowire transistors, where nanowires with much larger interface-body ratio are treated with traditional ion beam doping and thermal anneals [Fer06b] [Col08] [Nah08]. For example, a recent experimental study reports that the fraction of active boron atoms could be as low as 15%~25% in Ge nanowire devices [Nah08]. As an important and practical case, arsenic segregation at SiO<sub>2</sub>/Si interface is of great research interest [Fer06a] [Kas00] [Whe01] [Sai85] [Ste08] [Pei08] [Par08] [Dab00] [Zho05] [Rav05]. However, while recent experimental studies have characterized the arsenic segregation phenomenon very well, there has been less effort in investigating the underlying mechanism [Ste08] [Pei08] [Par08]. There are several theoretical studies addressing the arsenic segregation issue down to the atomistic level [Dab00] [Zho05] [Rav05]. But most of the theoretical studies have focused on the behavior of arsenic in substitutional positions, while disregarding silicon point defects, such as interstitials and vacancies, in SiO<sub>2</sub>/Si interface region. However, the importance of point defect in interface region has been clearly recognized

in recent studies [Kir04] [Kir05]. The interaction between substitutional arsenic and point defects in  $\text{SiO}_2/\text{Si}$  interface region could result in the formation of small arsenic complexes, which may play an important role during the initial stage of arsenic segregation. In addition, due to the unique lattice geometries and strain environment at the  $\text{SiO}_2/\text{Si}$  interface, one would expect significant change in the physics of arsenic complexes close to the interface region. For example, interface arsenic-defect complexes may have different configurations and stabilization properties compared with complexes in bulk Si. Therefore, a complete understanding of segregation mechanism requires the consideration of arsenic-point defect complexes, such as arsenic interstitial pairs ( $\text{As}_i$ ), arsenic vacancy clusters ( $\text{As}_4\text{V}$ ), or even new complex species. In addition, despite existing research about realistic  $\text{SiO}_2/\text{Si}$  interface structures [Bon03] [Har04b], most of the previous arsenic segregation studies [Dab00] [Zho05] [Rav05] still used tridymite-like  $\text{SiO}_2$  in their  $\text{SiO}_2/\text{Si}$  structures. Such artificially-constructed structures typically impose unrealistically large stress on both sides of the interface. Therefore, in order to gain a more accurate understanding, an amorphous  $\text{SiO}_2/\text{Si}$  interface is needed since it is the type of interface that exists most commonly in electronic devices.

In this chapter, we use density functional theory (DFT) [Hoh64] [Koh65] calculation to investigate the mechanism of arsenic pileup and de-activation in  $\text{SiO}_2/\text{Si}$  interface region. First, for the arsenic-defect complexes stabilized in bulk Si, the changes of their behavior induced by the proximity of a- $\text{SiO}_2/\text{Si}$  interface is investigated. Then we identified three energetically favorable arsenic-interstitial complexes which are stabilized only at the  $\text{SiO}_2/\text{Si}$  interface. The configuration, bonding and electronic properties of the interface arsenic-defect complexes are analyzed. Finally, the evolution/diffusion pathways are investigated for the understanding of their formation and migration dynamics. The content of this chapter is submitted to [Kon09].



## 4.2 COMPUTATIONAL DETAILS

We use two types of  $\text{SiO}_2/(110)$  Si interface structures: (1) monolayer crystalline- $\text{SiO}_2/\text{Si}$  system (c- $\text{SiO}_2/\text{Si}$ ) and (2) amorphous  $\text{SiO}_2/\text{Si}$  system (a- $\text{SiO}_2/\text{Si}$ ), as shown in Figure 4.1. The a- $\text{SiO}_2/\text{Si}$  supercell contains 96 Si atoms and 64 O atoms. The c- $\text{SiO}_2/\text{Si}$  interface structure contains 144 Si atoms, 24 O atoms and 48 H atoms. We verified all our major conclusions with larger a- $\text{SiO}_2/\text{Si}$  and c- $\text{SiO}_2/\text{Si}$  supercells to remove the effects induced by using small supercells. If we define z direction to be perpendicular to interface plane and x, y directions are contained in this plane. Periodical boundary conditions are applied in x, y and z directions for both a- $\text{SiO}_2/\text{Si}$  and c- $\text{SiO}_2/\text{Si}$  structures. For a- $\text{SiO}_2/\text{Si}$ , the structure is continuous in all directions and supercell-like. For c- $\text{SiO}_2/\text{Si}$ , the structure is continuous in x and y directions and “slab+vacuum”-like in z direction. The a- $\text{SiO}_2/\text{Si}$  structure is created by a continuous random network (CRN) model [Woo85] [Bur01] [Tu26]. The construction starts from a periodic tridymite  $\text{SiO}_2/\text{Si}$  structure with 9 layers of crystal Si and 4 layers of tridymite  $\text{SiO}_2$ . First, the amorphous  $\text{SiO}_2$  layer is randomized. Then we relax the entire system at 1500K via a large number of bond-switching, which is performed using the METROPOLIS Monte Carlo method with Keating-like potentials [Kea66]. The a- $\text{SiO}_2/\text{Si}$  interface structure is later relaxed by DFT calculation to further minimize the total energy. To verify the generated structure, we also constructed amorphous  $\text{SiO}_2$  with atomic density consistent with typical amorphous  $\text{SiO}_2$  mass density of  $2.2 \text{ g/cm}^3$ . The average Si-O-Si bond angle and bond angle deviation are  $136^\circ$  and  $15^\circ$ , respectively, which is in good agreement with experimental measurements [Bru98]. The monolayer c- $\text{SiO}_2/\text{Si}$  structure simplifies tridymite  $\text{SiO}_2/\text{Si}$  structure by using only one monolayer of  $\text{SiO}_2$  on top of crystal Si and passivating top oxygen and bottom silicon with hydrogen atoms. The monolayer c- $\text{SiO}_2/\text{Si}$  system keeps the  $\text{SiO}_2/\text{Si}$  interface topography while avoiding the unrealistic

strain induced by a rigid tridymite  $\text{SiO}_2/\text{Si}$  structure. We will show that this simplified system is enough for investigating interface arsenic complexes properties and for estimating their relative stability with respect to arsenic complexes in bulk Si.

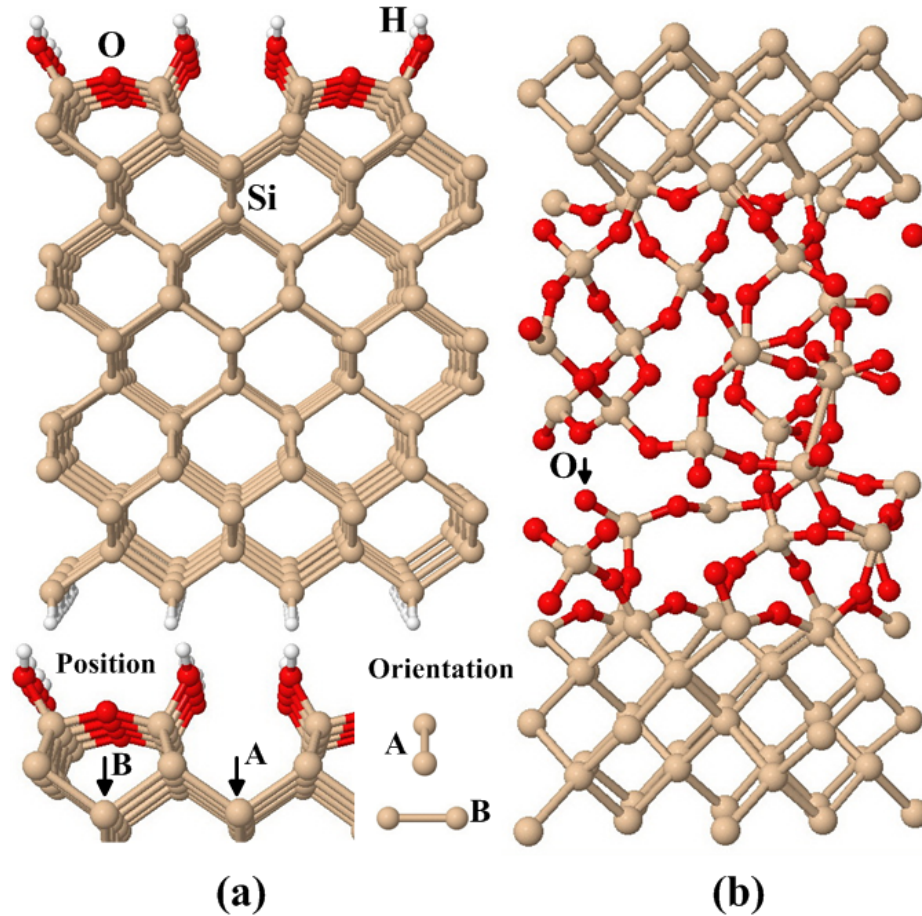


Figure 4.1:  $\text{SiO}_2/\text{Si}$  interface structures used in this work: (a) monolayer crystalline- $\text{SiO}_2/\text{Si}$  interface structure (c- $\text{SiO}_2/\text{Si}$ ) and the definition of position and orientation of arsenic complexes in this system (b) amorphous  $\text{SiO}_2/\text{Si}$  interface structure (a- $\text{SiO}_2/\text{Si}$ ).

For all structure and energetics calculations, we use the plane-wave basis pseudopotential [Rap90] method within the generalized gradient approximation (GGA) to DFT, as implemented in the Vienna ab initio simulation package (VASP) [Kre93] [Kre07]. We use ultrasoft Vanderbilt-type [Van85] pseudopotentials with a plane-wave cutoff energy of 250 eV. All atoms were fully relaxed using the conjugate gradient method with energy convergence threshold of  $1 \times 10^{-3}$  eV. For formation energies,  $\Gamma$  point sampling is used for the k-space summation and the major results are verified with a  $(2 \times 2 \times 1)$  Monkhorst–Pack [Mon76] Brillouin zone sampling. For Fermi level calculations, a  $(4 \times 4 \times 4)$  k-space sampling is used.

Diffusion pathways and barriers are extracted by nudged elastic band method (NEBM) [Hen00]. This method works by linearly interpolating between two fixed initial and final configurations. Each of the images represents a specific geometry between the initial and final states and the images are connected by a spring interaction. The energy minimization of the string of images gives the minimum energy pathway.

The bonding mechanisms are analyzed by electron localization function (ELF) [Sil94] [Bec90]. ELF represents the electron pair localization in terms of the conditional probability of finding an electron in the neighborhood of another electron with the same spin. ELF can take the values ranging from 0 to 1, with ELF=1 corresponding perfect localization and ELF<0.5 suggesting the distribution of delocalized electrons.

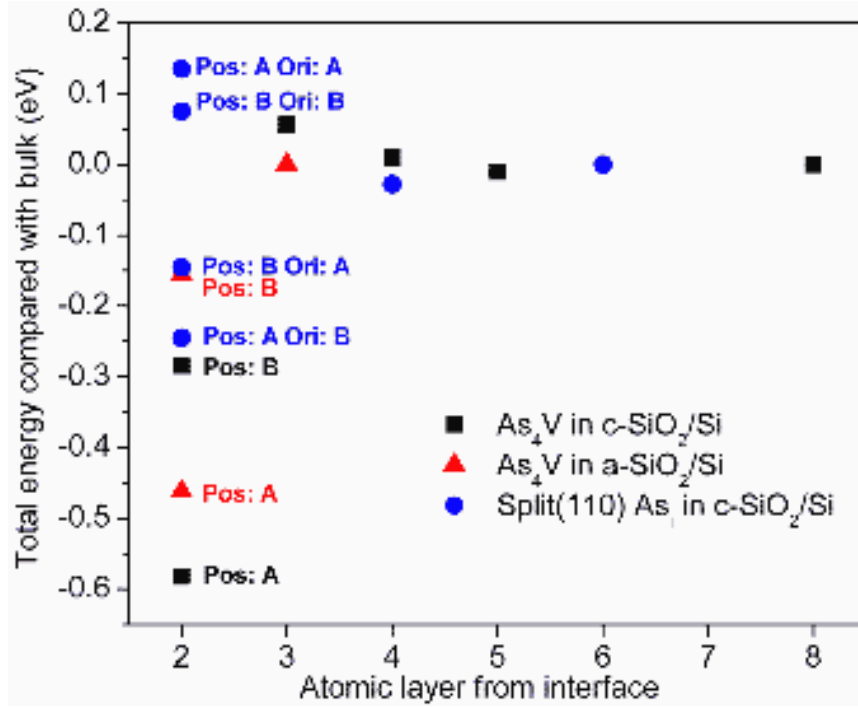


Figure 4.2: Total energy of As<sub>4</sub>V and split(110) As<sub>i</sub> in different layers of SiO<sub>2</sub>/Si interface structure. The total energy of arsenic complex in deep layers (deep layers are considered to have bulk Si-like properties) are set to be 0 eV reference. The position and orientation associated with interface arsenic complexes are marked, corresponding to the definition in Figure 4.1.

### 4.3 BULK-STABILIZED ARSENIC COMPLEXES AT SiO<sub>2</sub>/Si INTERFACE

We first construct the arsenic complexes that are most stable in the bulk Si(bulk-stabilized arsenic complexes), such as substitutional arsenic (As<sub>sub</sub>), As<sub>i</sub> and As<sub>4</sub>V, in our SiO<sub>2</sub>/Si interface system to check how SiO<sub>2</sub>/Si interface would change their stability. After relaxation, we find the proximity to SiO<sub>2</sub>/Si interface does not change the lowest energy configurations of these bulk-stabilized arsenic complexes. In order to estimate the stability difference of bulk-stabilized arsenic complexes in SiO<sub>2</sub>/Si interface region and in bulk Si, we need to first identify a reference depth in our structures, where the influence

of the interface is minimal and arsenic complexes exhibit bulk-like properties. We place  $\text{As}_i$  in split(110) and hexagonal interstitial positions in our interface system and compare the formation energy difference of the two with the difference estimated in bulk Si. We find  $\text{As}_i$  with split(110) configurations are more stable than those with hexagonal configurations. The formation energy difference of these two configurations is 0.46eV in the 4th layer from the  $\text{SiO}_2/\text{Si}$  interface, which is very close to the value of 0.42eV as we calculate in bulk Si. This is in good agreement with a previous study that  $\text{As}_i$  in split(110) configuration is 0.52eV more stable than in hexagonal position in bulk Si [Har05a]. Also in Figure 4.2, the formation energies of  $\text{As}_4\text{V}$  and split(110)  $\text{As}_i$  change very little from 4th layer to deeper layers. Therefore in this work, we treat arsenic complexes in the 4th layer of our structure as in bulk Si, due to the minimal interface effects.

We find that arsenic complexes in the interface layer as well as in  $\text{SiO}_2$  side (both with As-O bonds formed) are energetically less stable than those on the Si side. The As-O bonds can cause up to 2.8eV formation energy penalty. This result is not surprising in that it agrees very well with earlier experimental studies that arsenic atoms reside mainly on the Si side of the interface [Fer06a] [Par08]. Previous theoretical studies also indicated that As-O bonds in  $\text{SiO}_2/\text{Si}$  system are energetically unfavorable [Dab00] [Zho05] [Rav05].

Next we consider the stability of arsenic complexes in the 2<sup>nd</sup> through 6<sup>th</sup> layers from  $\text{SiO}_2/\text{Si}$  interface. We find the bulk-stabilized arsenic complexes have moderate energy gain in these close-to-interface layers than in bulk Si. In our  $\text{SiO}_2/\text{Si}$  system,  $\text{As}_{\text{sub}}$  has less than 0.3eV energy gain in the 2<sup>nd</sup> layer from interface than in bulk Si, and the effect diminishes in deeper layers. As shown in Figure 4.2, the formation energy of split(110)  $\text{As}_i$  in proximity to the  $\text{SiO}_2/\text{Si}$  interface depends highly on the position and orientation of the (110) dumbbell. In certain combinations of position and orientation

(e.g. the (110) dumbbell located in the open channel between two Si-O-Si bridges and oriented perpendicular to the channel direction),  $As_i$  could be moderately stabilized, while in others, the split (110)  $As_i$  at the interface is even less stable than in bulk.  $As_4V$ , the major clustering species in bulk Si [Ram96], is 0.15~0.6eV more stable in the interface layer compared to in bulk Si, and the formation energy also changes with positions. Such a strong position and orientation dependence points to that the stabilization effects can be attributed to geometrical and strain effects rather than to the chemical effects induced by  $SiO_2$ . The interface-induced strain depends on position and orientation of arsenic complexes and decreases fast towards deeper layers, corresponding to the flat profiles of formation energy from 3<sup>rd</sup> to deeper layers in Figure 4.2.

#### 4.4 INTERFACE-STABILIZED ARSENIC COMPLEXES AT $SiO_2/Si$ INTERFACE

Compared with the moderate formation energy gain of bulk-stabilized arsenic complex in  $SiO_2/Si$  interface region, we find that arsenic complexes could be deeply stabilized in several configurations that only exist at  $SiO_2/Si$  interface (interface-stabilized arsenic complexes). Figure 4.3 shows an interface arsenic interstitial configuration ( $As_{it}$ ). The interstitial arsenic forms bonds with three neighboring silicon atoms by breaking the bond between atom 1 and 3. This structure is energetically unfavorable in bulk Si due to the strain it induces into the crystalline Si lattice. At  $SiO_2/Si$  interfaces, however, the  $As_{it}$ -induced lattice distortion seems to be well accommodated by the flexibility of Si-O-Si bond angles. We find this  $As_{it}$  configuration exists at both c- $SiO_2/Si$  and a- $SiO_2/Si$  interfaces, with comparable bond lengths and bond angles.  $As_{it}$  configuration is much more stable than split(110)  $As_i$  configuration in bulk Si, with an energy gain of 1.51eV for c- $SiO_2/Si$  interface and 1.17eV for a- $SiO_2/Si$  interface. The stabilization could be due to the break of strained interface Si-Si bond and the formation

of new bonds in the interface channel space. Due to the randomness of amorphous  $\text{SiO}_2$  structure and a- $\text{SiO}_2/\text{Si}$  interface, this interface stabilization is location-dependent. The energy gain of  $\text{As}_{it}$  depends on local Si-O bonding configurations and may vary in different interface locations. We verified the  $\text{As}_{it}$  complex in four different locations in a large a- $\text{SiO}_2/\text{Si}$  supercell with 512 Si atoms and 256 O atoms. The energy gain ranges from 0.50eV to 1.86eV with an average of 1.09eV, compared with split(110)  $\text{As}_i$  in bulk Si. This high energy advantage could make  $\text{As}_{it}$  a trapping site for out-diffusing  $\text{As}_i$  from bulk Si to  $\text{SiO}_2/\text{Si}$  interface.

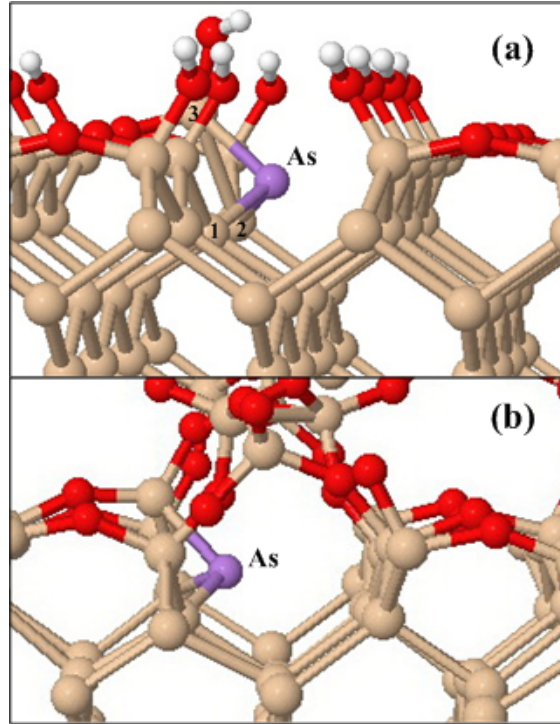


Figure 4.3:  $\text{As}_{it}$  configuration at (a) monolayer c- $\text{SiO}_2/\text{Si}$  interface and (b) a- $\text{SiO}_2/\text{Si}$  interface.

It is worthwhile noting that the  $\text{As}_{it}$  configuration is similar to the split(111) interstitial structure proposed in [Kir05]. The split(111) structure can be viewed as an intermediate trap before silicon interstitial diffuses into  $\text{SiO}_2$ . In contrast,  $\text{As}_{it}$  cannot diffuse into  $\text{SiO}_2$  due to the energetically unfavorable As-O bonds. The formation energy of  $\text{As}_{it}$ , as shown in Figure 4.4(a), is 0.6eV lower than that of split(111) interstitial with a neighboring  $\text{As}_{sub}$ , as shown in Figure 4.4(b). This indicates that aside from structural reasons, chemical effects could also be a factor in the stabilization of  $\text{As}_{it}$ . The less stable split(111) interstitial in a highly arsenic-doped interface may reduce the interstitial out-diffusion into  $\text{SiO}_2$  and potentially change the point-defect-assisted dopant diffusion scenario on the bulk Si side.

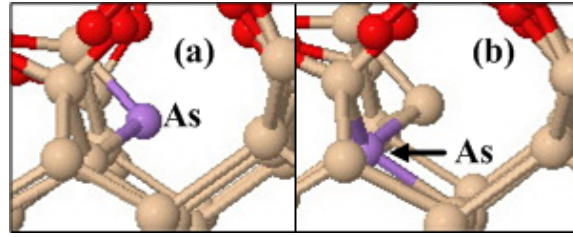


Figure 4.4: (a)  $\text{As}_{it}$  structure (b) Split(111) interstitial structure with a neighboring  $\text{As}_{sub}$ .



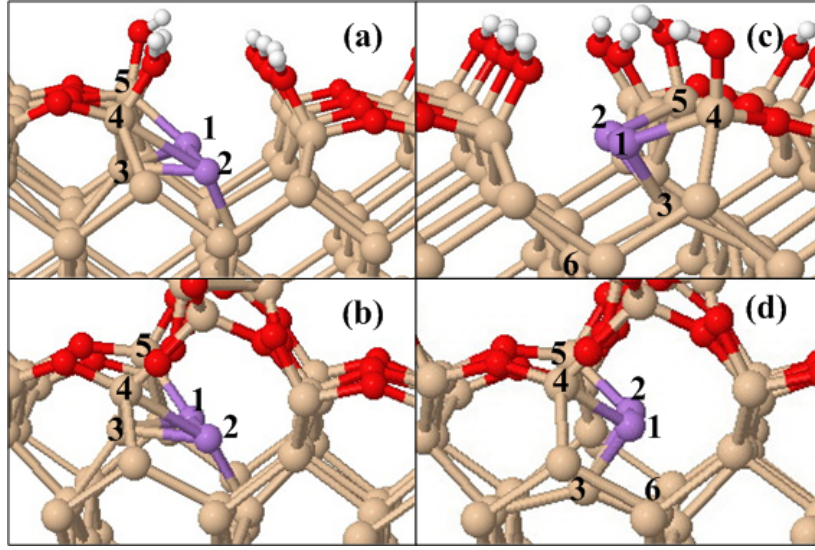


Figure 4.5:  $\text{As}_2\text{I}_{2I}$  configuration at (a) monolayer c- $\text{SiO}_2/\text{Si}$  interface (b) a- $\text{SiO}_2/\text{Si}$  interface;  $\text{As}_2\text{I}_{2II}$  configuration at (c) monolayer c- $\text{SiO}_2/\text{Si}$  interface (d) a- $\text{SiO}_2/\text{Si}$  interface. Atom #1 and #2 are the two arsenic atoms.

Since arsenic segregation usually results in high concentration pileup in  $\text{SiO}_2/\text{Si}$  interface region, the role of clustered arsenic complexes in this region could be important and interesting. Even if a large amount of arsenic pileup may exist in substitutional sites, one may not deny the role of clustered arsenic-defect complexes, at least as segregation precursors since arsenic atoms can only diffuse to the interface via dopant-defect pairing [Ram96] [Ura99] [Kon07] [Kon08]. After checking a variety of clustered arsenic configurations using relatively large c- $\text{SiO}_2/\text{Si}$  structures, we find the most stable ones are those with two As atoms in interstitial positions at the  $\text{SiO}_2/\text{Si}$  interface. Figure 4.5 shows two types of interface stabilized  $\text{As}_2\text{I}_2$  complex structures in our  $\text{SiO}_2/\text{Si}$  system:  $\text{As}_2\text{I}_{2I}$ , as shown in (a), (b), and  $\text{As}_2\text{I}_{2II}$ , as shown in (c), (d). In both structures, two interstitial arsenic atoms are coupled in the interface channel. The difference is in the position and bonding of the underlying silicon atom #3. In  $\text{As}_2\text{I}_{2I}$ , the silicon is in an upper position and forms bond with a first layer silicon atom #4. Both of the two arsenic atoms form

bonds with first layer silicon, except that one bond (As#1 and Si#5) is stronger than the other (As#2 and Si#4). The structure of  $\text{As}_2\text{I}_{2II}$  is more symmetric, with two equally strong As-Si bonds. The underlying Si atom #3 is in a lower position, forming bonds with a third layer Si atom #6. In c-SiO<sub>2</sub>/Si structure, we find the formation energy of  $\text{As}_2\text{I}_I$  is 0.85eV lower than the stable  $\text{As}_2\text{I}_2$  configuration in bulk Si [Kim09], and is 3.01eV lower than two separate bulk-stabilized split(110) As<sub>i</sub>. The symmetric  $\text{As}_2\text{I}_{2II}$  structure is 1.34eV more stable than  $\text{As}_2\text{I}_I$ . In a-SiO<sub>2</sub>/Si structure,  $\text{As}_2\text{I}_I$  is 2.80eV more stable than two separate split(110) As<sub>i</sub> in bulk Si, but  $\text{As}_2\text{I}_{2II}$  is only 0.61eV more stable than  $\text{As}_2\text{I}_I$ . The reduced stability of  $\text{As}_2\text{I}_{2II}$  compared with  $\text{As}_2\text{I}_I$  in a-SiO<sub>2</sub>/Si structure is possibly due to the strain induced from SiO<sub>2</sub>, since the two coupled arsenic atoms push two interface silicon atom #4 and #5 upward into SiO<sub>2</sub> side. In c-SiO<sub>2</sub>/Si structure, such strain is minimal due to the absence of real SiO<sub>2</sub> layers. In bulk Si lattice, such distortion would make these two  $\text{As}_2\text{I}_2$  structures highly unstable. We observe that the stabilization of As<sub>i</sub>,  $\text{As}_2\text{I}_I$  and  $\text{As}_2\text{I}_{2II}$  is largely due to the unique geometrical properties of SiO<sub>2</sub>/Si interface itself, instead of chemical interaction with SiO<sub>2</sub>. Therefore, these arsenic complexes are still important in systems where SiO<sub>2</sub> layers are defective and incomplete, as long as the SiO<sub>2</sub>/Si interface topography is maintained.

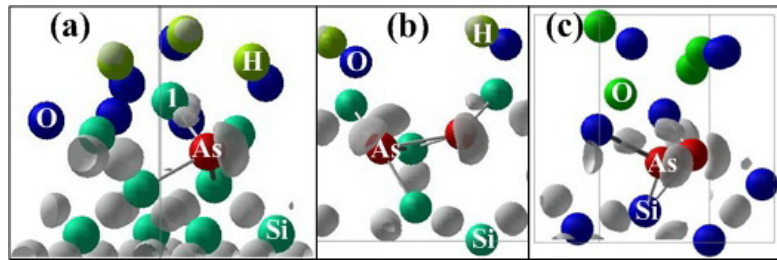


Figure 4.6: ELF iso-surface plot of (a)  $\text{As}_i$  in c-SiO<sub>2</sub>/Si interface, (b)  $\text{As}_2\text{I}_I$  in c-SiO<sub>2</sub>/Si interface and (c)  $\text{As}_2\text{I}_{2II}$  in a-SiO<sub>2</sub>/Si interface, with ELF=0.88. The blue balls represent O and green balls represent Si in (a) and (b). In (c), the blue balls represent Si and green balls are O. Red ball represents As in all (a), (b) and (c).

The charge transfer between interface Si and As in  $As_{it}$ ,  $As_2I_{2I}$  and  $As_2I_{2II}$  can be shown by observing the ELF iso-surface plot in Figure 4.6. Arsenic atoms in all three configurations show electron lone pairs in the interface channel side, which is similar to a previous study [Kir05] for split(111) interstitial at the  $SiO_2/Si$  interface. For  $As_{it}$ , a strong bond exists between arsenic and the interface Si atom #1. For  $As_2I_{2I}$ , this strong bond only exists for one arsenic atom, while the other forms a weaker bond with a third layer Si. In  $As_2I_{2II}$  complex structure, the bonding between arsenic and interface silicon is stronger and exists for both arsenic atoms, which may explain why  $As_2I_{2II}$  is more energetically stable than  $As_2I_{2I}$ .

$E_F-E_V(eV)$	Bulk c-Si(64)	Bulk c-Si (216)	c-SiO <sub>2</sub> /c-Si	a-SiO <sub>2</sub> /c-Si
Defect free	0.33	0.35	0.40	0.42
$As_{sub}$	0.79	0.59	0.87	0.85
Two $As_{sub}$	0.89	0.65		
Three $As_{sub}$		0.68		
$As_2I$	0.53	0.37	0.46	
$As_4V$		0.35	0.40	
$As_{it}$			0.43(0.35)	0.43(0.36)
$As_2I_{2I}$			0.44	0.40
$As_2I_{2II}$			0.39	0.42

Table 4.1: Fermi level of arsenic complexes in bulk Si and  $SiO_2/Si$  interface structures. The 0.35eV and 0.36eV in parentheses indicate deep donor level positions due to  $As_{it}$ .

The electrical activation properties of arsenic pileup at  $SiO_2/Si$  interface are of more interest since it matters for ultra shallow junction device performance and dose loss issues. An arsenic complex is considered electrically “active” if it can contribute electron to conduction band as a donor species. This release of electrons will typically increase the

Fermi level position relative to Si valence band top ( $E_F-E_V$ ). For a given supercell, the  $E_F-E_V$  should be the lowest when donor species are absent (defect-free system) and should increase when electrically active donors are introduced. Here we evaluate the activation properties of arsenic complexes by examining their  $E_F-E_V$ , as shown in Table 4.1. From the bulk Si test cases, we confirmed that active arsenic complexes, such as  $As_{sub}$ , tend to have higher  $E_F-E_V$  than the defect-free structure or structure with electrically inactive complexes, such as  $As_2I$  or  $As_4V$ . If we analysis the Si part of the bandstructure in  $SiO_2/Si$  systems, we find the interface stabilized  $As_{it}$ ,  $As_2I_{2I}$  and  $As_2I_{2II}$  in both c- $SiO_2/Si$  and a- $SiO_2/Si$  systems result in comparable  $E_F-E_V$  in Si bandstructure compared with that of defect-free systems. And the  $E_F-E_V$  of these interface-stabilized arsenic complexes are much smaller than the  $E_F-E_V$  of structures containing  $As_{sub}$ , which is electrically active. This suggests that electrons are localized in these three interface-stabilized arsenic complexes and very few of them can be released for conduction. Therefore, arsenic trapped in interface  $As_{it}$ ,  $As_2I_{2I}$  and  $As_2I_{2II}$  complexes are most likely inactive, which is very consistent with a previous study of Sai-Halasz et al [Sai85]. In a recent experimental paper [Ste08], the authors found that the segregated arsenic exhibits higher electrical activation with increasing arsenic sheet concentration in  $SiO_2/Si$  interface region. This phenomenon was explained by assuming a deep donor state for segregated arsenic. The interaction between donors at high concentration could merge this deep state with the conduction band. The simulation based on this assumption agrees well with their experimental data. In this work, we find  $As_{it}$  indeed induces deep donor level in the Si bandstructure of both a- $SiO_2/Si$  and c- $SiO_2/Si$  systems. The deep donor level is determined at  $E_V+0.35eV$  in a- $SiO_2/Si$  system and  $E_V+0.36eV$  in c- $SiO_2/Si$  system (as the computed Si bandgap is  $0.81eV$  for both systems). This deep donor level may result from electrons that are tightly bonded to  $As_{it}$ . Such electrons can be released to conduction

band upon interactions between neighboring donors. The excellent connection between our theoretical study and experimental results confirms that  $As_{it}$  proposed in this work could be one of the major segregation species. The deep donor state also suggests that  $As_{it}$  could serve as an electron trap and lead to interface current leakage during device operation.

In a previous study by Dabrowski et al. [Dab00], the authors constructed their interface model by using dopant pairing and dangling bond sites trapping mechanism at  $SiO_2/Si$  interface. Simulation with this interface model agrees well with experimental results except that the concentration of interface trapping site required for this agreement is ten times higher than the realistic dangling bond density at  $SiO_2/Si$  interface. The trapping sites based on interface vacancy complexes were proposed to fill the  $10^{13} \text{ cm}^{-2}$  density gap. However, in a later study by Ravichandran et al. [Rav05], the vacancy binding energy at interface was found to be too small to support this trapping mechanism. Instead, the author proposed a hydrogen-based interface trapping mechanism to account for the additional trapping sites. The hydrogen effect, however, was experimentally demonstrated to be at most secondary for the arsenic segregation behavior in a recent study [Ste08]. Now we suggest the  $As_{it}$ ,  $As_2I_{2I}$  and  $As_2I_{2II}$  complexes proposed by this work could be the most likely interface trapping sites to explain the previous inconsistency. As described in this work, the highly stabilized configurations suggest the arsenic-defect complexes could be major candidates for segregation species. The maximum interface density for such complexes is estimated to be at least  $1\sim 2 \times 10^{14} \text{ cm}^{-2}$ , which is enough to hold a large portion of segregation dose. And the trapping in arsenic complexes does not require either dangling bond sites or hydrogen-passivated interface, and is quite different from the dopant pairing mechanism.

#### 4.5 KINETIC ARSENIC COMPLEX MODELS

We also investigated the formation and evolution dynamics of arsenic complexes at the SiO<sub>2</sub>/Si interface. Figure 4.7 shows the diffusion pathways from bulk As<sub>i</sub> configurations to interface As<sub>it</sub> configuration. The forward barriers for this process range between 0.36eV to 0.57eV, depending on the initial bulk As<sub>i</sub> configurations. The reverse barriers from As<sub>it</sub> to bulk As<sub>i</sub> are between 1.45eV to 2.01eV. The forward diffusion barriers are well below the reverse barriers. This fact indicates that As<sub>it</sub> could be created via out-diffusion and interface capture of bulk As<sub>i</sub>. The barrier for arsenic to jump from one interface As<sub>it</sub> position to a neighboring As<sub>it</sub> position is around 0.8eV. This suggests that two As<sub>it</sub> may diffuse in the interface layer and couple with each other to form a more stable As<sub>2</sub>I<sub>2</sub> complex, which could be in either the As<sub>2</sub>I<sub>2I</sub> form or As<sub>2</sub>I<sub>2II</sub> form. While As<sub>2</sub>I<sub>2II</sub> is at least 0.6eV more stable than As<sub>2</sub>I<sub>2I</sub>, our NEBM calculation shows that it still takes ~0.80eV barrier for the evolution from As<sub>2</sub>I<sub>2I</sub> to As<sub>2</sub>I<sub>2II</sub> to occur, as shown in Figure 4.7(d).

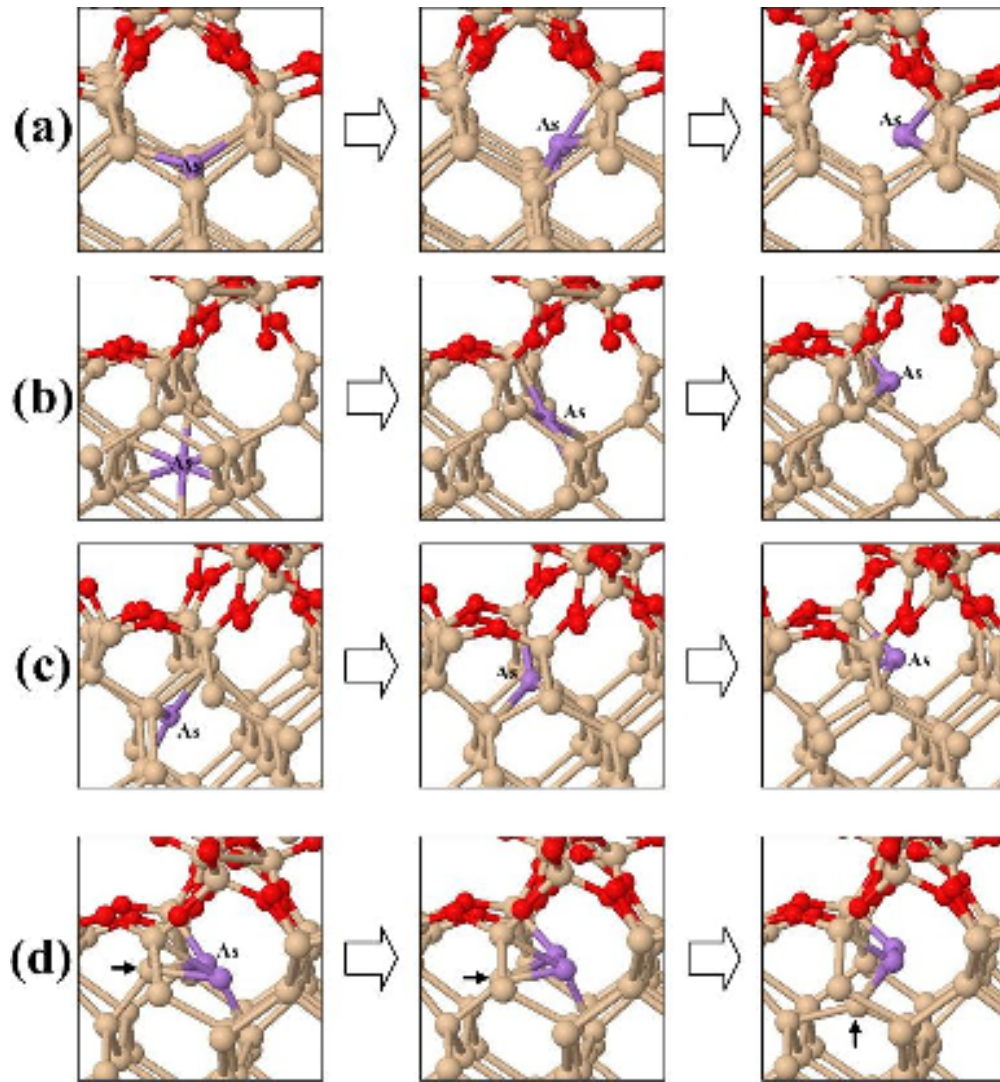


Figure 4.7: Evolution from  $As_i$  in bulk Si to interface  $As_{it}$ : (a) from split(110)  $As_i$  to  $As_{it}$ . (b), (c) from hexagonal  $As_i$  to  $As_{it}$ . (d) Transition from  $As_2I_{2I}$  to  $As_2I_{2II}$ .

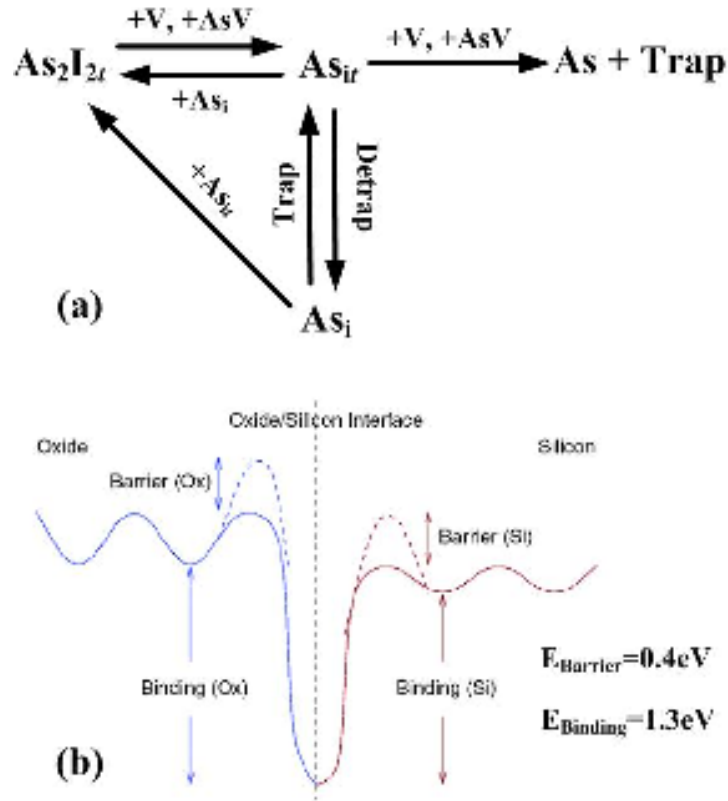


Figure 4.8: Kinetic models for arsenic segregation based on DFT studies: (a) DADOS models (b) Sentaurus Process models [Sen09].

Kinetic Monte Carlo simulation is performed based on the results of the DFT work. Two interface models are used, as shown in Figure 4.8. In the first one as shown in Figure 4.8(a), we introduce arsenic complexes and interface traps into DADOS and then define reactions between them. For example, As-interstitial pair can be trapped into  $As_{ir}$ , which can turn back to substitutional As by I-V recombination.

Since  $As_{ir}$  could play a central role, so the segregation process could be simplified by a trap and detrap model. The second interface model is provided by the Synopsys Sentaurus Process[Sen09], as shown in Figure 4.8(b). Dopant species can be captured in



this interface trap, and it takes a binding energy and barrier energy to escape. The energy parameters we used are extracted from the migration calculation.

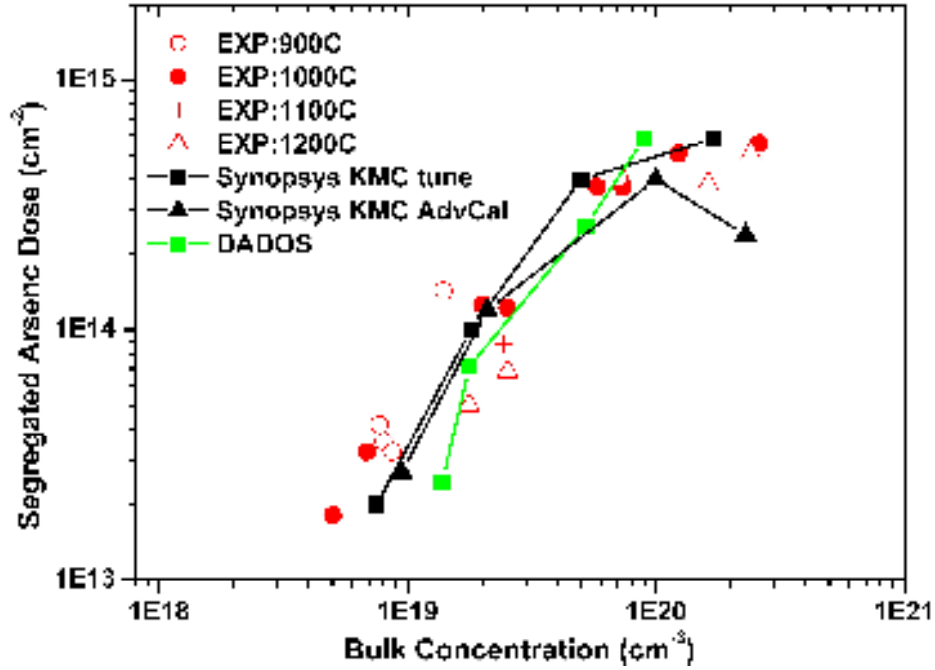


Figure 4.9: Comparison of kinetic Monte Carlo simulation and experimental data from [Ste08].

The simulation from both models is compared with experimental data. The experimental data is segregated arsenic dose versus the arsenic concentration under the interface, with different dose implant and long-time anneal [Ste08]. By comparing simulation and experiments, we find both DADOS and Synopsys models agree very well with the experimental results, as shown in Figure 4.9. The fitting could be even better if some more calibration is used. So with the models and parameters from this work, we can predict arsenic segregation effects accurately even using a simple interface model like this.

## 4.6 CONCLUSION

The configuration, bonding, electrical activation and dynamics of arsenic complexes in SiO<sub>2</sub>/Si interface region were investigated using plane wave-based DFT calculation. We found that bulk-stabilized arsenic complexes (such as As<sub>sub</sub>, split(110) As<sub>i</sub> and As<sub>4</sub>V which are stable arsenic complexes in bulk Si) have interface strain-induced energy gain in SiO<sub>2</sub>/Si interface region. On the other hand, we discovered three interface-stabilized arsenic complexes, As<sub>it</sub>, As<sub>2</sub>I<sub>2I</sub>, As<sub>2</sub>I<sub>2II</sub>, that exist only at SiO<sub>2</sub>/Si interface layer. The three interface-stabilized complexes are energetically far more favorable than arsenic complexes in bulk Si because they form strong bonds with interface Si and the resulting structural distortion induces minimal strain in the lattice due to the flexible Si-O-Si bond angles at SiO<sub>2</sub>/Si interface. The activation properties of the interface stabilized arsenic complexes are estimated and all of the three complexes are confirmed to be inactive. The experimentally reported increasing electrical activation when segregation dose becomes higher can be attributed to the deep donor level of As<sub>it</sub>. By analyzing the diffusion/evolution pathways of the arsenic complexes, we suggest interface complexes could be formed by trapping out-diffusing As<sub>i</sub> from bulk Si to SiO<sub>2</sub>/Si interface, and As<sub>2</sub>I<sub>2I</sub>/As<sub>2</sub>I<sub>2II</sub>, may also be created by diffusion and clustering of two neighboring As<sub>it</sub> defects.

From process integration point of view, in order to reduce segregation-induced dose loss, interface structure modification could be a viable method. In arsenic segregation cases, we can pre-occupy the channel positions where As<sub>it</sub> is energy favorable. Alternatively, we can modify the flexible interfacial Si-O-Si bonding structure to make it more rigid. A rigid interface structure will increase the formation energy of arsenic complexes due to the poor tolerance of induced lattice strain. Other than surface

modification, since arsenic complexes are mostly in interstitial sites, they can potentially be annihilated by vacancies introduced by point defect engineering.

## Chapter 5: Boron Diffusion Dynamics in Amorphous Silicon

### 5.1 INTRODUCTION

Pre-amorphisation and solid phase epitaxial regrowth (SPER) techniques are widely used for silicon (Si) transistor fabrication. This approach can produce ultra shallow and steep junction profiles as well as high dopant activation level. However recently, Jacques et al. [Jac03] reported five orders of magnitude boron diffusivity enhancement in amorphous-Si (a-Si) compared with that in crystalline-Si (c-Si) during SPER at 550°C. Venezia and Duffy et al. [Ven05] [Duf04] confirmed this high diffusivity and estimated the activation energy to be  $\sim 2.1$  eV in a-Si, which is well below the value of  $\sim 3.65$  eV in c-Si [Pic04]. The fast boron diffusion profile at low temperature is illustrated in Figure 5.1. This abnormally fast diffusion in a-Si could cause significant boron redistribution during SPER and thus pose a great challenge to ultra-shallow junction formation. Despite the technological importance of this phenomenon, it is poorly understood. A recent experimental study [Mir08] found this fast boron diffusion to be transient and proposed a dangling-bond(DB)-mediated diffusion mechanism to explain it. The transient behavior of the boron fast diffusion is shown in Figure 5.2. Other theoretical studies [Url08] [Har04b] indicated that point defects, such as interstitials and vacancies which act as the major diffusion drivers in c-Si, also exist in a-Si. Urli et al. [Url08] also pointed out that the annihilation of point defects proceeds at the same pace as the DB reduction, which is consistent with the transient feature of this fast boron diffusion. Therefore, in addition to the DB-mediated mechanism, point defects may also play a key role in the fast boron diffusion in a-Si, especially when the implantation-induced point defects have a time-dependant high concentration before the structural

relaxation in a-Si is completed. However, at this time, there is little atomistic level understanding of dopant-point defect dynamics in a-Si.

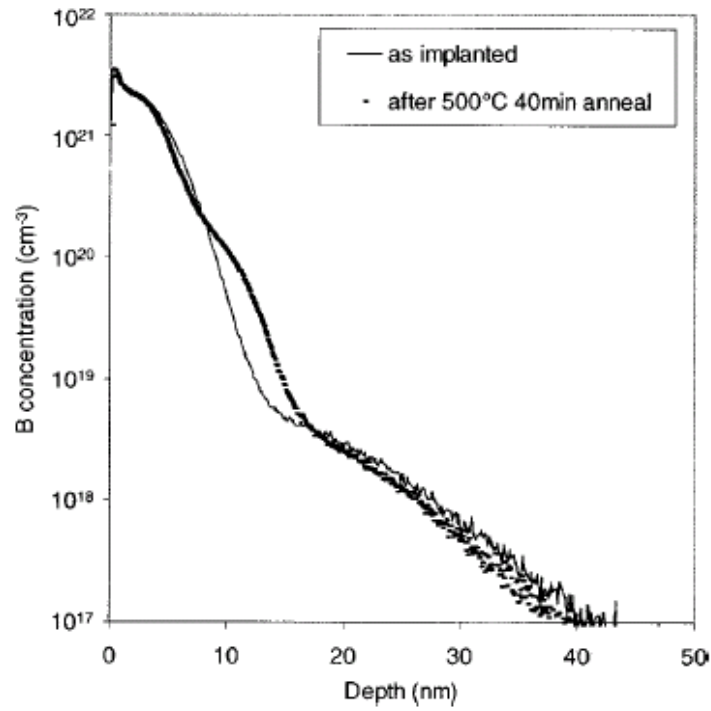


Figure 5.1: Boron fast diffusion at low annealing temperature. This figure is from [Duf04].

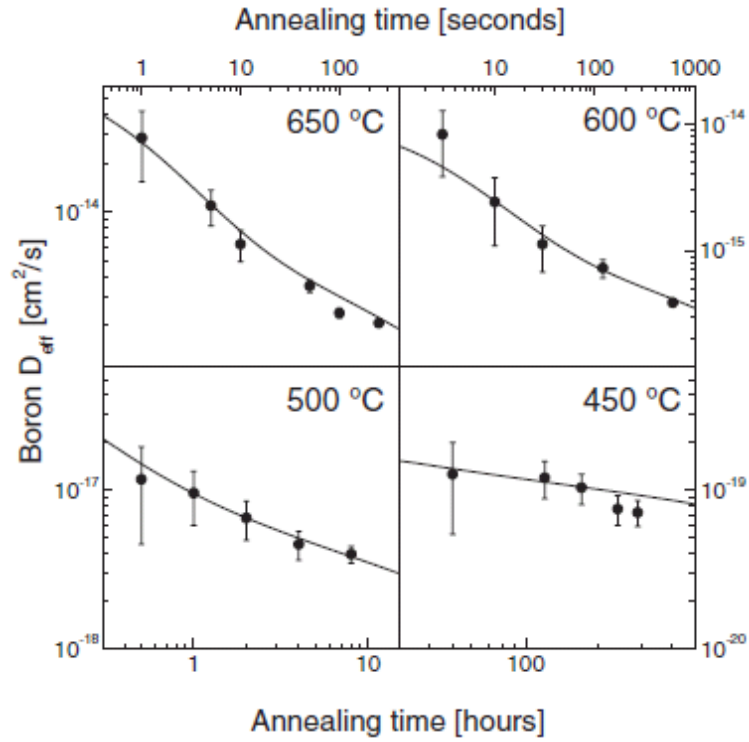


Figure 5.2: Transient feature of boron fast diffusion: diffusivity decreases with time. This figure is from [Mir08].

In this chapter, we examine boron diffusion dynamics in a-Si using density-functional theory (DFT) and ab initio molecular dynamics (MD) simulations. Based on MD, we suggest an interstitial-based boron diffusion mechanism in a-Si. The stability and migration barrier of the neutral and charged diffusion species are estimated. We propose an explanation for the high boron diffusivity in a-Si, and compare our calculations with experiments.

## 5.2 COMPUTATIONAL DETAILS

A continuous random network model is used to generate a 64 atoms a-Si structure, as shown in Figure 5.3(a). We also verified our major conclusions using a larger supercell as shown in Figure 5.3(b). The detailed procedure of a-Si construction can be found in [Har04b]. In most of our simulations, the a-Si lattice undergoes no major structural change during the time scale in which boron diffuses and interacts with point defects. Therefore this original a-Si structure is used as a reference lattice to show the boron behavior. However, during this time scale, our MD simulation shows that if a Si atom is displaced from its original site, it will be mobile enough to diffuse around the relatively stable a-Si lattice and interact with boron. We refer to this Si as “interstitial in a-Si” due to its similarity with interstitial in c-Si during the time scale in which boron-point defect interaction occurs in this work. On a larger time scale, this “interstitial” may not be distinguishable due to the entire a-Si structural relaxation and incorporation of this extra atom into the a-Si network.

For all calculations, we use the plane-wave basis pseudopotential method within the generalized gradient approximation (GGA) to DFT, as implemented in the Vienna Ab-initio Simulation Package (VASP) [Kre93]. We use ultrasoft Vanderbilt-type pseudopotentials [Van90] and a plane-wave cutoff energy of 150eV for MD and 250eV for static calculation. All atoms were fully relaxed using the conjugate gradient method with force convergence threshold of  $1 \times 10^{-2}$  eV/Å. A (4x4x4) Monkhorst-Pack Brillouin zone sampling is used in the interstitial formation energy calculation while for other cases  $\Gamma$  point sampling is used. The temperature of MD simulation is controlled by the Nosé algorithm. A velocity Verlet algorithm was used for integrating the equations of motion with a 1fs time step. Migration barriers are extracted using the nudged elastic band method (NEBM) [Hen00]. For the charged defect calculation, the overall charge

neutrality in the periodic supercell is maintained by introducing a homogeneous background charge. The formation energy of positively charged defects relative to the neutral state is expressed as:  $E_f^+ - E_f^0 = (E_D^+ - E_D^0) + (E_V + E_F)$  [Jeo01], where  $E_D$  is the total energy and  $E_F$  is the Fermi level relative to the valence band top,  $E_V$ .

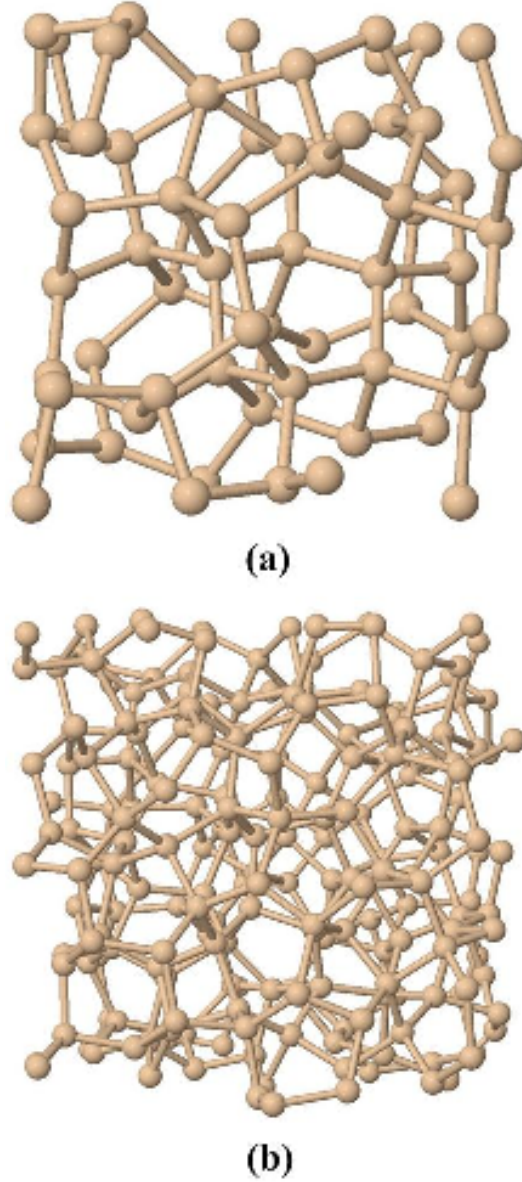


Figure 5.3: Amorphous silicon supercells: (a) 64-atom (b) 211-atom.



Due to the lack of global symmetries in a-Si structure, the formation and migration energies of point defects and dopant species are heavily influenced by local environment, such as neighboring atomic and bond configuration, leading to relatively large variations. Therefore, we focus our study on extracting physical diffusion mechanism rather than finding exact energy values. Nevertheless, we try to minimize this variation by performing calculations at several locations in the a-Si lattice. Our calculations indicate that boron-vacancy pair is much less stable than boron-interstitial pair in a-Si. Therefore, we consider only the behavior of  $B_i$ , where boron is in an interstitial position among the original a-Si lattice sites, and  $B_{sub}+I$ , where boron is in one of the original a-Si lattice sites with a neighboring Si displaced from this lattice site.

### 5.3 RESULTS AND DISCUSSION

First, we observe the  $B_i$  dynamics in a-Si by performing MD simulation of a 900°C, 2ps anneal. We construct 19 initial a-Si+ $B_i$  structures, including 12 with  $HB_i$ , in which boron is located in the center of a hexagonal ring, as shown in Figure 5.4 (a) and (c), 4 with split  $B_i$ , in which boron shares a lattice position with a Si atom, as shown in Figure 5.6 (a), and 3 with  $PB_i$ , in which boron is in the center of a pentagonal ring, as shown in Figure 5.5 (b). After anneal, we find that in 14 out of 19 samples, the  $B_i$  kicks out a lattice Si and become  $B_{sub}+I$ . As shown in Figure 5.4 (a) (b) and (c) (d),  $B_i$  kicks out Si #1 and takes the lattice position. By analyzing bond configuration changes and energy gains, we can clearly differentiate between  $B_{sub}$  and  $B_i$  in a-Si. The average energy gain from the initial state  $B_i$  to the final state  $B_{sub}+I$  is calculated to be 0.56+0.26eV. The time evolution shows that  $B_i$  tends to occupy a lattice position in an early stage of the annealing and stays trapped until the end of the simulation. This trend indicates that

boron prefers to stay in the original a-Si lattice sites as  $B_{\text{sub}}$ , which may be due to charge transfer and local stress compensation effects [Zhu96].

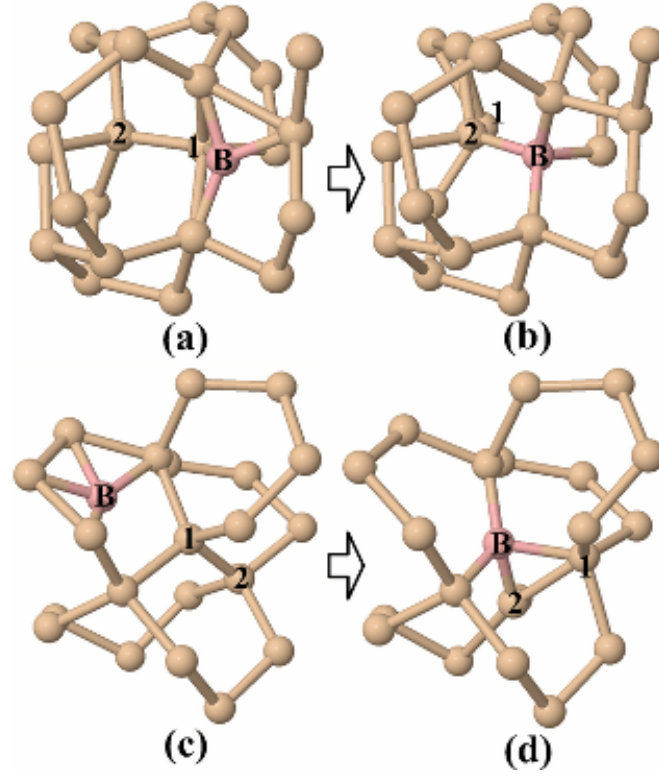


Figure 5.4: MD simulation shows  $B_i$  will kick out lattice Si and become  $B_{\text{sub}}+I$ .

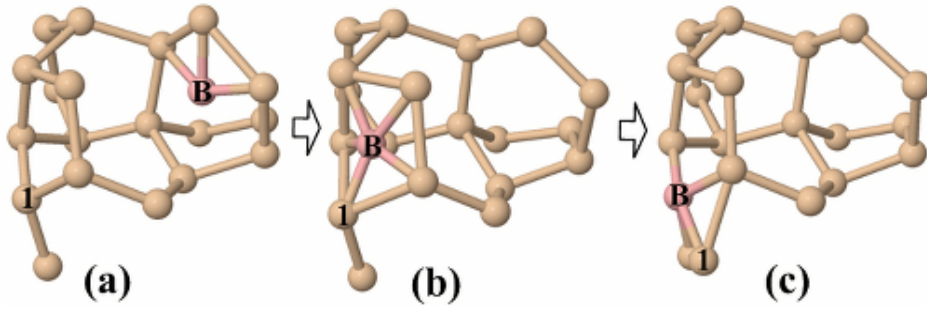


Figure 5.5: The diffusion of  $B_i$  through a-Si lattice.

Due to the limited time period of MD simulation and the trapping efficiency of the  $B_{\text{sub}}$  state, it is difficult to capture long distance  $B_i$  jumps through a-Si lattice. However, we do observe this jumping in two of our samples, where a locally less-dense area is available between two interstitial sites so that  $B_i$  can migrate over with low barriers. This locally less-dense area possibly results from the inhomogeneous nature of a-Si, or the formation of vacancies [Url08]. As shown in Figure 5.5(a) (b), boron atom starts from an  $HB_i$  position and diffuses to a  $PB_i$  position, with a barrier of only 0.12eV. The boron finally kicks out a lattice Si and forms  $B_{\text{sub}}+I$ , as shown in Figure 5.5(c). Combined with the previous knowledge that  $B_{\text{sub}}$  is well stabilized, we suggest  $B_i$  could be the major diffusion species in a-Si.

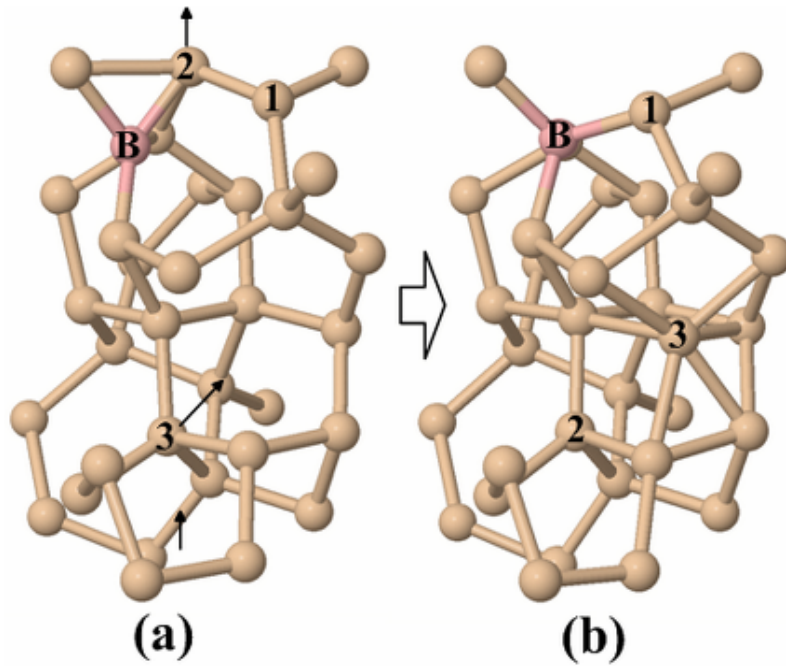


Figure 5.6: The mobility of kicked-out interstitials.  $B_i$  kicks out Si #2 and Si #2 kicks out Si #3. Due to periodic boundary conditions, Si #2 moves upward and injects from down side of Si #3.

The  $B_i$ -based diffusion requires mobile Si interstitials to kick  $B_{sub}$  out to become  $B_i$ . Most of our MD simulations show that when  $B_i$  kicks in to be  $B_{sub}+I$ , the kicked-out I will move around and in many cases kick out another lattice Si. As shown in Figure 5.6, boron kicks out Si #2, which diffuses for a relatively long distance and kicks out lattice Si #3. Given the 2ps short simulation time, this scenario suggests the contribution to boron diffusion from mobile interstitials over a longer time period. In a practical process, ion implantation will induce a large number of excess interstitials, which are unlikely for the a-Si network to accommodate and immobilize instantaneously. Since the relaxation of interstitials proceeds at the same pace as the reduction of DB [Url08], while the latter is proved to be consistent with the transient feature of boron fast diffusion in a-Si [Mir08], one cannot deny the possibility that the transient high interstitial concentration in a-Si will assist the boron fast diffusion as well.

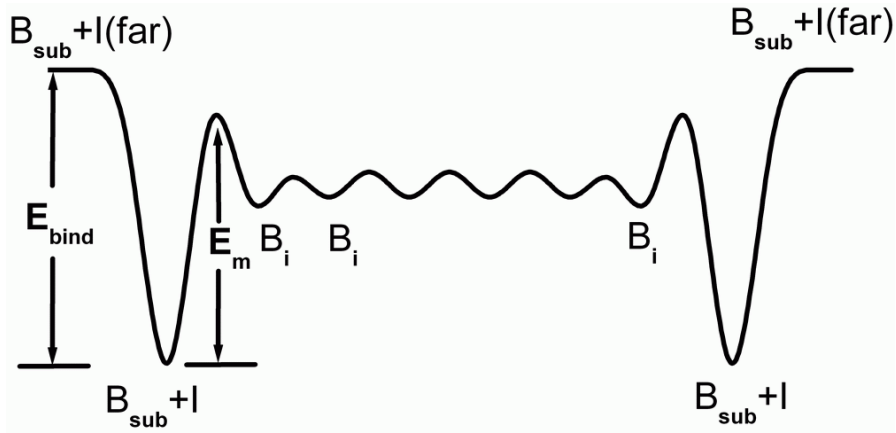


Figure 5.7: Interstitial-based B diffusion mechanism in a-Si.

The stable  $B_{sub}$ , diffusing  $B_i$  and mobile interstitial in a-Si suggest an interstitial-based boron diffusion mechanism, similar to the kick-out mechanism proposed earlier for

boron diffusion in c-Si [Zhu96]. As shown in Figure 5.7, boron tends to stay in the low energy  $B_{\text{sub}}$  position until an incoming interstitial knocks it out as  $B_i$ , which will jump between neighboring interstitial sites before falling back to  $B_{\text{sub}}$ . The activation energy for this mechanism can be estimated from the migration barrier  $E_m$  between two  $B_{\text{sub}}+I$  states, the interstitial formation energy,  $E_{\text{fl}}$ , and the binding energy,  $E_{\text{bind}}$ , of  $B_{\text{sub}}+I$  pair. The  $E_{\text{act}}$  can be expressed as  $E_{\text{act}}=E_{\text{fl}} - E_{\text{bind}}(B_{\text{sub}}+I)+E_m(B_{\text{sub}})$ . The interstitial formation energy is calculated by  $E_{\text{fl}}=E_{\text{total}}(\text{a-Si})\times 65/64-E_{\text{total}}(\text{a-Si}+I)$ , with an average over 35 samples including hexagonal, split and randomly placed interstitials. For neutral interstitial in a-Si,  $E_{\text{fl}}^0$  is calculated to be  $2.63\pm 0.51\text{eV}$ . In the c-Si case, as a comparison,  $E_{\text{fl}}^0$  of hexagonal and split(110) interstitial is calculated to be  $3.87\text{eV}$  and  $3.90\text{eV}$ , respectively. The  $E_{\text{fl}}^0$  in a-Si is over  $1.2\text{eV}$  lower than that in c-Si, which is consistent with a previous study [Har04b]. This lowering could be due to the bond rearrangement associated with interstitial integration in the a-Si lattice [Har04b]. The formation energy of positively charged  $I^+$  is calculated to be  $E_{\text{fl}}^+=2.16+E_F\text{ eV}$ .

The  $E_{\text{bind}}$  of  $B_{\text{sub}}+I$  is assessed from the total energy difference between the configuration that  $B_{\text{sub}}$  and  $I$  are paired together, and the configuration that  $I$  is moved far apart from  $B_{\text{sub}}$  where the binding effect is minimized. The  $E_{\text{bind}}$  is calculated as  $0.60\pm 0.35\text{eV}$  for neutral pairs  $(B_{\text{sub}}+I)^0$ , and  $0.52\pm 0.27\text{eV}$  for charged pairs  $(B_{\text{sub}}+I)^+$ , each averaged over 22 samples.

To calculate the  $B_{\text{sub}}$ -to- $B_i$  barrier  $E_m$ , we construct NEBM pathways from  $B_{\text{sub}}+I$  to  $B_i$ , based on MD trajectories and local energy minimum sites. For neutral  $(B_{\text{sub}}+I)^0$ ,  $E_m$  is estimated to be  $0.70\pm 0.35\text{eV}$ , while for  $(B_{\text{sub}}+I)^+$  it is  $0.87\pm 0.35\text{eV}$ , each averaged over 19 samples. Although there is no guarantee that the lowest barrier pathway can be found by this method, the accuracy of our results is enough for a semi-quantitative estimation.

According to the above calculation,  $E_{\text{act}}=2.73\text{eV}$  and  $(2.49+E_F)\text{eV}$  for neutral and positively charged defect-based diffusion, respectively. Our calculated  $E_{\text{act}}$  agrees well with the experimentally reported activation energy range from 3.0eV [Mir08] to 2.1eV [Ven05]. It can also be seen that the charged pair has a considerable diffusion contribution, especially in heavily p-doped cases, which is consistent with the experimentally reported concentration-dependent diffusion [Jac03] [Ven05] [Duf04] [Mir08]. More importantly, the calculation shows that most of the contribution to the  $E_{\text{act}}$  lowering is from the 1.2eV lowering of  $E_{\text{fi}}$  compared to its value in c-Si. This suggests that the fast diffusion is mainly because interstitials have a larger concentration in a-Si than in c-Si, which should boost the interstitial-mediated boron diffusion.

#### 5.4 CONCLUSION

In summary, we proposed an interstitial-based boron diffusion mechanism in a-Si. In the a-Si lattice, boron will preferentially stay in substitutional position as  $B_{\text{sub}}$ , while interstitial site  $B_i$  is the major diffusing species. The boron fast diffusion can be explained by the energetically more favorable interstitial formation in a-Si than in c-Si. The interstitial-based mechanism is consistent with experiments for both activation energy and the transient and concentration-dependent features observed for boron diffusion in a-Si.

## Chapter 6: Conclusions and Recommendation for Future Work

### 6.1 CONCLUSIONS

In chapter 2, arsenic enhanced or retarded diffusion is observed by overlapping the dopant region with, respectively, interstitial-rich and vacancy-rich regions produced by Si implants. Enhanced diffusion can be attributed to interstitial-mediated diffusion during post-implant annealing. Two possible mechanisms for diffusion retardation, interstitial-vacancy recombination and dopant clustering, are analyzed in additional experiments and the former one is proved to be dominant. This point defect engineering approach demonstrated in this chapter could be applied to fabrication of n-type ultra shallow junctions.

In chapter 3, a kinetic arsenic-interstitial interaction model has been developed to study and predict arsenic TED and deactivation. This model is based on DFT studies and has been verified by previous experiments in which the significant role of interstitial mechanism in arsenic TED was revealed. The mechanism of enhanced and retarded arsenic diffusion in different point defect environments is investigated by utilizing this model in kinetic Monte Carlo simulation. The arsenic-interstitial pair, with low binding energy and low migration energy, is shown to be the major contributor to arsenic TED in silicon interstitial rich situations. In addition, by using this model, we demonstrated the transient existence of arsenic interstitial clusters ( $As_nI_m$ ) during post-implant annealing and propose their possible role in deactivation for short time anneals such as laser anneal and spike anneal. Moreover, we developed a novel surface-trap based kinetic Monte Carlo model to simulate arsenic uphill diffusion in proximity to the  $SiO_2/Si$  interface. The simulation results show that the activation behavior of the uphill portion of arsenic has considerable impact on the junction sheet resistance. The activation behavior of this

arsenic is expected to become more important when junction depth is scaled down further.

In chapter 4, the behavior of arsenic-defect complexes at amorphous SiO<sub>2</sub>/Si(110) interfaces has been studied using DFT calculation. We find that arsenic-defect complexes that are stable in bulk Si show moderate energy gain in SiO<sub>2</sub>/Si interface region due to the interface-induced strain effect. We have identified three arsenic-defect complex configurations, As<sub>ii</sub>, As<sub>2</sub>I<sub>2I</sub> and As<sub>2</sub>I<sub>2II</sub>, which exist only at the SiO<sub>2</sub>/Si interface. These interface arsenic-defect complexes are highly stabilized due to their unique bonding configurations at SiO<sub>2</sub>/Si interface. Therefore, they could contribute to arsenic segregation as both initial stage precursor and dopant trapping sites. Our calculation indicates that arsenic atoms trapped in such interface complexes are electrically inactive. Finally, the formation and evolution dynamics of interface arsenic-defect complexes are discussed. Kinetic Monte Carlo simulation based on the DFT models shows very good agreement with experimental results.

In chapter 5, we identified a fast boron diffusion mechanism in amorphous silicon using DFT calculations. We found that interstitial-like point defects, omnipresent in as-implanted silicon, to be very stable in an amorphous network and can form highly mobile pair with boron atoms. The transient existence of such point defects in amorphous silicon is suggested to play an important role in boron diffusion. We found the activation energy for this pathway to be 2.73eV, in good agreement with experimental results. In addition, this mechanism is consistent with the experimentally reported transient and concentration-dependent features of boron diffusion in amorphous silicon.



## 6.2 RECOMMENDATION FOR FUTURE WORK

Since the diffusion and deactivation of arsenic in point defect engineered silicon has been studied in this work, it is very natural to attempt to apply this technique to real process flow. As far as I know, this technique has not been widely used in real process flow yet mainly because there is a good alternative: pre-amorphisation and solid phase epitaxial regrowth (SPER). However, SPER will typically induce end-of-range (EOR) defects resulting from the implant damage and excess interstitials introduced. During annealing, these EOR defects will release interstitials, which will lead to dopant TED. Also EOR defects may increase junction leakage if they lie in the junction depletion region. The sub-amorphous point defect engineering implant may largely reduce such undesirable effects by reducing the damage level. It is especially suitable for SOI devices since interstitial-rich region can be designed to be within the buried oxide region. Still, before this technique can be applied, there remain many process integration challenges which can be considered as future extension of this study.

In Chapter 4, we proposed several possible solutions to suppress arsenic segregation at  $\text{SiO}_2/\text{Si}$  interface such as pre-occupying the interface channel positions or modifying interface structures to make it rigid. These solutions can be demonstrated and verified using DFT calculations. For example, by examining whether nitrogen atoms can stably occupy interface channel positions, we can conclude whether a nitrogen ambient interface treatment will suppress arsenic segregation. Another solution we proposed is to introduce external vacancies to annihilate interstitial-based arsenic complexes. This can also be verified by DFT calculation combined with kinetic Monte Carlo simulation and experiments. The possible future work as mentioned above could be of great practical importance to semiconductor industry.

Besides boron, arsenic and phosphorus diffusion mechanism in amorphous silicon could also be interesting. The methodology could be similar to the one proposed in this work. However, the experimental results for arsenic and phosphorus diffusion in amorphous silicon are fewer than those for boron. In addition, if amorphous silicon supercell that contains dangling bonds can be constructed by CRN method, we can analyze how boron fast diffusion can be assisted by dangling bonds. The dangling bond-assisted boron diffusion has been reported experimentally [Mir08]. But using molecular dynamics method, a more detailed atomistic level understanding can be obtained.

## References

- [AMC07] Atomistic kMC, Sentaurus Process 2007.03 release by Synopsys Inc.
- [Bec90] A. D. Becke, and K. E. Edgecombe, "A simple measure of electron localization in atomic and molecular systems" *Journal of Chemical Physics*, **92**, 5397, 1990.
- [Ber98] M. A. Berding, A. Sher, and M. van Schilfgaarde, "Deactivation in heavily arsenic-doped silicon" *Applied Physics Letters*, **72**, 1492, 1998.
- [Bon98] A. Bongiorno, L. Colombo, and T. Diaz De la Rubia, "Structural and binding properties of vacancy clusters in silicon" *Europhysics Letters*, **43** (6), pp. 695-700, 1998.
- [Bon03] A. Bongiorno, A. Pasquarello, M. S. Hybertsen, and L. C. Feldman, "Transition Structure at the Si(100)-SiO<sub>2</sub> Interface" *Physical Review Letters*, **90**, 186101, 2003.
- [Bra95] H. Bracht, N. A. Stolwijk, and H. Mehrer, "Properties of intrinsic point defects in silicon determined by zinc diffusion experiments under nonequilibrium conditions" *Physical Review B*, **52**(16), 16542, 1995.
- [Brin99] R. Brindos, P. Keys, K. S. Jones, and M. E. Law, "Effect of arsenic doping on {311} defect dissolution in silicon" *Applied Physics Letters*, **75**, 229, 1999.
- [Bru98] A. Brunet-Bruneau, D. Souche, S. Fisson, V. N. Van, G. Vuye, F. Abeles, and J. Rivory, "Microstructural characterization of ion assisted SiO<sub>2</sub> thin films by visible and infrared ellipsometry" *Journal of Vacuum Science and Technology A*, **16**, 2281, 1998.
- [Bur01] V. M. Burlakov, G. A. D. Briggs, A. P. Sutton, and Y. Tsukahara, "Monte Carlo simulation of growth of porous SiO<sub>x</sub> by vapor deposition" *Physical Review Letters*, **86**, 3052, 2001.
- [Cer86] G. F. Cerofolini, P. Manini, L. Meda, M. L. Polignano, G. Queirolo, F. Nava, G. Ottaviani, and M. Gallorini, "Thermodynamic and kinetic-properties of arsenic-implanted silicon" *Thin Solid Films*, **135**(1):59–72, 1986.

- [Col08] A. Colli, A. Fasoli, C. Ronning, S. Pisana, S. Piscanec, and A. C. Ferrari, “Ion beam doping of silicon nanowires” *Nano Letters*, **8**, 2188, 2008.
- [Cow91] N. E. B. Cowern, G. F. A. van de Valle, D. J. Gravesteijn, and C. J. Vriezema, “Experiments on atomic-scale mechanisms of diffusion” *Physical Review Letters*, **67**(2), 212, 1991.
- [Cow99a] N. E. B. Cowern, G. Mannino, P. A. Stolk, F. Roozeboom, H. Huizing, J. van Berkum, F. Cristiano, A. Claverie, and M. Jaraiz, “Cluster ripening and transient enhanced diffusion in silicon” *Materials Science in Semiconductor Processing*, **2**, 369–376, 1999.
- [Cow99b] N. E. B. Cowern, G. Mannino, P. A. Stolk, F. Roozeboom, H. G. A. Huizing, J. G. M. van Berkum, F. Cristiano, A. Claverie, and M. Jaraiz, “Energetics of self-interstitial clusters in Si” *Physical Review Letters*, **82**(22), 4460, 1999.
- [Cow05] N. E. B. Cowern, A. J. Smith, B. Colombeau, R. Gwilliam, B. J. Sealy, and E. J. H. Collar, “Understanding, modeling and optimizing vacancy engineering for stable highly boron-doped ultrashallow junctions” *IEEE International Electron Devices Meeting*, 2005.
- [Dab00] J. Dabrowski, R. A. Casali, H.-J. Müssig, R. Baierle, M. J. Caldas, and V. Zavodinsky, “Mechanism of dopant segregation to SiO<sub>2</sub>/Si(001) interfaces” *Journal of Vacuum Science and Technology B*, **18**, 2160, 2000.
- [DAD] DADOS, distributed by Professor Martin Jaraiz from University of Valladolid.
- [Duf03] R. Duffy, V. C. Venezia, A. Heringa, T. W. T. Husken, M. J. P. Hopstaken, N. E. B. Cowern, P. B. Griffin, and C. C. Wang, “Boron uphill diffusion during ultrashallow junction formation” *Applied Physics Letters*, **82**, 3647, 2003.
- [Duf04] R. Duffy, V. C. Venezia, A. Heringa, B. J. Pawlak, M. J. P. Hopstaken, G. C. J. Mass, Y. Tamminga, T. Dao, F. Roozeboom, and L. Pelaz, “Boron diffusion in amorphous silicon and the role of fluorine” *Applied Physics Letters*, **84**, 4283, 2004.
- [Duf05] R. Duffy, V. C. Venezia, J. Loo, M. J. P. Hopstaken, M. A. Verheijen, J. G. M. van Berkum, G. C. J. Maas, and C. Demeurisse, “Low-temperature diffusion of high-concentration phosphorus in silicon, a preferential movement toward the surface” *Applied Physics Letters*, **86**, 081917, 2005.
- [Fah89] P. M. Fahey, P. B. Griffin, and J. D. Plummer, “Point defects and dopant diffusion in silicon” *Reviews of Modern Physics*, **61**, 289, 1989.

- [Fai81] R. B. Fair, “Impurity Doping Processes in Silicon” pp.315, North-Holland, 1981.
- [Fer06a] M. Ferri, S. Solmi, A. Parisini, M. Bersani, D. Giubertoni, and M. Barozzi, “Arsenic uphill diffusion during shallow junction formation” *Journal of Applied Physics*, **99**, 113508, 2006.
- [Fer06b] M. V. Fernández-Serra, Ch. Adessi, and X. Blase, “Surface segregation and backscattering in doped silicon nanowires” *Physical Review Letters*, **96**, 166805, 2006.
- [Fet71] A. L. Fetter, and J. D. Walecka, “Quantum Theory of Many-Particle Systems” McGraw-Hill, New York, p.29, 1971.
- [Gie00] A. Giese, H. Bracht, N. A. Stolwijk, and D. Baither, “Microscopic defects in silicon induced by zinc out-diffusion” *Materials Science and Engineering B*, **71**, 160, 2000.
- [Har04a] S. A. Harrison, T. F. Edgar, and G. S. Hwang, “Interaction between interstitials and arsenic-vacancy complexes in crystalline silicon” *Applied Physics Letters*, **85**, 4935, 2004.
- [Har04b] S. A. Harrison, D. Yu, T. F. Edgar, G. S. Hwang, T. A. Kirichenko, and S. K. Banerjee, “Origin of vacancy and interstitial stabilization at the amorphous-crystalline Si interface” *Journal of Applied Physics*, **96**, 3334, 2004.
- [Har05a] S. A. Harrison, T. F. Edgar, and G. S. Hwang, “Structure, stability, and diffusion of arsenic-silicon interstitial pairs” *Applied Physics Letters*, **87**, 231905, 2005.
- [Har05b] S. A. Harrison, T. F. Edgar, and G. S. Hwang, “Structure and dynamics of the diarsenic complex in crystalline silicon” *Physical Review B*, **72**, 195414, 2005.
- [Har06] S. A. Harrison, T. F. Edgar, and G. S. Hwang, “Interstitial-mediated arsenic clustering in ultrashallow junction formation” *Electrochemical and Solid-State Letters*, **9** (12) G354-G357, 2006.
- [Hen00] G. Henkelman, B. P. Uberuaga, and H. Jonsson, “A climbing image nudged elastic band method for finding saddle points and minimum energy paths” *Journal of Chemical Physics*, **113**, 9901, 2000.
- [Hoh64] P. Hohenberg, and W. Kohn, “Inhomogeneous Electron Gas” *Physical Review*, **136**, B864, 1964.

- [Hop04] M. J. P. Hopstaken, Y. Tamminga, M. A. Verheijen, R. Duffy, V. C. Venezia, and A. Heringa, "Effects of crystalline regrowth on dopant profiles in preamorphized silicon" *Applied Surface Science*, **231**, 688-692, 2004.
- [Ish82] Y. Ishikawa, Y. Sakina, H. Tanaka, S. Matsumoto, and T. J. Niimi, "The enhanced diffusion of arsenic and phosphorus in silicon by thermal-oxidation" *Journal of the Electrochemical Society*, **129**(3):644-648, 1982.
- [Jac03] J. M. Jacques, L. S. Robertson, K. S. Jones, M. E. Law, M. Rendon, and J. Bennett, "Fluorine-enhanced boron diffusion in amorphous silicon" *Applied Physics Letters*, **82**, 3469, 2003.
- [Jar96] M. Jaraiz, G. H. Gilmer, J. M. Poate, and T. D. de la Rubia, "Atomistic calculations of ion implantation in Si: Point defect and transient enhanced diffusion phenomena" *Applied Physics Letters*, **68**, 409, 1996.
- [Jeo01] J. W. Jeong, and A. Oshiyama, "Atomic and electronic structures of a boron impurity and its diffusion pathways in crystalline Si" *Physical Review B*, **64**, 235204, 2001.
- [Kal01] R. Kalyanaraman, T. E. Haynes, O. W. Holland, H.-J. L. Gossmann, C. S. Rafferty, and G. H. Gilmer, "Binding energy of vacancies to clusters formed in Si by high-energy ion implantation" *Applied Physics Letters*, **79**, 1983, 2001.
- [Kas00] R. Kasnavi, Y. Sun, R. Mo, P. Panetta, P. B. Griffin, and J. D. Plummer, "Characterization of arsenic dose loss at the Si/SiO<sub>2</sub> interface" *Journal of Applied Physics*, **87**, 2255, 2000.
- [Kea66] P. Keating, "Effect of invariance requirements on the elastic strain energy of crystals with application to the diamond structure" *Physical Review*, **145**, 637, 1966.
- [Kim02] R. Kim, T. Hirose, T. Shano, H. Tsuji, and K. Taniguchi, "Influences of Point and Extended Defects on As Diffusion in Si" *Japanese Journal of Applied Physics*, Part 1, **41**, 227, 2002.
- [Kim09] Y. Kim, T. A. Kirichenko, N. Kong, G. Henkelman, and S. K. Banerjee, "First-principles studies of small arsenic interstitial complexes in crystalline silicon" *Physical Review B*, **79**, 075201, 2009.
- [Kir04] T. A. Kirichenko, S. K. Banerjee, and G. S. Hwang, "Interaction of neutral vacancies and interstitials with the Si(001) surface" *Physical Review B*, **70**, 045321, 2004.

- [Kir05] T. A. Kirichenko, D. Yu, S. K. Banerjee, and G. S. Hwang, "Silicon interstitials at Si/SiO<sub>2</sub> interfaces: Density functional calculations" *Physical Review B*, **72**, 035345, 2005.
- [Koh65] W. Kohn, and L. J. Sham, "Self-consistent equations including exchange and correlation effects" *Physical Review*, **140**, 1133A, 1965.
- [Kon07] N. Kong, T. A. Kirichenko, S. G. H. Anderson, M. C. Foisy, and S. K. Banerjee, "Enhanced and retarded diffusion of arsenic in silicon by point defect engineering" *Applied Physics Letters*, **90**, 062107, 2007.
- [Kon08] N. Kong, T. A. Kirichenko, Y. Kim, M. C. Foisy, and S. K. Banerjee, "Physically based kinetic Monte Carlo modeling of arsenic-interstitial interaction and arsenic uphill diffusion during ultrashallow junction formation" *Journal of Applied Physics*, **104**, 013514, 2008.
- [Kon09] N. Kong, T. A. Kirichenko, G. S. Hwang, and S. K. Banerjee, "Arsenic-defect complexes at SiO<sub>2</sub>/Si interfaces" *Physical Review B*, (submitted April, 2009)
- [Kre93] G. Kresse, and J. Hafner, "Ab initio molecular dynamics for liquid metals" *Physical Review B*, **47**, 558, 1993.
- [Kre96a] G. Kresse, and J. Furthmuller, "Efficiency of ab-initio total energy calculations for metals and semiconductors using a plane-wave basis set" *Computational Materials Science*, **6**, 15-50, 1996.
- [Kre96b] G. Kresse, and J. Furthmuller, "Efficient iterative schemes for ab initio total-energy calculations using a plane-wave basis set" *Physical Review B*, **54**, 11169, 1996.
- [Kre07] G. Kresse, and J. Furthmuller, "VASP the Guide" Vienna University of Technology, Vienna, 2007.
- [Lau89] F. Lau, L. Mader, C. Mazure, Ch. Werner, and M. Orlowski, "A model for phosphorus segregation at the silicon-silicon dioxide interface" *Applied Physics A-Materials Science & Processing*, **49**, 671, 1989.
- [Law95] D.W. Lawther, U. Myler, and P.J. Simpson, "Vacancy generation resulting from electrical deactivation of arsenic" *Applied Physics Letters*, **67**, 3575, 1995.
- [Mar04] I. Martin-Bragado, M. Jaraiz, P. Castrillo, R. Pinacho, J. E. Rubio, and J. Barbolla, "Ion implant simulations: Kinetic Monte Carlo annealing assessment of the dominant features" *Applied Physics Letters*, **84**, 4962, 2004.

- [MarD] Ignacio Martin-Bragado, PhD Dissertation, University of Valladolid, 2004.
- [Mat83] D. Mathiot, and J. C. Pifster, “Diffusion of arsenic in silicon: Validity of the percolation model” *Applied Physics Letters*, **42**, 1043, 1983.
- [Mic87] A. E. Michel, W. Rausch, P. A. Ronsheim, and R. H. Kastl, “Rapid annealing and the anomalous diffusion of ion implanted boron into silicon” *Applied Physics Letters*, **50**, 416, 1987.
- [Mir08] S. Mirabella, D. D. Salvador, E. Bruno, E. Napolitani, E. F. Pecora, S. Boninelli, and F. Priolo, “Mechanism of boron diffusion in amorphous silicon” *Physical Review Letters*, **100**, 155901, 2008.
- [Mon76] H. Monkhorst, and J. Pack, “Special points for Brillouin-zone integrations” *Physical Review B*, **13**, 5188, 1976.
- [Moo65] G. E. Moore, “Cramming more components onto integrated circuits” *Electronics*, **38**(8), April 9, 1965.
- [Nah08] J. Nah, K. Varahramyan, E. S. Liu, S. K. Banerjee, and E. Tutuc, “Doping of Ge–Si<sub>x</sub>Ge<sub>1–x</sub> core-shell nanowires using low energy ion implantation” *Applied Physics Letters*, **93**, 203108, 2008.
- [Pan88] K. C. Pandey, A. Erbil, G. S. Cargill, and R. F. Boehme, “Annealing of heavily arsenic-doped silicon: electrical deactivation and a new defect complex” *Physical Review Letters*, **61**, 1282, 1988.
- [Par08] A. Parisini, V. Morandi, S. Solmi, P. G. Merli, D. Giubertoni, M. Bersani, and J. A. van den Berg, “Quantitative determination of the dopant distribution in Si ultrashallow junctions by tilted sample annular dark field scanning transmission electron microscopy” *Applied Physics Letters*, **92**, 261907, 2008.
- [Pay92] M. C. Payne, M. P. Teter, D. C. Allan, T. A. Arias, and J. D. Joannopoulos, “Iterative minimization techniques for ab initio total-energy calculations: molecular dynamics and conjugate gradients” *Reviews of Modern Physics*, **64**, 4, 1992.
- [Pei08] L. Pei, G. Duscher, C. Steen, P. Pichler, H. Ryssel, E. Napolitani, D. De Salvador, A. M. Piro, A. Terrasi, F. Severac, F. Cristiano, K. Ravichandran, N. Gupta, and W. Windl, “Detailed arsenic concentration profiles at Si/SiO<sub>2</sub> interfaces” *Journal of Applied Physics*, **104**, 043507, 2008.
- [Pel97] L. Pelaz, M. Jaraiz, G. H. Gilmer, H.-J. Gossmann, C. S. Rafferty, D. Eaglesham, and J. M. Poate, “B diffusion and clustering in ion implanted



- Si: The role of B cluster precursors” *Applied Physics Letters*, **70**(17), 2285, 1997.
- [Pel99] L. Pelaz, G. H. Gilmer, V. C. Venezia, H.-J. Gossmann, M. Jaraiz, and J. Barbolla, “Modeling of the effects of dose, dose rate, and implant temperature on transient enhanced diffusion” *Applied Physics Letters*, **74**, 2017, 1999.
- [Pel03] L. Pelaz, L. A. Marques, M. Aboy, J. Barbolla, and G. H. Gilmer, “Atomistic modeling of amorphization and recrystallization in silicon” *Applied Physics Letters*, **82**, 2038, 2003.
- [Per96] J. P. Perdew, K. Burke, and M. Ernzerhof, “Generalized Gradient Approximation made simple” *Physical Review Letters*, **77**, 3865, 1996.
- [Pic04] P. Pichler, “Intrinsic Point Defects, Impurities, and Their Diffusion in Silicon” Springer, 2004.
- [Pin05] R. Pinacho, M. Jaraiz, P. Castrillo, I. Martin-Bragado, J. E. Rubio, and J. Barbolla, “Modeling arsenic deactivation through arsenic-vacancy clusters using an atomistic kinetic Monte Carlo approach” *Applied Physics Letters*, **86**, 252103, 2005.
- [Plu00] J. D. Plummer, M. D. Deal, and P. B. Graffin, “Silicon VLSI technology: Fundamentals, Practice and Modeling” page 388, Prentice Hall, 2000.
- [Ram96] M. Ramamoorthy, and S. T. Pantelides, “Complex dynamical phenomena in heavily arsenic doped silicon” *Physical Review Letters*, **76**, 4753, 1996.
- [Rap90] A. M. Rappe, K. M. Rabe, E. Kaxiras, and J. D. Joannopoulos, “Optimized pseudopotentials” *Physical Review B*, **41**, 1227, 1990.
- [Rav05] K. Ravichandran, and W. Windl, “Ab initio study of the effect of hydrogen and point defects on arsenic segregation at Si(100)/SiO<sub>2</sub> interfaces” *Applied Physics Letters*, **86**, 152106, 2005.
- [Sai85] G. A. Sai-Halasz, K. T. Short, and J. S. Williams, “Antimony and arsenic segregation at Si-SiO<sub>2</sub> interfaces” *IEEE Electron Device Letters*, **6**, 285, 1985.
- [Sen07] Sentaurus Process 2007.03 release by Synopsys Inc.
- [Sen09] Sentaurus Process 2009.06 release by Synopsys Inc.

- [Sil94] B. Silvi, and A. Savin, "Classification of chemical bonds based on topological analysis of electron localization functions" *Nature* **371**, 683, 1994.
- [Sol03] S. Solmi, M. Ferri, M. Bersani, D. Guibertoni, and V. Soncini, "Transient enhanced diffusion of arsenic in silicon" *Journal of Applied Physics*, **94**, 4950, 2003.
- [Ste08] C. Steen, A. Martinez-Limia, P. Pichler, H. Ryssel, S. Paul, W. Lerch, L. Pei, G. Duscher, F. Severac, F. Cristiano, and W. Windl, "Distribution and segregation of arsenic at the SiO<sub>2</sub>/Si interface" *Journal of Applied Physics*, **104**, 023518, 2008.
- [Sto97] P. A. Stolk, H. J. Gossmann, D. J. Eaglesham, D. C. Jacobson, C. S. Rafferty, G. H. Gilmer, M. Jaraiz, J. M. Poate, H. S. Luftman, and T. E. Haynes, "Physical mechanism of transient enhanced dopant diffusion in ion-implanted silicon" *Journal of Applied Physics*, **81**, 6031, 1997.
- [Sul98] A. Sultan, S. K. Banerjee, S. List, and V. McNeil, "An approach using a subamorphizing threshold dose silicon implant of optimal energy to achieve shallower junctions" *Journal of Applied Physics*, **83**, 8046, 1998.
- [Syn09] Synopsys Sentaurus article, "TCAD Application Advanced Examples (2D)", 2009.
- [Tu98] Y. Tu, J. Tersoff, G. Grinstein, and D. Vanderbilt, "Properties of a Continuous-Random-Network model for amorphous systems" *Physical Review Letters*, **81**, 4899, 1998.
- [Ura99] A. Ural, P. B. Griffin, and J. D. Plummer, "Fractional contributions of microscopic diffusion mechanisms for common dopants and self-diffusion in silicon" *Journal of Applied Physics*, **85**, 6440, 1999.
- [Url08] X. Urli, C. L. Dias, L. J. Lewis, and S. Roorda, "Point defects in pure amorphous silicon and their role in structural relaxation: A tight-binding molecular-dynamics study" *Physical Review B*, **77**, 155204, 2008.
- [UTM] Simulation by UT-MARLOWE code, distributed by the University of Texas at Austin.
- [Van85] D. Vanderbilt, "Optimally smooth norm-conserving pseudopotentials" *Physical Review B*, **32**, 8412, 1985.
- [Van90] D. Vanderbilt, "Soft self-consistent pseudopotentials in a generalized eigenvalue formalism" *Physical Review B*, **41**, 7892, 1990.

- [Van02] J. A. Van den Berg, D. G. Armour, S. Zhang, S. Whelan, H. Ohno, T. S. Wang, A. G. Cullis, E. H. J. Collart, R. D. Goldberg, P. Bailey, and T. C. Q. Noakes, "Characterization by medium energy ion scattering of damage and dopant profiles produced by ultrashallow B and As implants into Si at different temperatures" *Journal of Vacuum Science and Technology B*, **20**(3), 974, 2002.
- [Ven00] V. C. Venezia, T. E. Haynes, A. Agarwal, L. Pelaz, H.-J. Gossmann, D. C. Jacobson, and D. J. Eaglesham, "Mechanism for the reduction of interstitial supersaturations in MeV-implanted silicon" *Applied Physics Letters*, **74**, 1299, 2000.
- [Ven05] V. C. Venezia, R. Duffy, L. Pelaz, M. J. P. Hopstaken, G. C. J. Mass, T. Dao, Y. Tammimga, and P. Graat, "Boron diffusion in amorphous silicon" *Materials Science and Engineering B*, **124**, 245, 2005.
- [Wan01] H. C. Wang, C. C. Wang, C. S. Chang, T. Wang, P. B. Griffin, and C. H. Diaz, "Interface induced uphill diffusion of boron: an effective approach for ultrashallow junction" *IEEE Electron Device Letters*, **22**, 65, 2001.
- [Whe01] S. Whelan, V. Privitera, G. Mannino, M. Italia, C. Bongiorno, A. La Magna, and E. Napolitani, "Electrical activation of ultralow energy As implants in Si" *Journal of Applied Physics*, **90**, 3873, 2001.
- [Woo85] F. Wooten, K. Winer, and D. Weaire, "Computer generation of structural models of amorphous Si and Ge" *Physical Review Letters*, **54**, 1392, 1985.
- [Xie99] J. J. Xie, and S. P. Chen, "Diffusion and clustering in heavily arsenic-doped silicon: Discrepancies and Explanation" *Physical Review Letters*, **83**, 1795, 1999.
- [Zho05] Z. Zhou, M. L. Steigerwald, R. A. Friesner, L. Brus, and M. S. Hybertsen, "Dopant local bonding and electrical activity near Si(001)-oxide interfaces" *Journal of Applied Physics*, **98**, 076105, 2005.
- [Zhu96] J. Zhu, T. D. de la Rubia, L. H. Yang, C. Maillhot, and G. H. Gilmer, "Ab initio pseudopotential calculations of B diffusion and pairing in Si" *Physical Review B*, **54**, 4741, 1996.

## **Vita**

Ning Kong was born in Feidong County, Hefei, Anhui Province, China in June, 1982. After graduating from Feidong No.1 Middle School in 1999, he entered University of Science and Technology of China in Hefei. In July of 2004, he graduated from University of Science and Technology of China with a Bachelor of Science in Applied Physics. In August of 2004, he entered the Graduate School at the University of Texas at Austin. After spending one semester in the Department of Physics, he joined the Department of Electrical and Computer Engineering in January 2005. In May 2005, he began his research under the guidance of Professor Sanjay K. Banerjee and Dr. Taras A. Kirichenko. He received the degree of Master of Science in Engineering in May 2007. He was admitted to Ph.D. candidacy in July 2008.

Permanent address: 7401 N. Lamar Blvd. Apt. 204, Austin, TX 78752

This dissertation was typed by the author.